ANTIBACTERIAL, UV PROTECTION AND HYDROPHOBIC PROPERTIES OF COTTON FABRIC COATED WITH TiO_2/GO/ZnO COMPOSITES

SUCHANAN SUKSRI

Graduate School Srinakharinwirot University

2024

สมบัติการยับยั้งแบคทีเรีย การป้องกันยูวี และความไม่ชอบน้ำของผ้าฝ้าย ที่เคลือบด้วยวัสดุผสม TiO_2/GO/ZnO

สุชานันท์ สุขศรี

ปริญญานิพนธ์นี้เป็นส่วนหนึ่งของการศึกษาตามหลักสูตร
วิทยาศาสตรมหาบัณฑิต สาขาวิชาวัสดุศาสตร์
คณะวิทยาศาสตร์ มหาวิทยาลัยศรีนครินทรวิโรฒ
ปีการศึกษา 2567
ลิขสิทธิ์ของมหาวิทยาลัยศรีนครินทรวิโรฒ

ANTIBACTERIAL, UV PROTECTION AND HYDROPHOBIC PROPERTIES OF COTTON FABRIC COATED WITH TiO_2/GO/ZnO COMPOSITES

SUCHANAN SUKSRI

A Thesis Submitted in Partial Fulfillment of the Requirements

for the Degree of MASTER OF SCIENCE

(Materials Science)

Faculty of Science, Srinakharinwirot University

2024

Copyright of Srinakharinwirot University

THE THESIS TITLED

ANTIBACTERIAL, UV PROTECTION AND HYDROPHOBIC PROPERTIES OF COTTON FABRIC COATED WITH TIO_2/GO/ZNO COMPOSITES

BY

SUCHANAN SUKSRI

HAS BEEN APPROVED BY THE GRADUATE SCHOOL IN PARTIAL FULFILLMENT OF THE REQUIREMENTS FOR THE MASTER OF SCIENCE IN MATERIALS SCIENCE AT SRINAKHARINWIROT UNIVERSITY

(Assoc. Prof. Dr. Chatchai Ekpanyaskul, MD.)
Dean of Graduate School

ORAL DEFENSE COMMITTEE

..... Major-advisor
(Asst. Prof.Areeya Aeimbhu)

..... Chair
(Asst. Prof. Dr.Wandee Onreabroy)

..... Committee
(Asst. Prof.Panitarn Wanakamol)

Title	ANTIBACTERIAL, UV PROTECTION AND HYDROPHOBIC PROPERTIES OF COTTON FABRIC COATED WITH TiO_2/GO/ZnO COMPOSITES
Author	SUCHANAN SUKSRI
Degree	MASTER OF SCIENCE
Academic Year	2024
Thesis Advisor	Assistant Professor Areeya Aeimbhu

This research aims to improve the functionality of cotton fabrics by coating them with TiO_2-GO-ZnO (TNPsGZ) composite to enhance its hydrophobicity, UV protection and antibacterial properties. The TNPsGZ composite was synthesized, characterized and applied to cotton fabric using a dip-dry-cured technique. Titanium dioxide nanoparticles and graphene oxide flakes (TG) were mixed in a weight ratio of 1.94:0.06. The TNPsGZ was synthesized using an ultrasonic-assisted method, combining the TG and zinc oxide particles with four different weights of TG: ZnO (1:1, 1:3, 1:5 and 1:7). The composite was characterized using Fourier transform infrared spectroscopy (FTIR), Raman spectroscopy, X-ray diffraction (XRD), field emission scanning electron microscopy (FE-SEM) and Energy dispersive spectrometer (EDS). The TNPsGZ, combined with a binder, was coated onto cotton fabrics, which were subsequently assessed for their hydrophobicity, UV protection and antibacterial activity. The results indicated that the 1:1 ratio significantly improved hydrophobicity, achieving a water contact angle of 129° and strong UV protection with a UPF rating of 30, blocking over 96% of UV-A and 97% of UV-B radiation. However, the composite exhibited limited antibacterial activity against *Staphylococcus aureus* and *Escherichia coli*.

Keyword : Cotton, Titanium Dioxide, Graphene Oxide, Zinc Oxide, Nanocomposites, Hydrophobic, UV-Protecting, Antibacterial

ACKNOWLEDGEMENTS

This research would not have been successfully completed without the invaluable support and guidance of Assistant Professor Dr. Areeya Aiembhu, my research advisor. I am deeply grateful for her insightful advice, constructive feedback, and assistance in refining this work. Her commitment to this project played a vital role in its completion. I would also like to extend my heartfelt thanks to my parents, friends, and the Department of Materials Science, Srinakharinwirot University, for their constant encouragement and support throughout my research journey.

SUCHANAN SUKSRI

TABLE OF CONTENTS

Page

LIST OF TABLES

Page

LIST OF FIGURES

Page

CHAPTER 1
INTRODUCTION

1.1 Background and significance of the research

Clothing is essential for people of all genders and ages. Clothes made from cotton provide comfort and excellent ventilation, making them well-suited for tropical climates like Thailand and Southeast Asia, where the hot and humid weather can cause sweating stains and dirt that may be challenging to remove, affecting the wearer's appearance. (1) Cotton, composed of almost pure cellulose (making up 88-96% of the fiber), offers a range of excellent properties, including hygroscopicity (moisture absorption), air permeability, biodegradability, and the absence of static electricity. These characteristics make cotton a preferred choice for clothing and textile products, with a global market share of 48% worldwide fiber consumption. (2) However, cotton fabric does have some limitations, such as its lack of antimicrobial activity, relatively low strength, despite its good liquid absorbency, and poor sensitivity to UV light.(3) Ultraviolet radiation (UVR) includes UV-A with a wavelength range of 315-400 nm, UV-B with a wavelength range of 290-315 nm, and UV-C with a 100-290 nm wavelength range. Most UV-C radiation is absorbed by the ozone layer, preventing it from reaching the Earth's surface. UV-A and UV-B radiation, on the other hand, do get to the Earth's surface and can cause major health concerns such as skin cancer, sunburn, and premature aging. As a result, there is an increasing demand for lightweight clothing that protects against UV rays.(4)

The UV-protection properties of textiles depend on various factors, such as the type of fiber used, the way it is woven, the dyes used, and the finishing processes applied. To be considered excellent UV protection, clothing made of cotton fabric should have a UPF (Ultraviolet Protection Factor) rating between 40 and 50+. UPF measures how much UVR can penetrate the fabric and reach the skin. A higher UPF rating means better protection from UVR. (5) For example, a plain-weave cotton fabric

with a UPF rating of 10 is deemed insufficient for outdoor wearers. This means it allows a considerable quantity of UVR to get through and reach the skin, which can cause skin ageing, acne, skin reddening, and even skin cancer. As a result, it is critical to produce textiles with improved UV protection performance to protect human skin from the damaging effects of UVR. (4)

The two types of UV protection materials are commonly used in sunscreen and coated on fabric. Titanium dioxide (TiO_2) is more effective in UVB and zinc oxide (ZnO) in the UVA range. (6) TiO_2 is widely used as a transparent coating in self-cleaning windows due to its photocatalytic activity and ability to make surfaces superhydrophobic, carrying away dirt molecules. TiO_2 is non-toxic, cost-effective, and has favorable physical and chemical properties, making it useful in various applications such as paint, cosmetics, anti-pollution, and water purification.(7) In 2007, Abidi et al. treated cotton fabric with a solution containing nanoparticles of TiO_2. This treatment provided excellent protection against UVR, particularly in the UVB range (290-315 nm). The researchers found that the covalent linkages between the hydroxy (OH) groups of cellulose (a component of cotton) and the OH groups of the TiO_2 network offer the lifetime of the coating, which can be maintained after repeated home laundering. TiO_2 nanoparticles can absorb UVR, which protects the harmful UV rays. (8)

In 2022, Jongprateep et al. suggested using functional smart textiles for medical professionals at risk of infection during the COVID-19 pandemic. These textiles are coated with fluoropolymer-based precursors and TiO_2 to provide antibacterial and water-repellent qualities. According to the study, the average size of the TiO_2 particles was less than 200 nm, and they were evenly dispersed throughout the fabric. The fabric's ability to suppress the growth of microorganisms, particularly *Staphylococcus aureus* and *Klebsiella pneumoniae*, was evaluated before and after 10 wash cycles. The results demonstrated that the cloth effectively prevented bacterial growth after multiple washings. The study also tested the wettability by measuring the contact angle of water on the treated fabrics. The treated fabric exhibits strong water repellency with a water contact angle ranging from 120 to 139 degrees. According to a

water-repellency test, the coated materials maintained their water-repellent quality even after 10 washing cycles. (9)

Zinc oxide (ZnO) can be used to functionalize textile substrates and offer special multifunctional qualities like hydrophobicity, electrical conductivity, UV protection, flame retardancy, antimicrobial activity, thermal insulation, and moisture management. (10) In 2018, Khan et al. studied the development of a multifunctional cotton fabric with UV protection and superhydrophobic and antibacterial activity. The fabric was treated with formulations containing nanoparticles of ZnO or TiO_2, an optimized concentration of a repellent chemical and an organic-inorganic binder. The treated fabric showed promising results for all three functional properties and was durable for up to 20 washing cycles. The antibacterial properties of the fabric were evaluated against Gram-negative *E. coli* and Gram-positive *S. aureus* bacteria using the agar diffusion technique. (11)

Graphene oxide (GO) is a nanomaterial that can kill bacteria effectively. Due to its unique properties, graphene oxide is widely used in various applications such as biosensors, intracellular imaging, and drug delivery. It originates from a single layer of carbon atoms arranged in a two-dimensional lattice structure known as graphene. GO is produced by oxidizing graphene and introducing oxygen-containing functional groups to its surface. (12) In 2012, Krishnamoorthy et al. investigated the molecular-level interaction between GO and cotton fabric using Fourier-transform infrared (FTIR) spectroscopy, confirming the successful coating of GO onto the fabric. The GO-coated cotton fabric's antibacterial activity was examined against Gram-negative and Gram-positive bacteria, demonstrating higher toxicity towards Gram-positive bacteria. The antibacterial efficacy of GO-coated cotton fabric was assessed through a quantitative bacterial reduction test, which revealed a time-dependent reduction in bacterial growth when exposed to GO-coated fabrics. These results suggest the potential of GO-coated cotton fabric for biomedical applications, thereby enhancing healthcare practices. (13) In 2020, Zhou et al. developed conductive cotton fabric by dyeing them with graphene oxide and reducing them using hydrazine

hydrate. The fabric coated with graphene demonstrated excellent resistance to washing, friction, and bending. The materials maintained excellent conductivity levels of 86%, 55%, and 99% after 20 washing cycles, 2000 rubbing cycles, and 1000 bending cycles. The addition of graphene produced a dyed cloth with superior UV resistance and infrared absorption. (14)

This research aims to improve the cotton fabric's hydrophobicity, UV protection and antibacterial properties with the following strategies: the first step syntheses and characterizes the TNPsGZ composites. Next, TNPsGZ composites are used to coat cotton fabric. Finally, the coated fabric is evaluated for hydrophobicity, UV protection and antibacterial properties.

1.2 Objectives of the study

1. To synthesize TNPsGZ composites.
2. To examine the characteristics of the TNPsGZ composites.
3. To coat TNPsGZ composites on cotton fabric.
4. To investigate the characteristics of cotton fabric after being coated with TNPsGZ composites.
5. To determine the properties of cotton fabric after being coated with TNPsGZ composites.

1.3 Scope of the study

1. Synthesis of TNPsGZ composites using ultrasonic method.
2. Examine the characteristics of TNPsGZ composites:
   - Morphology using field emission scanning electron microscope (FE-SEM)
   - The chemical composition using Fourier transform infrared spectroscopy and Raman Spectroscopy.
   - The phase identification of crystalline materials using X-ray diffraction.
3. Coat cotton fabric with TNPsGZ composites through a dip-dry-cure method.

4. Examine the characteristics of cotton fabric after being coated with TNPsGZ composites:

- The morphology is studied using a scanning electron microscope

- The chemical composition is investigated using Fourier transform infrared spectroscopy.

5. Study the properties of cotton fabric after coated with composites:

- The hydrophobic properties are measured by contact angle measurement.

- The UV-protection properties are examined by UV-Vis spectrophotometer, modified AATCC (American Association of Textiles Chemists and Colorists) test method 183 (2014).

- The anti-bacterial properties are modified AATCC (American Association of Textiles Chemists and Colorists) test method 100 (2019).

1.4 Conceptual framework

1.5 Expected Outcomes

1. Obtain a coating composite that improves cotton fabric's hydrophobic, UV protection, and antimicrobial properties.

2. Published research on the coating of cotton fabric with composites.

CHAPTER 2
RESEARCH METHODOLOGY

2.1 Cotton Fabric

All regions of Thailand are suitable for cultivating cellulosic fiber, the natural material used to create cotton fabric. Cotton, a naturally occurring fiber extracted from the seedpod of the cotton plant, plays a crucial role in the production of various textiles. When viewed under a microscope, cotton fibers exhibit a twisted, ribbon-like appearance with a hollow center. Thanks to its versatility in blending with various other fibers and the ability to receive unique performance finishes, cotton has been cultivated for over 7,000 years and continues to gain popularity. (15) Cotton can be woven or knitted to produce textiles, with plain and twill weaves being the two most widely used techniques in cotton weaving. Fabric with a plain weave includes broadcloth, gingham, percale, and chambray. In contrast, twill weaves, which are used in gabardine, khaki, and denim, are known for their strength. The satin weave, although less common with cotton fibers due to its slightly dressier appearance, is found in high-sheen cotton fabric like sateen. (16)

Cotton fabric is popular because it is easy to care for and comfortable to wear throughout the year. Cotton can be easily cleaned by either laundering or dry cleaning, as shown in **Figure 1a**. It can withstand high water temperatures, but it is prone to shrinkage. Even with pre-washed fabric, most cotton fabric shrink during the first wash, so it is important to pre-wash again before sewing. In the case of printed cotton, most manufacturers recommend dry cleaning to preserve the design of the fabric. (17)

Due to the ordered arrangement and specific orientation of molecules in cotton cellulose, it is a highly crystalline and structured substance. The distinctive, elongated, and rigid molecular structure is referred to as α-cellulose. Cellulose molecules consist of β-1,4-D(+)-glucopyranose units linked together by 1,4-glucosidic

bonds, as shown in **Figure 1b**. Steric effects prevent the free rotation of the C-O-C linkage between the glucopyranose units, further enhancing the stiffness of the cellulose structure. Each glucopyranose unit contains three hydroxyl groups: one primary on C-6 and two secondaries on C-2 and C-3. These numerous hydroxyl groups, coupled with the chain-like structure, facilitate significant intra- and intermolecular hydrogen bonding in cellulose. These hydrogen bonds contribute to the increased rigidity of the cellulose structure, making it a durable and long-lasting material. (18)

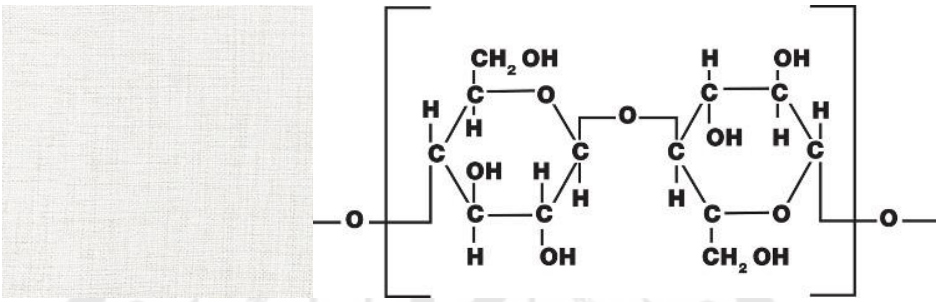

a. b.

Figure 1 Cotton fabric (a) and chemical structure of cellulose (b)
Source: https://barnhardtcotton.net/technology/cotton-pperties/

Table 1 Properties of cotton fabric
(19)

Property	Cotton fabric
Durability	Very good
Liquid absorbency	Excellent
Wrinkle resistance	Poor
Care	Machine wash

Cotton fibers are highly valued in the textile industry due to their breathability, absorbency, and versatility. These fibers allow air to pass through, preventing the buildup of heat and moisture, making cotton comfortable for clothing and household textiles. Its absorbent nature enables it to hold significant amounts of

moisture, up to 24-27 times its own weight, which makes it an ideal material for towels and washcloths. Furthermore, cotton's ability to absorb pigments and dyes easily enhances its versatility in color and design applications.

However, cotton has some notable drawbacks. It is prone to wrinkling, shrinking, and losing shape after repeated washing. Additionally, since cotton can retain moisture, it may take longer to dry and can become susceptible to mold or mildew growth in humid environments. Its natural absorbency also makes it more likely to stain and absorb dirt, requiring frequent washing and maintenance.(20) To address these limitations, there has been growing interest in enhancing cotton's functionality by integrating photocatalytic materials like titanium dioxide (TiO_2). TiO_2, especially in its anatase and rutile forms, can significantly improve the self-cleaning properties of textiles. This is due to its photocatalytic activity, which enables it to break down pollutants and organic compounds when exposed to light. By coating cotton fibers with TiO_2, the fabric retains its breathable and absorbent qualities while gaining the ability to degrade contaminants, thus reducing the need for frequent washing. This innovation not only addresses some of the disadvantages of cotton but also adds value to functional textile applications, promoting sustainability and convenience in everyday use.

2.2 Titanium dioxide (TiO_2)

TiO_2 is a metal that can be found in both plants and animals. Titanium, a transition metal, reacts with non-metallic oxygen to create this semi-metallic compound. It is a white solid with a molecular mass of 79.9 and melting and boiling points of 1830 and 2500 °C, respectively. As illustrated in **Figure 2**, TiO_2 is a semiconductor with three distinct crystal structures: anatase, rutile, and brookite. These structures are all composed of octahedral basic units (TiO_2^{6-}), with six oxygen atoms surrounding one titanium atom in each structure, resulting in a deformed octahedral arrangement at the faces, corners, and edges. (21)

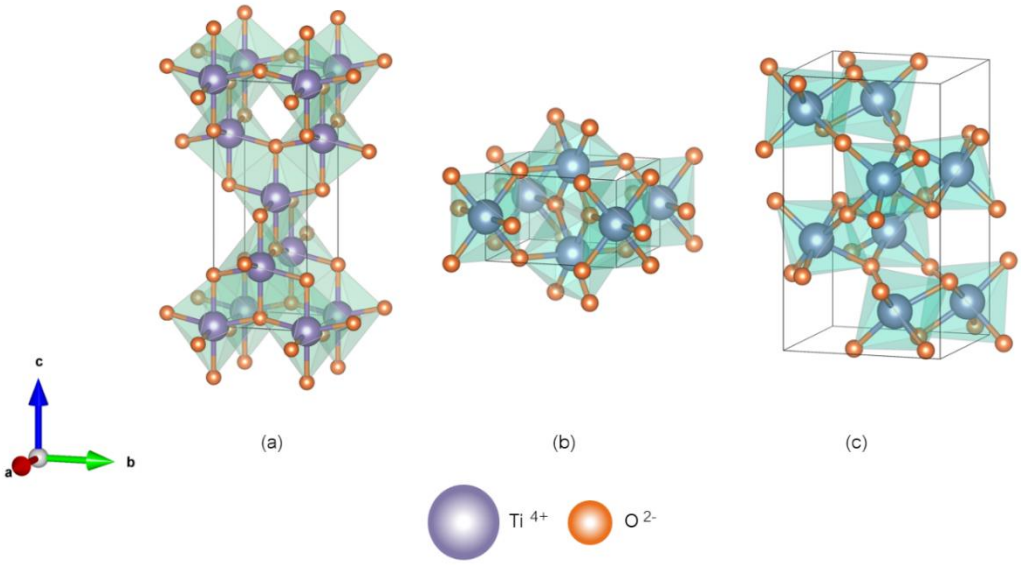

Figure 2 Titanium dioxide structure

(a) Anatase (b) Rutile (c) Brookite

2.2.1 Homophase

2.2.1.2 Anatase titanium dioxide

Anatase is one of three crystalline forms of TiO_2, as shown in **Figure 2a**. This specific polymorph has special qualities and photocatalytic activity. Because anatase has a larger band gap than rutile, it can oxidize more effectively and transfer electrons more easily. Because of this property, it has a smaller indirect band gap than a direct band gap and a lower conduction band than rutile, which makes it excellent for photocatalysis. Anatase has a bigger specific surface area, more active sites, and a higher oxygen vacancy concentration than rutile, which improves the efficacy of charge separation. It also shows a lower rate of recombination and a greater adsorption affinity for organic compounds. However, because rutile has more thermodynamic stability than anatase, anatase production is nevertheless limited in some situations. (22)

Table 2 Physical properties of Anatase titanium dioxide

(20)

Materials name	Anatase		
Composition	TiO_2		
System	Tetragonal		
a(Å), b(Å), c(Å)	3.7842(13)	3.7842(13)	9.5146(15)
α(deg), β(deg), γ(deg)	90	90	90
Unit cell volume	136.3		
D_x (g/cm^3)	3.89		

2.2.1.2 Rutile titanium dioxide

Rutile is one of the three crystalline forms of titanium dioxide, as shown in **Figure 2b**. At high temperatures, it is the most easily formed polymorph of TiO_2 and is also the most stable. Rutile can absorb UVR close to the visible spectrum because it has a lower band gap than anatase. Due to characteristics like its smaller specific surface area, rapid recombination rate, and the positive placement of its minimum conduction band, it exhibits less photocatalytic activity than anatase.

Rutile has received less interest in studies as a photocatalyst for the oxidation of pigments and organic compounds due to its poor oxygen absorption. Recent research has shown that rutile generated at low temperatures has higher photocatalytic activity than industrial P25 photocatalysts in the degradation of specific compounds. Rutile is useful in water separation systems because it allows for preferred water oxidation. The existence of vacancy-oxygen defects in rutile can significantly boost its photocatalytic activity because these defects hinder charge recombination. (22)

Table 3 Physical properties of Rutile titanium dioxide
(20)

Materials name	Rutile		
Composition	TiO_2		
System	Tetragonal		
a(Å), b(Å), c(Å)	4.593(2)	4.593(2)	2.959(2)
α(deg), β(deg), γ(deg)	90	90	90
Unit cell volume	62.42		
D_x (g/cm^3)	4.25		

2.2.1.3 Brookite titanium dioxide

Along with rutile and anatase, brookite is one of the three crystalline forms of titanium dioxide, as shown in **Figure 2c**. It can be created directly from anatase or by first converting anatase to brookite and then to rutile. It has an orthorhombic crystal structure. Crystallite size, size distribution, and crystallite contact area are only a few examples of the variables that affect brookite's stability. Brookite is more stable than anatase for crystal sizes larger than 11 nm, and rutile becomes the most stable phase for sizes larger than 35 nm.

Despite having a smaller specific surface area than other TiO_2 polymorphs, brookite has unique photocatalytic characteristics as well as increased photoactivity. The presence of Ti_4 flaws has been discovered to increase the photocatalytic activity of brookite, which is highly dependent on the amount of these defects. Research revealing brookite is favorable influence on the oxidation of certain compounds provides additional support for its usefulness in diverse applications. (22)

Table 4 Physical properties of Brookite titanium dioxide
(20)

Materials name	Brookite		
Composition	TiO_2		
System	Orthorhombic		
a(Å), b(Å), c(Å)	9.174(2)	5.449(2)	5.138(2)
α(deg), β(deg), γ(deg)	90	90	90
Unit cell volume	257		
D_x (g/cm^3)	4.13		

Anatase, with its superior photocatalytic properties and larger surface area, is ideal for applications requiring high reactivity. On the other hand, rutile, being the more thermodynamically stable form, also plays a crucial role in various industrial applications. The interaction between anatase and rutile phases, particularly in mixed-phase systems, offers enhanced photocatalytic efficiency due to their complementary properties. The next section will explore the synergistic effects of anatase and rutile combinations and their impact on photocatalytic performance.

2.2.2 Anatase/Rutile

Anatase has greater photocatalytic activity than rutile. A mixture of anatase and rutile, however, has greater photocatalytic activity than a single anatase. Of the three forms of TiO_2, rutile is the most stable. Because brookite and anatase are metastable forms, they are not thermodynamically stable and can change into different states under specific circumstances. Due to rutile stability, anatase and brookite can change into it at high temperatures. It is usual practice to control the calcination temperature to generate TiO_2 with a blend of anatase and rutile phases. (22)

2.2.2.1 Degussa P25 Titanium dioxide

Degussa P25 TiO_2 in photocatalytic reaction systems. This substance is composed of anatase and rutile crystallites in a specific ratio. It has unique features that make it suitable for widespread environmental applications due to its low cost, high photoactivity, chemical stability, reactivity, and biocompatibility.

Degussa P25 consists of two crystalline phases of TiO_2: anatase and rutile. The band gap of anatase is 3.2 eV, which is higher than the 3.0 eV band gap of rutile. Despite its higher band gap, anatase typically exhibits better photocatalytic properties compared to rutile. P25, which contains anatase and rutile in a 3:1 ratio, demonstrates superior photocatalytic compared to anatase alone. This enhanced performance is due to the synergistic effect that arises from the coexistence of both phases, as the combination improves electron-hole separation and prolongs charge carrier lifetimes.

The specific anatase-to-rutile ratio in P25 significantly influences its photocatalytic efficiency and ability to adsorb pollutants. As Spurr and Myers demonstrated, the ratio of anatase and rutile can be determined with precision using X-ray diffraction, which allows for the optimization of P25's composition in applications where photocatalytic efficiency is critical. The controlled proportions of these two polymorphs are a key factor in the material's effectiveness in decomposing pollutants and other environmental contaminants. (23,24)

In 2013, Pisitsak et al. investigated the self-cleaning properties of cotton fabric coated with nanoparticles of TiO_2 or mixtures of TiO_2 and fumed silica. The results show that all samples possess self-cleaning abilities, with stronger effects observed for higher TiO_2 concentrations. The use of TiO_2 nanoparticles on cotton fabric enhances self-cleaning efficiency via two separate mechanisms: a dye-sensitization mechanism through exposure to visible light and a classical UV-stimulated photocatalytic action. The study also found that the addition of fumed silica reduced the fabric's self-cleaning ability. (25)

2.2.2.2 Spurr and Myers

Anatase and rutile are two polymorphs of titanium dioxide, which exhibit different crystallographic structures and physical properties. These forms are often present together in natural or synthetic TiO_2 samples, and determining their proportions is critical for applications that depend on their distinct properties, such as dielectric behavior. The method developed by Spurr and Myers is based on the fact that the scattering intensity for each component in a mixture is proportional to its weight fraction. The XRD pattern for a mixture of anatase and rutile shows characteristic peaks corresponding to each phase, and the ratio of the intensities of these peaks can be used to determine the proportion of each phase in the mixture.

The analysis is based on the ratio of the intensity of the strongest anatase reflection (I_A) to the intensity of the strongest rutile reflection (I_R). This intensity ratio (I_A/I_R) provides an index of the sample composition. If the material is pure anatase, the ratio will approach infinity, and if it is pure rutile, the ratio will approach zero. The following equations describe the relationship between the weight fractions of anatase (W_A) and rutile (W_R) in the sample and their respective intensities (23,24) :

$$\frac{I_A}{I_R} = K \cdot \frac{W_R}{W_A}$$

X-ray diffraction (XRD) is the primary technique employed to distinguish between the anatase and rutile phases in a TiO_2 sample. The distinct crystal structures of anatase and rutile lead to different diffraction patterns, with each phase exhibiting unique peaks at specific diffraction angles. The ratio of the diffraction intensities I_R and I_A, where I_R represents the intensity of the strongest rutile peak, and I_A represents the strongest anatase peak, forms the basis of the quantitative analysis. The relative phase content is determined using the empirically derived formula (23,24) :

$$\frac{W_R}{W_A} = 1.22 \cdot \left(\frac{I_R}{I_A}\right) - 0.0281$$

Where:

- W_R is the weight fraction of rutile,
- W_A is the weight fraction of anatase,
- I_R and I_A are the intensities of the rutile and anatase diffraction peaks, respectively.

Spurr and Myers derived the coefficient 1.22 for the ratio of the diffraction intensities between rutile and anatase from their experiments. This coefficient adjusts the intensity ratio $\frac{I_R}{I_A}$ to accurately represent the relative weight fractions of the two phases. The value 1.22 ensures that the equation scales the intensity ratio properly, reflecting the actual phase proportions in the sample. The constant 0.0281 was introduced to correct for baseline errors and minor amounts of rutile that may be present even in samples that are predominantly anatase. In real-world XRD measurements, even in a nearly pure anatase sample, there might still be a detectable signal from rutile due to:

- Instrumental noise or background interference that affects the XRD data.
- Trace amounts of rutile impurities that are present in samples marketed or processed as pure anatase.

By subtracting 0.0281, the formula compensates for this inherent background signal from rutile, ensuring that the calculated phase fraction is not overestimated when rutile is present in very small amounts. Thus, this correction factor refines the accuracy of the calculation, particularly for samples with low rutile content.(24)

X-ray diffraction is not only useful for phase identification but also for determining the particle size of nanomaterials. The Scherrer equation is the most commonly employed method to estimate the average crystallite size from XRD data. The Scherrer formula relates the broadening of diffraction peaks to the crystallite size, assuming that the broadening is due to the small size of the crystallites. The formula is expressed as (26):

$$D = \frac{K\lambda}{\beta \cos\theta}$$

Where:

- D is the particle size perpendicular to the lattice planes (in nanometers).
- K is the shape factor, usually taken as 0.9.
- λ is the X-ray wavelength (in Å).
- β is the full-width at half-maximum (FWHM) of the diffraction peak in radians.
- θ is the Bragg angle corresponding to the diffraction peak.

This method assumes that peak broadening is primarily due to particle size, neglecting other contributions such as strain. Therefore, it provides an approximate particle size and works best for small crystallites (generally < 100 nm). The Scherrer formula does not account for overlapping peaks or instrumental broadening.

The unique photocatalytic performance of Degussa P25, a mixture of anatase and rutile phases, demonstrates the advantages of combining different crystal structures of TiO_2. Similarly, zinc oxide (ZnO), another semiconductor, has gained attention for its excellent photocatalytic properties and UV-blocking abilities. ZnO, like TiO_2, can enhance the functional properties of textiles, particularly in UV protection and antibacterial applications. The following section delves into the properties of zinc oxide and its potential applications in textile technologies.

2.3 Zinc oxide (ZnO)

Zinc Oxide has the molecular formula ZnO. It appears as a fine white powder. Many people recognize it as 'calamine' or a substance used to treat skin irritation because zinc oxide has antibacterial properties. ZnO is a semiconducting material with a wide band gap and a large exciton binding energy, making it an efficient photocatalyst with high surface reactivity, reaction rates, and mineralization rates. (10) One-dimensional structures, such as nanowires or nanorods, are ideal for photocatalytic applications due to their large surface-to-volume ratio compared to thin films. ZnO is a material that has received extensive research for its potential use in optoelectronic components like solar cells, LEDs, and lasers. To fully harness the practical applications of ZnO, it is essential to conduct research on the development of high-quality ZnO films and the achievement of reliable p-type conductivity in ZnO.

It has three different crystal structures: Zincblende, Rocksalt and Wurtzite, as shown in **Figure 3**. ZnO three crystal forms exhibit inversion symmetry, meaning that they are not symmetrical when viewed from a point or plane. Due to the way the atoms are arranged in the crystal structure, which causes an unequal distribution of charges, ZnO lacks inversion symmetry. ZnO crystal exhibits crystallographic polarity, which refers to the orientation of the bonds in the crystal structure, as a result of this lack of symmetry. (27)

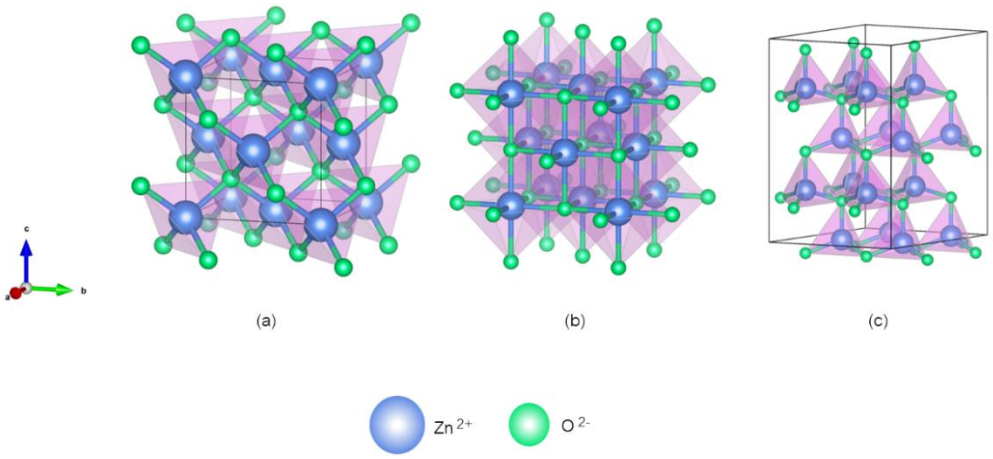

Figure 3 Zinc oxide

(a) Zincblende (b) Rocksalt (c) Wurtzite

2.3.1 Zincblende

A common crystal structure in some substances, such as zinc sulfide (ZnS), is called zincblende. Each atom in the face-centered cubic (FCC) structure of the crystal is surrounded by four atoms of the opposite kind. This is a particular kind of cubic crystal lattice, as shown in **Figure 3a**. When it comes to zincblende, four sulfur (S) atoms and four zinc (Zn) atoms are tetrahedrally coordinated. In the context of ZnO, the zincblende structure is significant because it can be maintained by growing on cubic substrates like ZnS. It must be noted that ZnO itself has a different crystal structure known as wurtzite, although, under specific conditions, the cubic zincblende structure can be obtained. The differentiation between diverse crystal structures is important because it influences many material behaviors and properties. (27)

2.3.2 Rocksalt

The sodium chloride (NaCl) structure is a particular crystal structure that is referred to as "rock salt." Six chloride ions surround each sodium ion, and vice versa, in this sort of cubic crystal lattice, as shown in **Figure 3b**. In contrast to other structures like wurtzite, the rock salt structure may be created at relatively high pressures and is characterized by a decrease in the lattice constant. The rock salt structure is discussed about the high-pressure phase transition of ZnO from wurtzite to rock salt structure in the context of the sources that were presented. About the epitaxial development of rock-salt MgO on sapphire substrates, it is also mentioned. In contrast to other crystal structures, the rock salt structure has unique qualities and uses, and it is crucial for research in several areas, including solid-state physics and materials science. (27)

2.3.3 Wurtzite

A common crystal structure in several substances, such as ZnO, is wurtzite. In this type of hexagonal crystal lattice, each atom is surrounded by four atoms of the opposing type, forming a hexagonal unit cell. In the case of wurtzite, four oxygen (O) atoms and four zinc (Zn) atoms are tetrahedrally coordinated, as shown in **Figure 3c**. The wurtzite structure is the thermodynamically stable and technologically intriguing

structure of ZnO. Its particularly significant surfaces include the (0001) or basal plane, the d1120Th plane, and the d1100Th plane. The (0001) plane is the most used surface for growth. In contrast, the other two planes are important for Reflection High Energy Electron Diffraction (RHEED) observations in Molecular Beam Epitaxy (MBE) growth. (27)

Common coating techniques for this purpose include dip-coating, sol-gel, padding, electro-deposition, and chemical bath deposition. These application techniques involve depositing nano- and micro-sized ZnO particles onto a specific textile substrate. ZnO particles can be produced in situ using various methods, including sol-gel, solvothermal, hydrothermal, precipitation, ultrasonic, mechanochemical, and microwave procedures, or they can be deposited as a previously prepared suspension. The accurate functional requirements of the textile substrate determine the application method to be used. For instance, depositing a uniform layer of ZnO particles on the textile substrate can be achieved through the quick and affordable dip-coating technique. The functional qualities of the textile substrate can be further enhanced by increasing the ZnO particle concentration and using doping and coupling agents. The endurance of ZnO coatings can also be increased by using binding and seeding chemicals. (10) In 2017, Arputharaj et al. developed a durable multi-functional finish for cotton fabric by directly synthesizing nano zinc oxide (nano-ZnO) particles in the pores of the fibers, resulting in excellent antibacterial activity and UV protection even after multiple washes. The research focused on cotton fabric utilizing in situ generated nano-ZnO particles, which are synthesized directly in the pores of the cotton fibers. This process led to excellent antibacterial properties and UV protection that remained effective even after multiple washes. Furthermore, the finished fabric retained its inherent physical and mechanical properties with minimal impact on its overall quality. The concentration of precursors used for in situ synthesis influenced the quantity of nano-ZnO loaded onto the fabric, and the optimal quantity of ZnO was retained even after laundering, ensuring the long-term durability of its antibacterial and UV protective properties. (28)

Table 5 Comparative properties of TiO_2 and ZnO
(29)

Parameter	Unit	Titanium dioxide	Zinc oxide
Molecular weight	g/mole	79.87	81.40
Appearance, existence		White powder	White powder
Odor		Odorless	Odorless
Structure		Tetragonal	Hexagonal wurtzite
Solubility		Insoluble in water	Insoluble in H_2O and alcohol, but soluble in acids and bases
Energy gap	eV	3.2	3.37
Density	g/cm^3	3.895	5.606
Lattice constants	nm	a= 0.3758, c= 0.9514	a= 0.3296, c= 0.52065
Boiling point	K	3245	2633.15
Melting point	K	2116	2248.15
Refractive index	n_D	2.488	2.0041

2.4 Photocatalytic Mechanism

Photocatalytic mechanisms rely on the generation of electron-hole pairs when semiconductor materials are exposed to UV light as shown in **Figure 4**. In TiO_2/ZnO composites, this mechanism is enhanced by the transfer of electrons across a heterojunction, which reduces electron-hole recombination. ZnO, upon UV exposure, generates electron-hole pairs, and the excited electrons then transfer to TiO_2's conduction band, where they are at a lower energy level. This electron transfer helps maintain charge separation, allowing TiO_2 to capture electrons while ZnO facilitates oxidation reactions through its holes. The overall process supports sustained photocatalytic activity, promoting pollutant degradation as shown in **Figure 5**. (30–33)

Additionally, both ZnO and TiO_2 block UV radiation due to their wide band gaps, which contributes to material protection while supporting photocatalytic processes. Advanced configurations like the Z-scheme can further enhance redox reactions, promoting longer carrier lifetimes and more efficient electron flow factors that are critical for effective pollutant degradation. (33,34)

Integrating carbon-based materials, such as graphene oxide (GO), into TiO_2/ZnO composites improves electron mobility and surface reactivity. This enhancement facilitates charge transfer and reduces recombination rates, making TiO_2/ZnO composites highly suitable for environmental applications. (34,35)

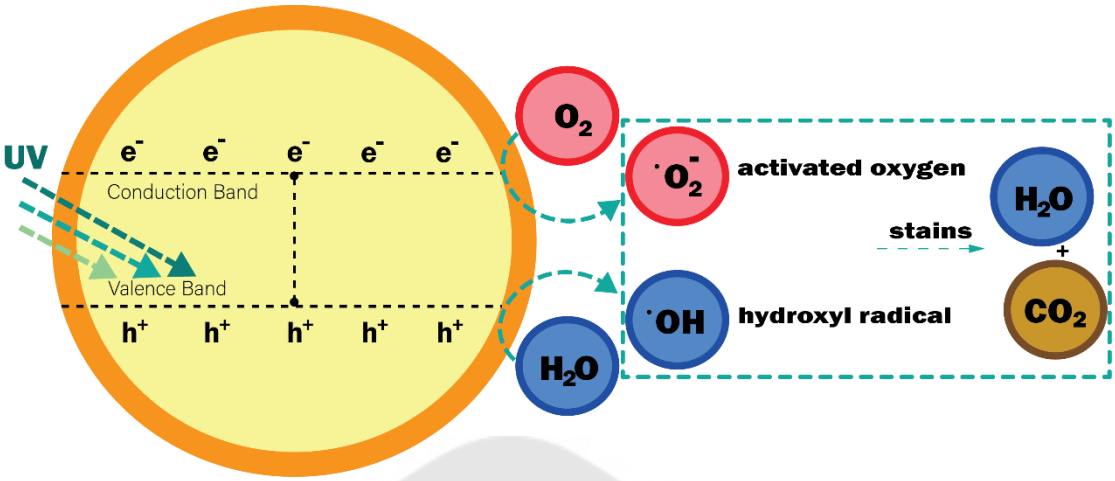

Figure 4 Illustrates the generation of e^- - h^+ pairs in TiO_2/ZnO under UV light exposure, enhancing photocatalytic efficiency by reducing charge recombination.

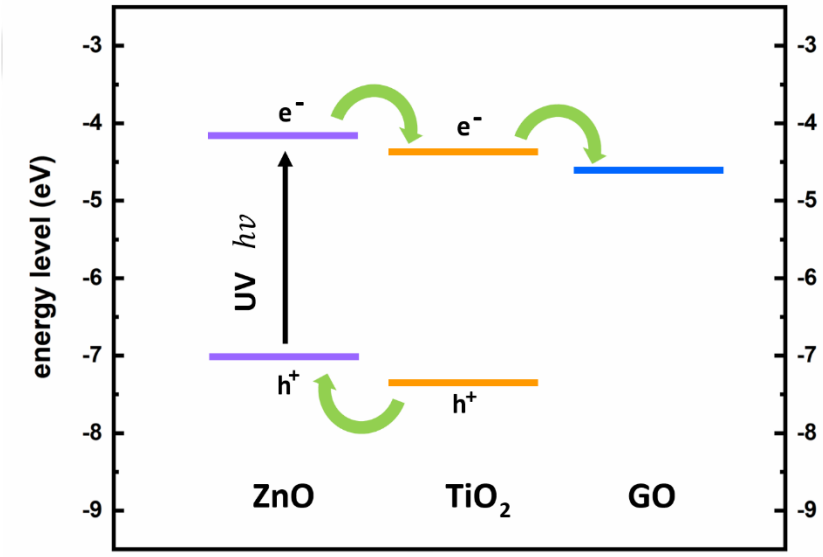

Figure 5 Shows the energy band alignment in the TiO_2/ZnO/GO composite, facilitating electron transfer and reducing e^- - h^+ recombination.

2.5 Comparison of Graphite, Graphene Oxide, and Reduced Graphene Oxide

2.5.1 Graphite

Graphite is a naturally occurring crystalline form of carbon with a layered structure. Strong covalent C-C bonds hold each layer together, while weaker van der Waals forces connect the layers. This structure makes graphite thermodynamically stable and electrically conductive, leading to its use in applications such as electrodes, lubricants, and thermal management materials. Graphite is categorized into vein, flake, and amorphous types, with flake graphite being the most commonly used due to its widespread availability and excellent conductivity. (36)

2.5.2 Graphene oxide (GO)

Graphene oxide (GO) is synthesized through the oxidation of graphite, introducing oxygen-containing functional groups such as epoxy, hydroxyl, and carboxyl into its layered structure. These groups render GO hydrophilic, facilitating its dispersion in water and various solvents. Owing to its enhanced reactivity compared to pristine graphite, GO serves as an essential precursor for producing graphene and reduced graphene oxide (rGO). Its versatile applications span across fields like composites, sensors, and biomedical devices. (37)

Structurally, GO consists of layered carbon sheets with oxygen functional groups attached both on the surfaces and along the edges, as shown in **Figure 6**. GO can appear as a single-layer material or in multilayer forms. For instance, a single layer is referred to as graphene oxide, while a few-layered GO comprises two to five layers. Beyond five layers, GO becomes multilayered, and materials with eleven or more layers revert to the classification of graphite oxide. (38)

As a 2D nano-inorganic filler, GO significantly enhances material properties even when added in minute quantities (less than 2 wt% of the matrix). The oxygen functional groups on its surface not only improve chemical activity but also promote homogeneous dispersion within polymer matrices. These groups enable strong interfacial bonding, which creates robust percolation networks, improving the mechanical and thermodynamic performance of composites. Additionally, GO's inherent

UV shielding properties further endow these materials with excellent resistance to ultraviolet radiation. (36,37)

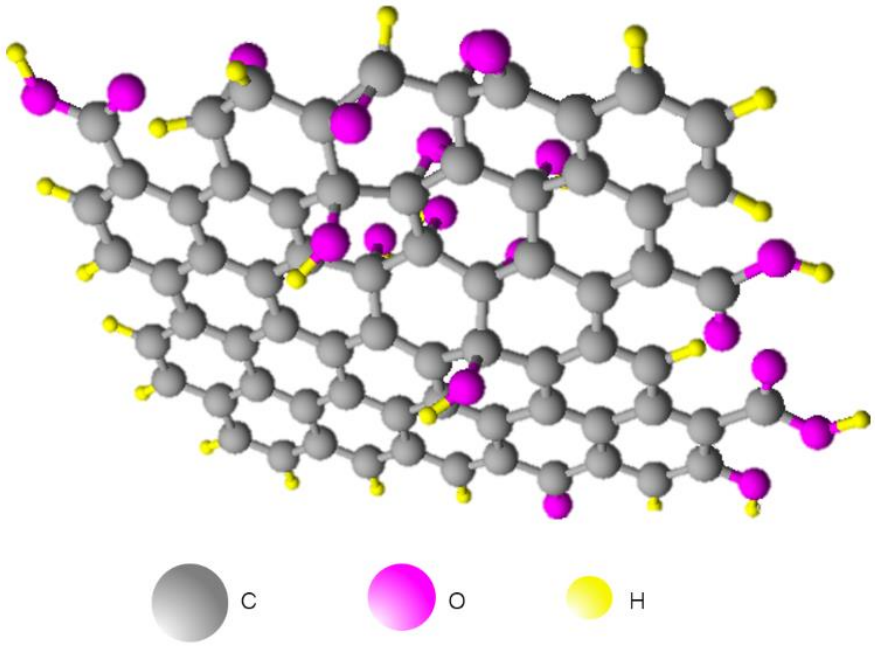

Figure 6 3D structure of Graphene Oxide

2.5.3 Reduced graphene oxide (rGO)

Reduced graphene oxide is produced by reducing graphene oxide to remove some or all of the oxygen-containing groups, resulting in a material that is more similar to pristine graphene but retains some residual functional groups and defects. rGO exhibits improved electrical conductivity and mechanical properties compared to GO, though not as high as pristine graphene. It finds applications in energy storage, conductive films, and as a catalyst support. (37,39)

2.5.4 Characterization

2.5.4.1 Fourier transform infrared (FTIR)

FTIR spectra reveal key functional groups in graphite, GO, and rGO, as shown in **Figure 7**. For graphite, no significant peaks are observed, indicating the absence of oxygen-containing functional groups, typical for pure graphite. In contrast, GO shows several distinct peaks: a broad peak at 3 4 2 0 cm^{-1} corresponding to O-H stretching (hydroxyl group), a peak at 1739 cm^{-1} representing C=O stretching (carboxyl group), and peaks at 1226 cm^{-1} and 1015 cm^{-1} related to C-O-C (epoxy group). These peaks confirm that oxygen functional groups have been introduced during the oxidation process, transforming graphite into GO. For rGO, the intensity of these peaks decreases significantly, particularly the broad O-H stretching peak at 3 4 2 0 cm^{-1}, indicating the successful removal of oxygen functional groups during the reduction process. However, some residual oxygen functional groups remain, suggesting that the reduction process was not complete. (37)

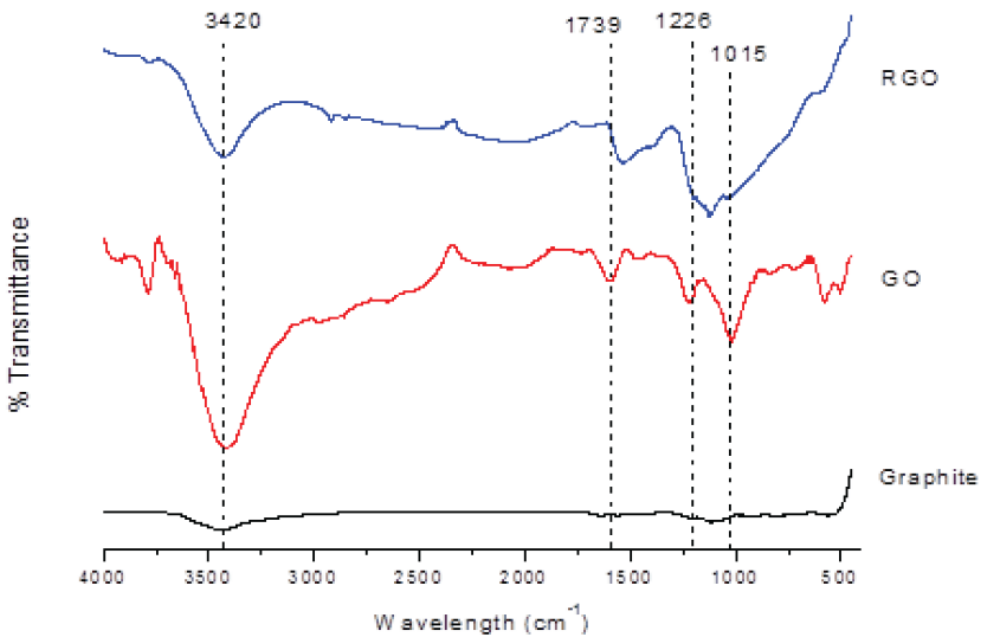

Figure 7 FTIR spectra of graphite, GO, and rGO

Source: http://dx.doi.org/10.1063/1.5005764

2.5.4.2 Raman spectroscopy

Raman spectroscopy provides insight into the structure and disorder of the materials, as shown in **Figure 8**. GO exhibits both G and D bands, with the D band at around 1350 cm^{-1} indicating the presence of defects and disorder introduced by the oxidation process G band at around 1580 cm^{-1}, corresponding to the in-plane vibrations of sp^2-hybridized carbon atoms. The ID/IG ratio, which represents the level of disorder, is higher in GO compared to graphite due to the introduction of oxygen functional groups that disrupt the sp^2 network. For rGO, the D band becomes more prominent, reflecting an increase in defects as some of the sp^2 network is restored but with additional structural irregularities introduced during the reduction. The increase in the ID/IG ratio in rGO suggests that while reduction removes some oxygen groups, it also introduces more localized defects, resulting in smaller sp^2 domains. (37)

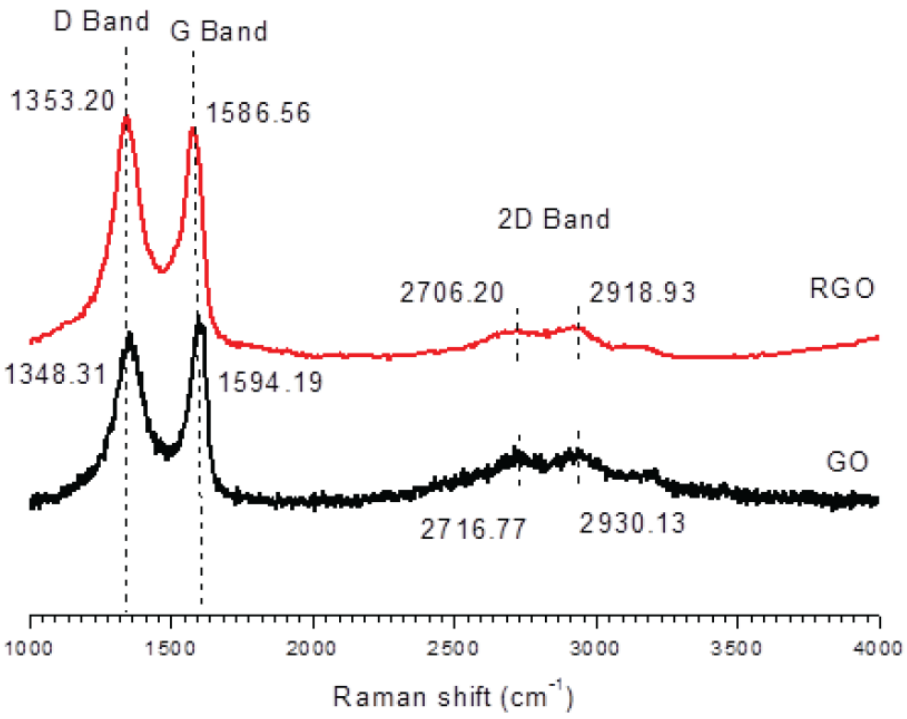

Figure 8 Raman spectra of GO, and rGO

Source : http://dx.doi.org/10.1063/1.5005764

2.5.4.3 X-ray Diffraction (XRD)

XRD results show the crystalline structure and interlayer spacing of graphite, GO, and rGO, as shown in **Figure 9**. Graphite displays a sharp peak at 2θ = 26.62°, indicating a well-ordered crystalline structure with a layer spacing of 0.3346 nm. In GO, this peak shifts to 9.03°, signifying an increase in the interlayer spacing to 0.9794 nm due to the intercalation of oxygen-containing groups between the graphene layers. After reduction, the XRD peak for rGO shifts to 24.10°, reflecting partial restoration of the graphitic structure but with a broader and less intense peak, indicating a more disordered arrangement. The interlayer spacing decreases to 0.3689 nm, showing that many oxygen groups have been removed, allowing the layers to come closer together. However, the material still lacks the crystallinity of pure graphite. (37)

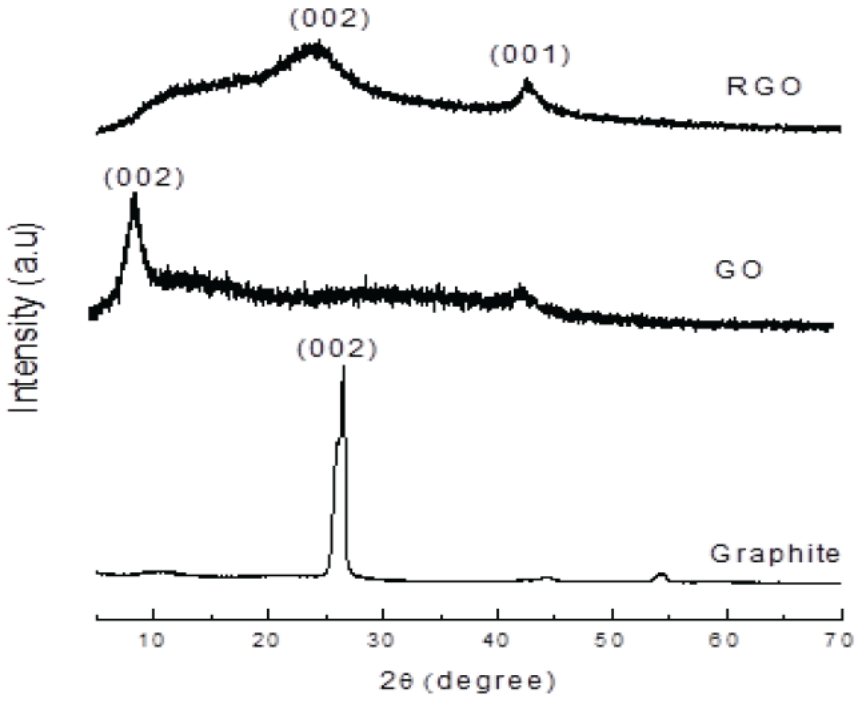

Figure 9 XRD spectra of graphite, GO, and rGO

Source : http://dx.doi.org/10.1063/1.5005764

2.5.4.4 Scanning Electron Microscope (SEM)

SEM images reveal the surface morphology of the materials, as shown in **Figure 10**. Graphite shows a smooth, platelet-like structure, typical of its crystalline form. In GO, the surface appears wrinkled and consists of layered flakes, indicating successful oxidation and exfoliation of the graphite layers. For rGO, the SEM image shows crumpled thin sheets, reflecting the partial restoration of the graphite-like structure after reduction. The disordered and folded appearance of rGO sheets suggests that while the reduction process restores some of the graphene layers, the material remains structurally disorganized compared to the original graphite. (37)

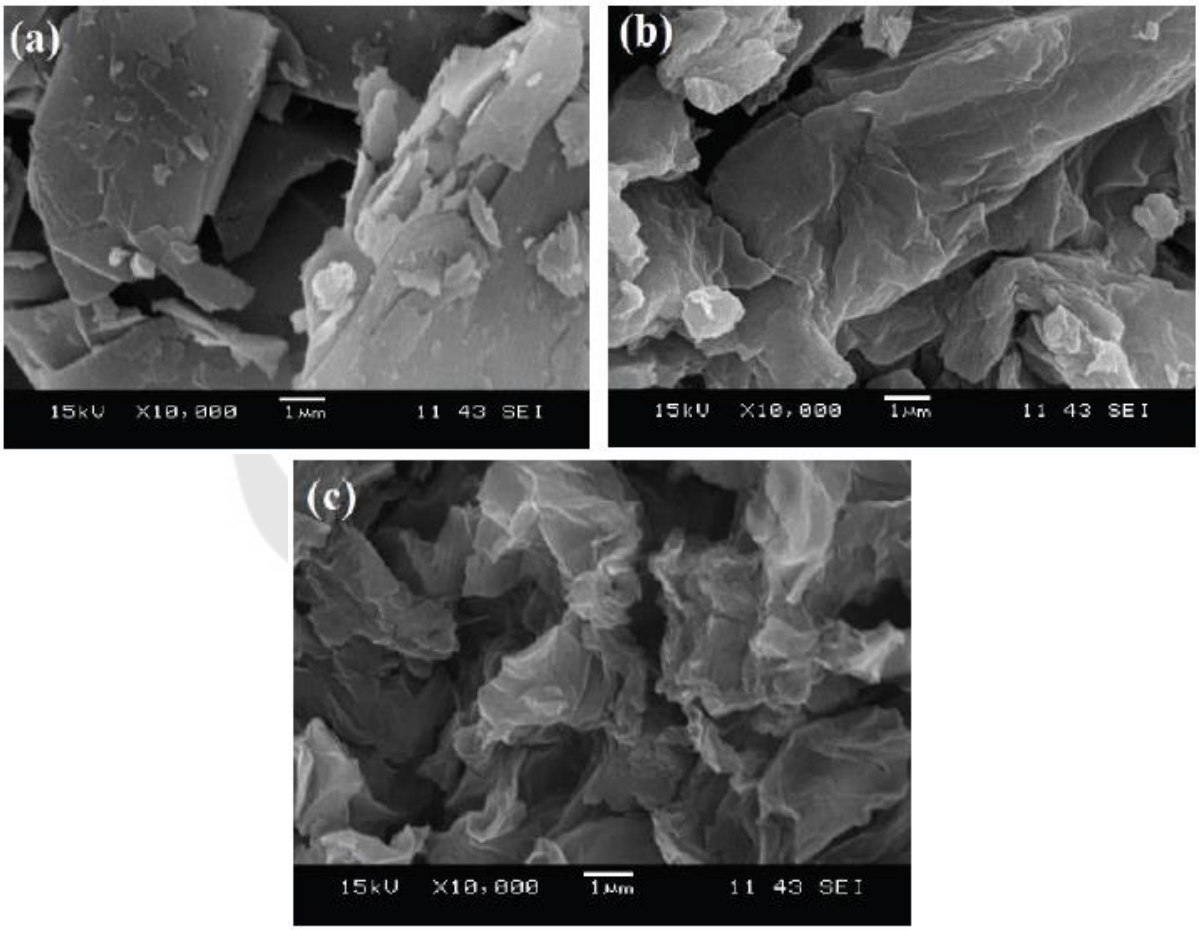

Figure 10 SEM micrograph of a) graphite, b) GO, and c) rGO

Source: http://dx.doi.org/10.1063/1.5005764

Table 6 Comparison of Graphite, Graphene Oxide, and Reduced Graphene Oxide (37)

Parameter	Graphite	GO	rGO
Structure and Composition	Layered structure with strong in-plane covalent bonds and weak interlayer van der Waals forces.	Similar layered structure but with various oxygen-containing groups disrupting the sp^2 hybridization and increasing interlayer spacing.	Reduced oxygen content compared to GO, partially restoring the sp^2 network, but still contains some defects and functional groups.
Chemical Reactivity	Relatively inert, with applications leveraging its stability and conductivity.	Highly reactive due to oxygen functionalities, useful for chemical modifications and as a precursor to graphene materials	Intermediate reactivity; retains some functional groups, making it useful in various chemical and physical applications.
Applications	Used in high-temperature applications, as electrodes in batteries, and in lubricants and pencils.	Employed in composites, biomedical devices, sensors, and as a precursor for rGO and graphene.	Utilized in energy storage devices, conductive films, catalysis, and flexible electronics.

From the comparisons made, Graphene Oxide (GO) demonstrates notable potential in enhancing UV protection, particularly when integrated with other materials. Its structure allows for improved dispersion in composite systems, which can significantly boost the material's ability to block harmful ultraviolet radiation. When combined with UV-absorbing materials like TiO_2 and ZnO, GO contributes to the creation of fabrics and coatings that offer superior UV shielding, ensuring better protection against both UVA and UVB rays. This makes GO an attractive candidate for applications requiring enhanced UV resistance.

Zuo et al. focus on enhancing the UV-blocking properties of cotton fabrics by applying a nanocomposite coating made from graphene oxide (GO) and zinc oxide (ZnO) quantum dots. Cotton, despite its popularity for summer clothing, lacks inherent UV protection, which this study aims to improve. The researchers used a water-based self-assembly process to coat the surface-modified cotton fabric with a GO/ZnO composite, resulting in a durable and effective UV-blocking material. The treated cotton fabric demonstrated a UPF (Ultraviolet Protection Factor) of 61.3, indicating excellent UV protection. Even after 20 wash cycles, the fabric maintained a high UPF of 57.6, showcasing its durability. The study concludes that the combination of GO and ZnO quantum dots offers significant potential for developing textiles with long-lasting UV protection. (40)

The integration of TiO_2, ZnO, and GO in composite coatings enhances the multifunctionality of treated fabric. TiO_2 and ZnO are known for their superior photocatalytic and UV-blocking properties, particularly in the UVA and UVB ranges, providing robust UV protection. When combined, these materials synergistically absorb and scatter harmful ultraviolet (UV) radiation, offering comprehensive defense against solar exposure.

From previous research, Krishna et al. investigated the optical limiting properties of Graphene Oxide (GO) nanocomposites functionalized with ZnO and TiO_2, demonstrating that these materials exhibit nonlinear optical absorption that limits light transmission at high intensities, particularly at wavelengths of 532 nm and

1064 nm. This capability makes the GO-ZnO/TiO_2 composites suitable for applications in optoelectronic and photonic devices, where they protect sensitive sensors from intense light exposure. (41)

Building on this, El-Shafai et al. focused on the antibacterial and photocatalytic activities of GO-based nanocomposites decorated with ZnO and TiO_2, highlighting their potential in water treatment and sterilization. Their findings revealed that the combination of GO with these metal oxides enhances reactive oxygen species (ROS) production, facilitating effective degradation of organic pollutants and inhibition of bacterial growth. Together, these studies emphasize the functional adaptability of GO when integrated with ZnO and TiO_2, providing enhanced stability and reactivity beneficial to environmental and optical applications. (42)

This study by M.K. Murali, V. Sri Priyanka, and M. Abdur Rahman focuses on synthesizing ZnO-TiO_2-GO nanocomposites (ZTGO) using a one-pot precipitation method to create biocidal agents for healthcare applications. XRD and SEM analyses confirmed the structural and morphological integrity of the ZTGO, with GO sheets decorated by ZnO-TiO_2 nanoflakes, providing a larger surface area. The presence of oxygen groups and vacancies, as shown by FTIR and PL spectroscopy, facilitates reactive oxygen species (ROS) production, enhancing the composite's biocidal properties. The ZTGO nanocomposite demonstrated effective antibacterial activity against *S. aureus* and *E. coli*, surpassing standard antibiotics. Also, it showed promising anticancer effects on liver cancer cells with an IC50 of 52.72 µg/mL. The researchers aim to address challenges in managing drug-resistant bacterial infections and cancer with a cost-effective and biocompatible alternative suitable for clinical applications. (43)

In addition to UV protection, this composite structure significantly contributes to the hydrophobicity of the fabric. The combination of TiO_2, ZnO, and GO helps create a water-repellent surface. (44) TiO_2 and ZnO nanoparticles play a crucial role in enhancing surface roughness, which is essential for hydrophobicity. This surface roughness encourages water droplets to bead and roll off,

preventing moisture absorption and keeping the fabric dry. Furthermore, the inclusion of ZnO and TiO_2 nanoparticles provides antibacterial properties through the generation of reactive oxygen species (ROS), which disrupts bacterial cells. (43) The presence of GO in the composite further enhances these biocidal effects, contributing to the fabric's resistance to microbial contamination. Overall, this combination ensures that the fabric remains durable, water-repellent, and resistant to bacterial growth.

2.6 Hydrophobicity and Hydrophilicity

A surface or material that can clean itself without assistance from outside is said to be self-cleaning. It entails cleansing the surface of dirt, dust, or other impurities, usually using water or other cleaning agents. Self-cleaning materials and coatings have drawn a lot of attention because of their numerous uses across a variety of industries.

Hydrophobic coatings make water droplets slide and roll over the surface, carrying dirt away with them. On the other hand, hydrophilic coatings use metal oxides to sheet the water, removing dirt from the surface, as shown in **Figure 11**. (45)

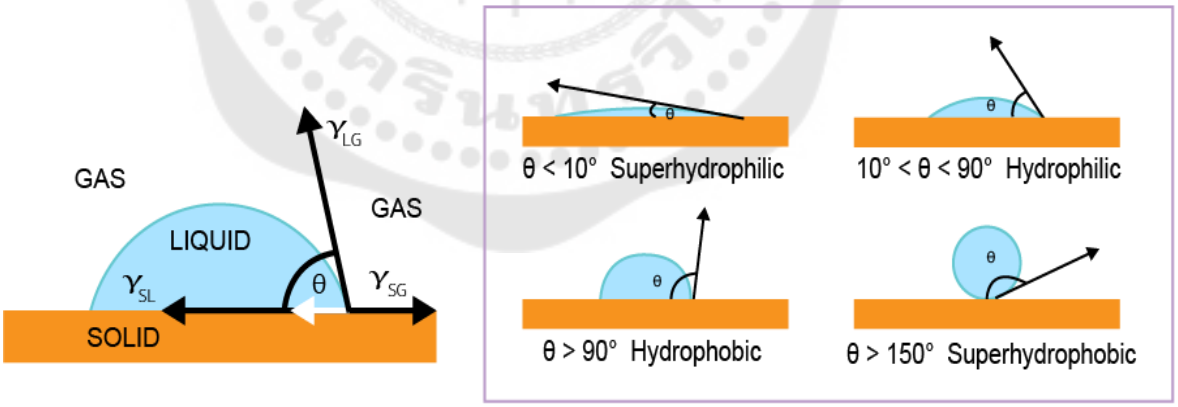

Figure 11 Schematics Illustrating the differences between hydrophilic and hydrophobic surface properties in wetting behavior.

2.6.1 Hydrophilic surfaces

Water droplets spread out and create a thin layer over hydrophilic surfaces, which have a strong affinity for water. This prevents water droplets from beading up. Low water contact angles, typically less than 90 degrees, define these surfaces. Hydrophilic coatings are crucial for many different applications, including windows, solar panels, cement, and paints. The creation of hydrophilic coatings requires the use of substances and synthetic processes that encourage water absorption and surface wetting. Modifying a material's surface energy and surface roughness can result in hydrophilic surfaces. By encouraging the simple removal of dirt and impurities through water droplets, hydrophilic coatings can improve the self-cleaning abilities of surfaces and reduce the need for manual cleaning. (45)

2.6.2 Hydrophobic surfaces

Water beads up and rolls off of hydrophobic surfaces, which are surfaces that reject water. The water contact angle of these surfaces is high, usually more significant than 90 degrees. Surface roughness improves hydrophobicity and can be attained using substances like fluorinated polymers. Many items, such as self-cleaning, stain-repellent textiles, and anti-corrosion coatings, can be made using hydrophobic surfaces. Nanoparticles, which can be manufactured with uniform size and regulated by the Stober method, can be used to control the roughness of the surface. The superhydrophobic qualities of lotus leaves, which result from the presence of epicuticular wax crystalloids, are an example of hydrophobic materials that can also be found in nature. (45)

2.7 UV-protection of cotton fabric

Textiles treated with UV protection coatings show substantial improvements in shielding against ultraviolet (UV) radiation. These coatings absorb and reflect UVR, reducing transmission through the fabric, as shown in **Figure 12**. When exposed to sunlight, they scatter UV radiation, effectively protecting both the textile and the wearer from potential harm. This enhancement is often measured by the Ultraviolet Protection Factor (UPF), with higher UPF values indicating more reliable and robust protection. Such properties make UV-protective textiles especially suitable for outdoor and protective wear, as they help prevent both material degradation and UV-related skin damage. (46)

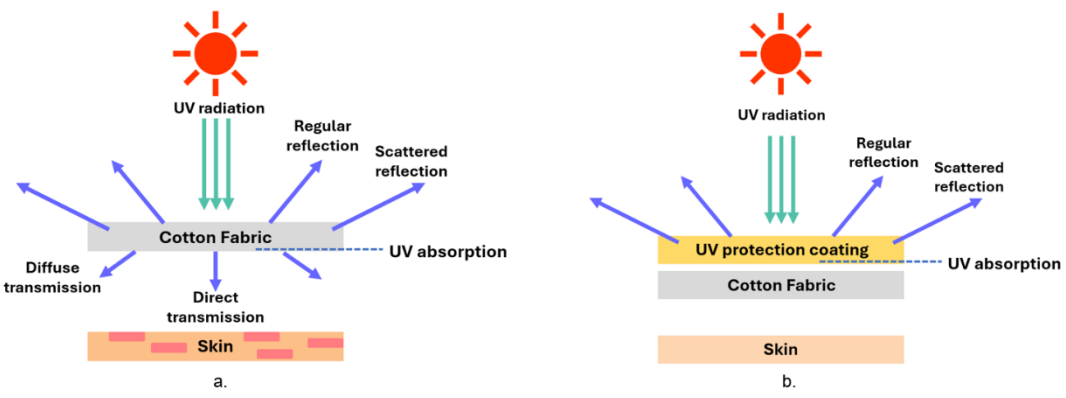

Figure 12 Diagram of UV radiation effects in unprotected (a) and protected (b) conditions

Ultraviolet radiation (UVR), which makes up almost 6% of the sun's total radiation, can also be produced from heated objects or electric arcs passing through gas. UVR has energy in the range of 3-124 eV and wavelengths between 100 and 400 nm. The discovery of UVR was made after evidence of chemical changes produced by them in matter. (5)

Ultraviolet protection factor (UPF) is the ratio of the average effective UVR irradiance calculated for unprotected skin to the average effective UVR irradiance

calculated for skin protected by AATCC (American Association of Textiles Chemists and Colorists) test method 183 (2014). The UPF is calculated according to the Eq. (2.6.1)

$$UPF = \frac{\sum_{280}^{400} E_\lambda S_\lambda \Delta_\lambda}{\sum_{280}^{400} E_\lambda S_\lambda T_\lambda \Delta_\lambda} \qquad (2.6.1)$$

Where:

E_λ = relative erythemal spectral effectiveness,

S_λ = solar spectral irradiance in $W.m^{-2}$. Nm^{-1}

T_λ = spectral transmittance of the item

Δ_λ = wavelength step in nm

λ = wavelength in nm

UVR: solar ultraviolet radiation in the range of 280 to 400 nm. (47)

UVA — solar ultraviolet radiation in the range of 315 to 400 nm.

UVB — solar ultraviolet radiation in the range of 280 to 315 nm.

Table 7 Ultraviolet protective factor rating according to ASTM D 6603 (47)

UPF Range	UVR protection category	Effective UVR transmission, %
15 to 24	Good protection	6.7 to 4.2
25 to 39	Very good protection	4.1 to 2.6
40 to 50, 50+	Excellent protection	$\leq$ 2 . 5

2.8 Anti-bacterial activity

The antibacterial mechanism of antibacterial coatings is predominantly attributed to the generation of reactive oxygen species (ROS), such as superoxide (O_2^-) and hydroxyl radicals (OH^-), upon activation by UV or natural light, as shown in **Figure 13**. These ROS are produced through the excitation of electrons within the coating material, which exhibits photocatalytic properties. The ROS generated acts directly on bacterial cells, disrupting essential cellular components, including DNA, proteins, and lipids in the cell membrane. This induces significant oxidative stress, ultimately compromising the integrity of the cell wall and leading to bacterial cell death, as shown in **Figure 14** (32)

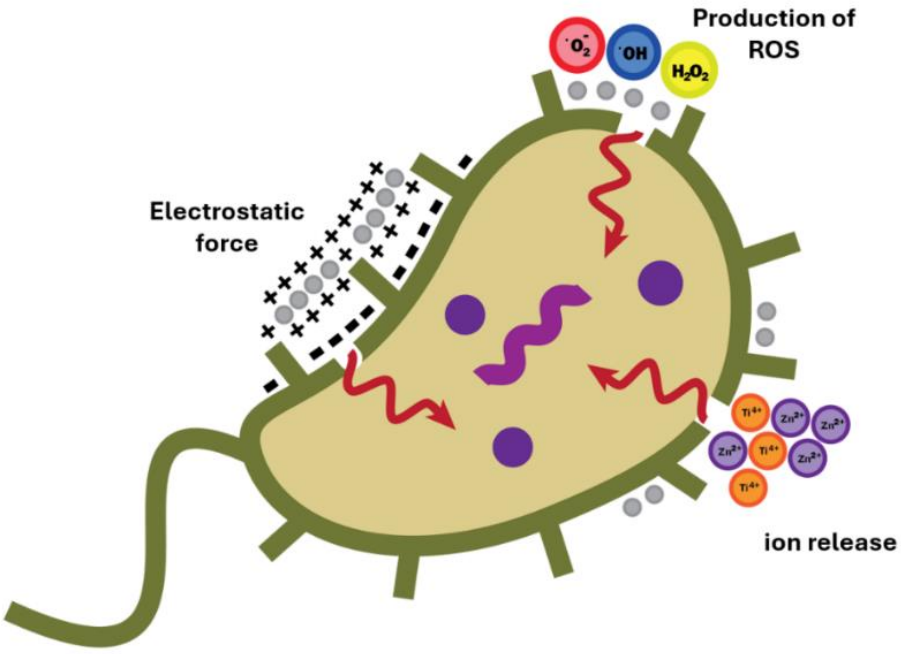

Figure 13 Hypothesized antibacterial mechanism of TiO_2-ZnO materials through ROS production and bacterial membrane disruption.

Antimicrobial textiles are fabrics treated with chemicals or natural compounds designed to kill or inhibit the growth of microorganisms. These textiles can be classified based on their effectiveness against different types of microbes, such as antibacterial, antifungal, or antiviral properties. Some antimicrobial textiles are versatile and able to target multiple types of microbes simultaneously, enhancing their efficacy in infection prevention.

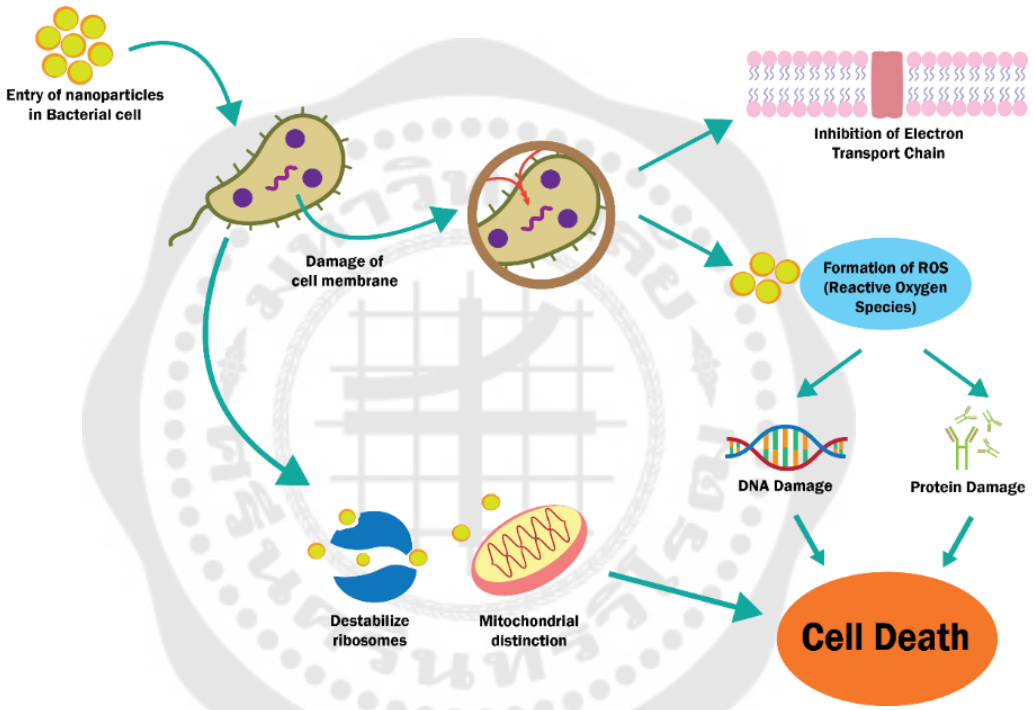

Figure 14 Antibacterial mechanism of ROS generation leading to bacterial cell death

The chemicals used in antimicrobial textiles generally act as broad-spectrum antimicrobial agents, capable of targeting a wide range of microbes. Such textiles are in high demand in public areas, including hotels, restaurants, and public transport, where the risk of infection from contaminated surfaces (e.g., towels, curtains, and carpets) is a concern. Additionally, odor control is a crucial area of research, as textiles can often harbor odor-causing microorganisms.

Continuous laundering of clothes is the most effective way to reduce the microbial load from textiles. However, this is not always possible in settings like

hospitals, where there are continuous shifts. Developing antimicrobial textiles is a promising solution to reduce the risk of microbial infection from contaminated textiles, especially in settings like hospitals and sewage treatment plants, where there is a high risk of infection. (48)

AATCC 100: 2019 – Test Method for Antibacterial Finishes on Textile Materials

- Report bacterial counts as the number of bacteria per sample (swatch in a jar), not as the number of bacteria per mL of neutralizing solution. Report "0" counts at 10^0 dilutions as "less than 100".

- Calculate the percent reduction of bacteria by the specimen treatments by one of the following formulas (2.7.1) :

$$100 (B - A) / B = R \qquad (2.7.1)$$

Where:

R = % reduction

A = the number of bacteria recovered from the inoculated treated test specimen swatches in the jar incubated over the desired contact period

B = the number of bacteria recovered from inoculated treated test specimen swatches in the jar immediately after inoculation (at "0" contact time)

2.9 Literature review

Extensive research has been conducted in recent years on the development of superhydrophobic textiles. These textiles, made by combining nanoparticles of materials such as ZnO, TiO_2, and SiO_2, can repel water. One method for achieving superior UV protection in textiles is applying TiO_2 nanoparticles to cotton fabric. This deposition process enhances the fabric's ability to block the sun's damaging UVR. ZnO and TiO_2 nanoparticles are commonly used in textiles for UV protection due to their capacity to reflect, scatter, or absorb harmful UVR. (2)

According to a 2004 study by Yang et al., the wavelength of light at which nano-TiO_2 begins to absorb UV radiation is known as its absorption edge. The blue shift of the absorption edge indicates that shorter wavelengths specifically those in the blue region of the electromagnetic spectrum are where nano-TiO_2 absorbs UV energy. This blue shift is detrimental to solar UV protection because it reduces the absorption of UVA radiation, which is harmful to the skin. While TiO_2 binds well to textiles, its absorption edge's blue shift diminishes UVA absorption, limiting its effectiveness as a solar UV protector. (49) Additionally, the researchers found that the treatment was highly effective against UVB radiation, known for causing sunburn and skin damage. The wavelength range of UVB light is 290–315 nm, and the researchers made note of this characteristic. (4) ZnO demonstrates excellent chemical stability when exposed to UV radiation and has high efficiency in blocking both UV-A and UV-B radiation. In 2013, Yazdanshenas and Mohammad Shateri coated cotton fabric with ZnO nanoparticles, confirming that the resulting fabric exhibited outstanding UV-blocking capabilities, particularly in the UVB range (280–315 nm). Even after undergoing five washing cycles, the ZnO-coated fabric maintained exceptional durability in terms of both antibacterial activity and UV protection. (50) In 2022, Nautiyal et al. investigated the production of cotton textiles containing ZnO-TiO_2 hybrid nanocrystals. These textiles demonstrated strong washing endurance, antibacterial effectiveness, and excellent UV protection. Combining ZnO and TiO_2 showed enhanced photocatalytic capabilities in hybrid nanocrystals (NCs). Recognizing the limitations of traditional pad-dry-cure methods for functionalizing

textiles, the authors proposed in situ synthesis of NCs on cotton fabric as a solution. The goal of this suggested technique is to create a wash-durable, multipurpose cotton fabric that maintains comfort levels while improving functional efficiency. The results demonstrated an impressive UV protection factor of up to 54, showcasing the material's highly effective UV-blocking capabilities. The materials exhibited potent antibacterial qualities, with a 100% bactericidal effectiveness against both S. aureus and E. coli. Remarkably, even after undergoing 30 thorough washing cycles, the resulting fabric maintained its antibacterial and anti-UV-R effectiveness. This durability makes them suitable for a variety of applications in the textile industry. (51)

Recently, in 2022, Priyanka et al. discussed the use of a one-pot precipitation approach to synthesize and characterize multifunctional biocidal nanocomposites consisting of ZnO, TiO_2, and GO. When GO sheets are adorned or replaced with inorganic nanoparticles like ZnO and TiO_2, they exhibit superior capabilities in inhibiting bacterial cell growth and show high rates of inhibition against E. coli. With their broad bandgaps, ZnO and TiO_2 nanoparticles display antibacterial and anticancer properties when exposed to UV or visible light. The combined action of ZnO and TiO_2 nanoparticles may enhance photocatalytic and therapeutic activity by increasing the dissociation efficiency of photo-excited charge carriers. These effects are amplified when ZnO and TiO_2 nanoparticles create a heterojunction structure. (43)

This enhancement in performance can be attributed to the synergistic effects of combining different materials. The presence of ZnO and TiO_2 nanomaterials on the GO sheets can enhance their properties, such as biocidal activity or other functionalities. When combined with ZnO and TiO_2 nanomaterials, GO can result in improved properties such as better stability, enhanced electrical conductivity, and increased antibacterial or anticancer activity. Moreover, this combination can be more cost-effective than using individual materials, as it produces better results without requiring large amounts of expensive substances.

CHAPTER 3
MATERIALS AND METHODS

This thesis is divided into two parts as follows:

(3.1) Study the effect of the number of coating layers on the hydrophobicity of TNPsGZ-coated cotton fabrics.

(3.2) Study the impact of TG: ZnO ratios on hydrophobicity, UV protection, and antibacterial activity of TNPsGZ-coated cotton fabrics.

3.1 Study the effect of the number of coating layers on the hydrophobicity of TNPsGZ-coated cotton fabrics.

3.1.1 Chemical reactants, materials and types of equipment

3.1.1.1 Chemical reactants

- Titanium dioxide Commercial Degussa P25 (TiO_2)
- Single-layer Graphene Oxide (GO)
- Ethanol 98.5%, Chemipan, Thailand
- Isopropanol (IPA), Chemipan, Thailand
- Zinc oxide (ZnO), Chemipan, Thailand
- Polyvinylpyrrolidone (PVP), Chemipan Thailand
- Deionized water

3.1.1.2 Materials and Equipment

- 100% Cotton fabric, Bulliontex Co., Ltd.
- Beaker (50, 250, 800 mL)
- Ultrasonic bath, Derui®
- Dropper
- Hot plate stirrer
- Magnetic bar
- Hot air oven

3.1.2 Synthesis of titanium dioxide/graphene oxide composite

0.06 g GO was dispersed into 200 mL ethanol (98.5%) under ultrasonic-assisted conditions for 45 min to obtain the homogeneous solution. After that, 1.94 g TiO_2 was slowly added to the GO suspension under vigorous stirring conditions at 80°C for 2 h. GO and TiO_2NPs were sonicated for 3 h to obtain TG suspension (TiO_2/GO)(52). As shown in **Figure 15**.

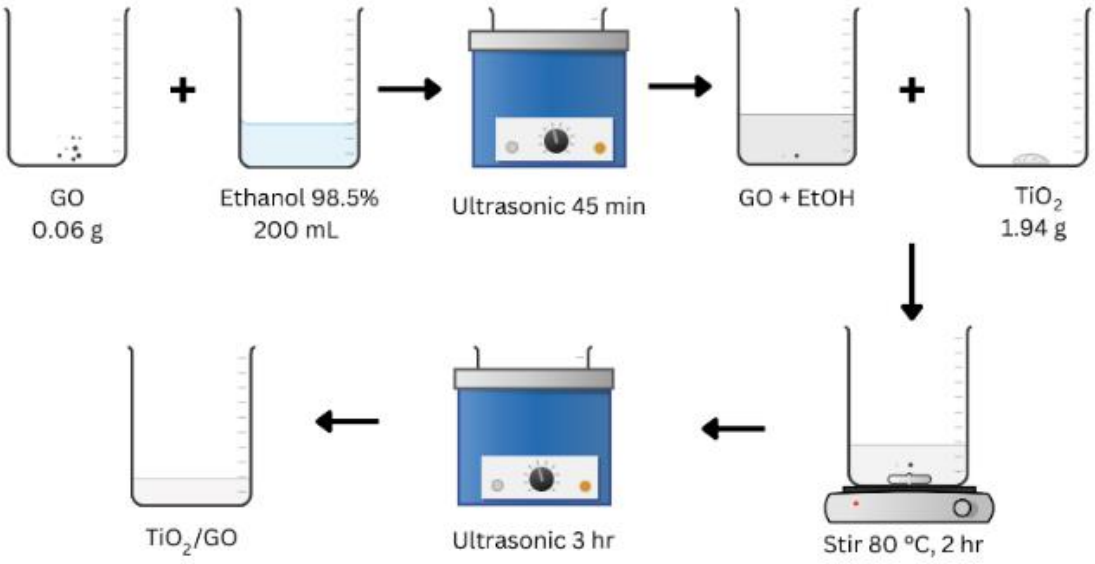

Figure 15 Schematic representation of the synthesis process for TiO_2/GO composites via ultrasonic-assisted methods.

3.1.3 Synthesis of TNPsGZ composites.

3 g of ZnO were dispersed into a variable TG suspension, and 40 mL of isopropanol under ultrasonic-assisted conditions for 1.30 hours to obtain a homogeneous solution. The suspension was then dried at room temperature and ground into a powder. Polyvinylpyrrolidone (PVP) was slowly added to the 200mL DI water. After that, 2 g of TNPsGZ composites powder added to the solution under ultrasonic-assisted conditions for 1.30 h and stirring at 75°C to obtain TNPsGZ composites solution. As shown in **Figure 16**.

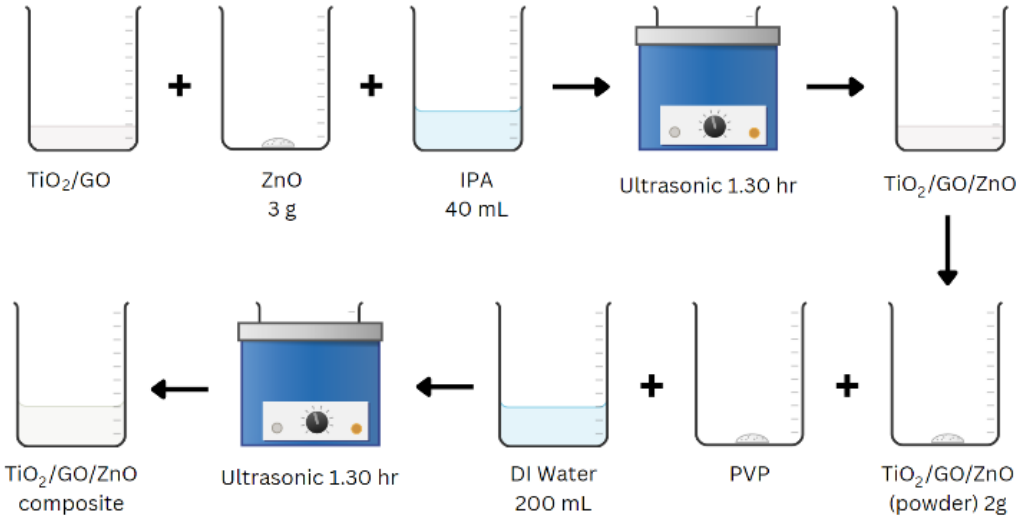

Figure 16 Illustration of the synthesis process for TNPsGZ composites, showing the integration of TiO_2/GO and ZnO particles into a homogeneous composite using ultrasonic-assisted methods.

3.1.4 Coating of cotton fabric

Fabrics were coated with TNPsGZ composites at 75°C for 30 min. After that, the specimen was dried at 120°C for 30 min. All specimen was cured for 30 min at a consistent temperature of 130°C. To increase the number of layers, the coating process was repeated under the same conditions, applying subsequent layers of TNPsGZ composites to the fabric. After each application, the specimen was subjected to the same drying procedures to ensure uniform adhesion and optimal composite integration. As shown in **Figure 17**.

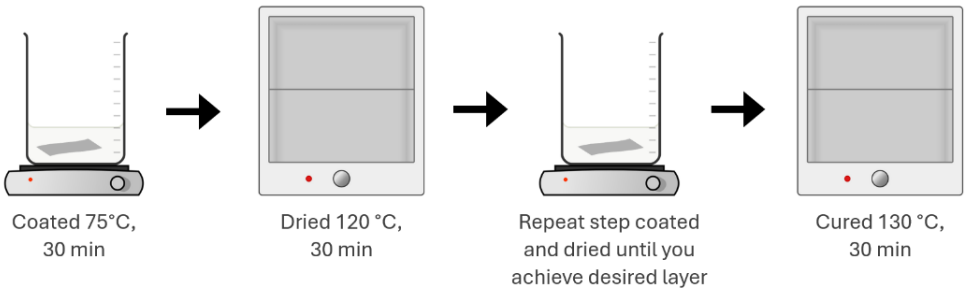

Figure 17 Illustration of the coating process where TNPsGZ composites are applied layer by layer onto cotton fabric, with each layer undergoing drying and curing until the desired number of layers is achieved.

3.1.5 Washing

This step was applied to the AATCC (American Association of Textiles Chemists and Colorists) test method 61 (2010).

3.1.6 Characterization of composites

3.1.6.1 Fourier transform infrared (FTIR)

The composite powder samples were prepared in potassium bromide (KBr) pellets and recorded using a Bruker FT-IR Alpha spectrometer in the frequency range of 4000-500 cm^{-1}.

3.1.7 Characterization of cotton fabric

3.1.7.1 Fourier transform infrared (FTIR)

The cotton fabric samples were deposited on a diamond crystal. Using a Bruker FT-IR Alpha spectrometer, the ATR spectra were recorded in the frequency range of 4000-400 cm^{-1}.

3.1.7.2 Scanning electron microscope (SEM)

The morphology and chemical composition of the deposited layers on the cotton fabric were affixed to the specimen stub using double-sided adhesive tape. Subsequently, they underwent gold coating via a sputter coating process and were analyzed using a scanning electron microscope (SEM) (JEOL JSM-6480LV).

3.1.8 Properties of cotton fabric

3.1.8.1 Hydrophobic properties

Samples were analyzed by measuring the contact angle of the cotton fabric coated with composites and comparing it to the cotton fabric coated with the composite using a contact angle system (OCA). A 5 µL water droplet was deposited on the surface, and images were captured at 10-second intervals.

3.2 Study the impact of TG: ZnO ratios on hydrophobicity, UV protection, and antibacterial activity of TNPsGZ-coated cotton fabrics.

3.2.1 Preparation of TNPsGZ composites

3.2.1.1 Synthesis of titanium dioxide/graphene oxide composite

0.06 g GO was dispersed into 200 mL ethanol (98.5%) under ultrasonic-assisted conditions for 45 min to obtain the homogeneous solution. After that, 1.94 g TiO_2 was slowly added to the GO suspension under vigorous stirring conditions at 80°C for 2 h. GO, and TiO_2NPs were sonicated for 3 h to obtain TG suspension (TiO_2/GO) (52). As shown in **Figure 18**.

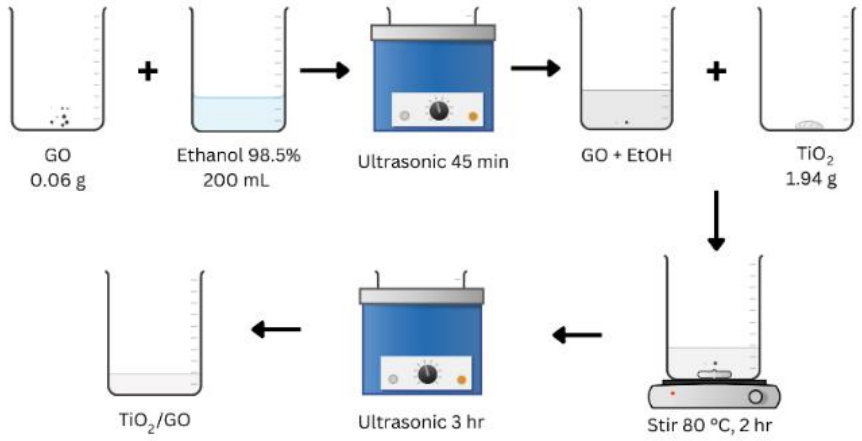

Figure 18 Illustration of the synthesis process for TiO_2/GO composites using ultrasonic-assisted techniques.

3.2.1.2 Synthesis of TNPsGZ composites.

ZnO is distributed in variable proportions based on the TG: ZnO ratios (1:1, 1:3, 1:5, 1:7). To create a homogeneous solution, ZnO was dispersed into a 10 mL TG suspension and 40 mL of isopropanol for 3 hours with ultrasonic assistance. Following this, the suspension was allowed to dry at room temperature and then crushed into a powder, forming the TNPsGZ composite. A further step involved gradually adding 0.2 g of Polyvinylpyrrolidone (PVP) to 100 mL of DI water. The TNPsGZ composite solution was then created by adding 1 g of TNPsGZ composite powder to the mixture and stirring it for 1.30 hours at 75°C with ultrasonic assistance. As shown in **Figure 19**.

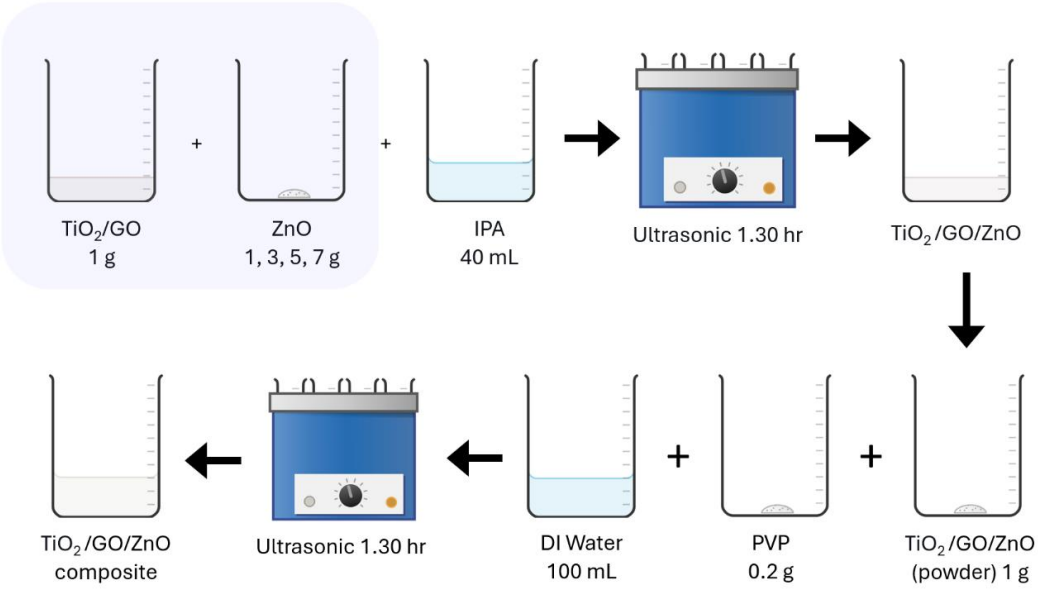

Figure 19 Step-by-step synthesis process of TNPsGZ composites, highlighting the incorporation of ZnO particles at varying TG: ZnO weight ratios (1:1, 1:3, 1:5, and 1:7) through ultrasonic-assisted methods.

3.2.2 Preparation of TiO_2/PVP and ZnO/PVP composite

3.2.2.1 Synthesis of TiO_2/PVP composite

This step involved the gradual addition of 0.2 g of Polyvinylpyrrolidone (PVP) into 100 mL of DI water. Subsequently, a TiO_2 composite solution was prepared by incorporating 1 g of TiO_2 powder into the mixture, followed by stirring for 1 hour and 30 minutes at 75°C with ultrasonic assistance, as shown in **Figure 20.**

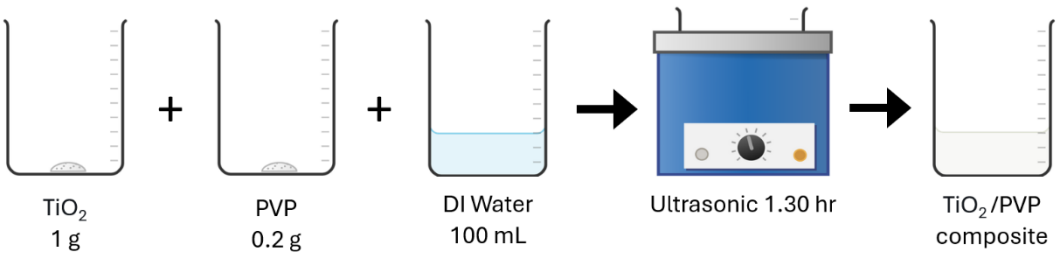

Figure 20 Preparation of TiO_2/PVP composite using ultrasonic assistance

3.2.2.2 Synthesis of ZnO/PVP composite

This step involved gradually dissolving 0.2 g of Polyvinylpyrrolidone (PVP) in 100 mL of DI water. A ZnO composite solution was then prepared by adding 1 g of ZnO powder into the mixture and stirring it for 1 hour and 30 minutes at 75°C with ultrasonic assistance, as shown in **Figure 21**.

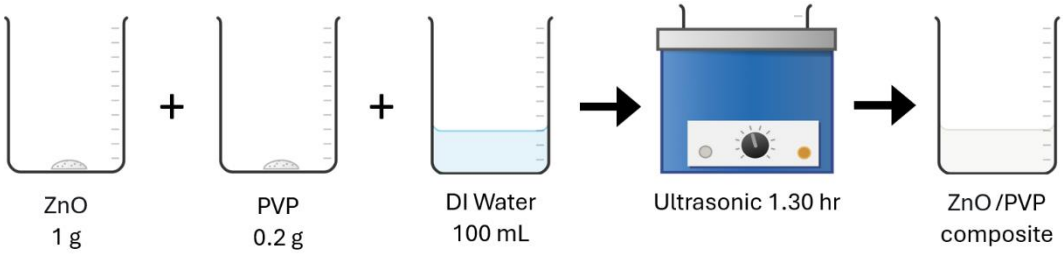

Figure 21 Preparation of ZnO/PVP composite using ultrasonic assistance

3.2.3 Coating of fabric

Fabrics were coated with TNPsGZ composites, TiO_2/PVP and ZnO/PVP at 75°C for 30 min. After that, the specimen was dried at 120°C for 30 min. All specimens were cured for 30 min at a consistent temperature of 130°C, as shown in **Figure 22**.

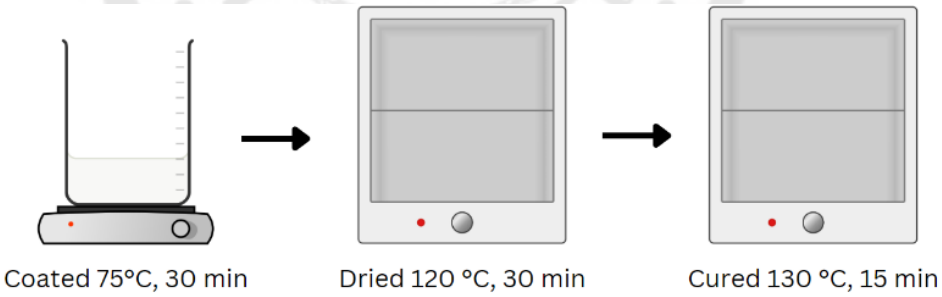

Figure 22 Diagram of the coating process for cotton fabric using the dip-dry-cure technique to apply composites.

3.2.3 Characterization of composites

3.2.3.1 Fourier transform infrared (FTIR)

The composite powder samples were prepared in potassium bromide (KBr) pellets and recorded using a Bruker FT-IR Alpha spectrometer in the frequency range of 4000-500 cm^{-1}.

3.2.3.2 Raman spectroscopy

The composite powder samples were recorded from 50 to 2500 cm^{-1} on PERKIN ELMER Spectrum GX.

3.2.3.3 X-ray Diffraction (XRD)

The crystalline structure and crystal phases of the as-prepared composite catalysts were determined by the X-ray powder diffractometer, and the refraction data were recorded for 2θ diffraction angle in the range of 10° –100°.

3.2.3.4 Field Emission Scanning Electron Microscope (FE-SEM)

The morphology and chemical composition of the composite were mounted on the specimen stub with double-sided adhesive tape. Afterward, the samples underwent platinum or gold coating via a sputter deposition process and were analyzed using a Field Emission Scanning Electron Microscope (FE-SEM).

3.2.4 Characterization of cotton fabric

3.2.4.1 Fourier transform infrared (FTIR)

The cotton fabric samples were deposited on a diamond crystal. Using a Bruker FT-IR Alpha spectrometer, the ATR spectra were recorded in the frequency range of 4000-400 cm^{-1}.

3.2.4.2 Scanning electron microscope (SEM)

The morphology and chemical composition of the deposited layers on the cotton fabric were affixed to the specimen stub using double-sided adhesive tape. Subsequently, they underwent gold coating via a sputter coating process and were analyzed using a scanning electron microscope (SEM) (JEOL JSM-6480LV).

3.2.5 Properties of cotton fabric

3.2.5.1 Hydrophobic properties

Samples were analyzed by measuring the contact angle of the cotton fabric coated with composites and comparing it to the cotton fabric coated with the composite using a contact angle system (OCA). A 5 µL water droplet was deposited on the surface, and images were captured at 10-second intervals.

3.2.5.2 UV-Vis spectrophotometer

Cotton fabric samples, sized 20x20 cm, were dry tested after the coating, drying, and curing processes were completed. The samples were submitted to the Thailand Textile Institute for evaluation of UV protection performance according to the AATCC-183(2014) test method using a UV-Vis spectrophotometer.

3.2.5.3 Antibacterial activity

The fabric material was tested utilizing the AATCC 100 test technique, employing both test and control samples that had not been treated with an antibacterial agent. By comparing the decrease in the viable count of bacteria on the treated sample with the untreated sample, antibacterial activity is ascertained. This process evaluates the antimicrobial test agent's bacteriostatic (inhibition of proliferation) and bactericidal (bacterium-killing) properties.

CHAPTER 4
RESULTS AND DISCUSSION

This chapter presents the experimental results and analysis of the properties of TNPsGZ composite coatings on fabric, organized into three main parts as follows:

(4.1) Characterization of TiO_2, GO, and ZnO Materials

(4.2) Effect of multiple coating layers on hydrophobic properties of TNPsGZ-coated fabrics

(4.3) Impact of TG: ZnO ratios on hydrophobicity, UV protection, and antibacterial activity of TNPsGZ-coated fabrics

4.1 Characterization of TiO_2, GO, and ZnO Materials

4.1.1 Characterization of Titanium Dioxide P25 (TiO_2)

The characterization of TiO_2 nanoparticles (Degussa P25) was performed to critically evaluate their structural, chemical, and morphological properties, which are essential for their integration into composite materials. The analysis employed Fourier Transform Infrared Spectroscopy (FTIR) and Raman Spectroscopy to elucidate functional groups and molecular vibrations, X-ray Diffraction (XRD) to identify crystalline phases and compute average crystallite size and Scanning Electron Microscopy (SEM) to investigate particle morphology and size distribution, thereby providing comprehensive insights into the material's characteristics.

4.1.1.1 Fourier transform infrared (FTIR)

The FTIR spectra of the titanium dioxide (Degussa P25) are shown in **Figure 23**. The Ti-O bending mode and deformative vibration of the Ti-OH stretching mode can be observed at 1626 cm^{-1} in the FTIR spectra of TiO_2 nanoparticles. Stretching vibrations of the hydroxyl group (-OH) can be seen at 3409 cm^{-1}, both symmetrically and asymmetrically. The band at 1626 cm^{-1} might result from water absorbed onto the surface of TiO_2. Consequently, the two detected peaks at 3409 and 1626 cm^{-1} are associated with hydroxyl groups and surface-adsorbed water (25,53), and the OH bands in the spectrum are a result of H_2O that has been chemically and physically adsorbed on the surface of nanoparticles (54).

The band at 1626 cm^{-1} is due to the bending mode of the H-O-H bond, which further confirms the presence of physically adsorbed water molecules on the nanoparticle surface. Additionally, the absorption peak at 1397 cm^{-1} is particularly noteworthy. This peak can be attributed to the stretching vibrations of the C=O bond, suggesting the presence of carbonate groups on the surface of the TiO_2 nanoparticles. (53)

According to reports, the strong absorption bands in the region from 1000 to 400 cm^{-1} are characteristic of Ti-O stretching and Ti-O-Ti bridging stretching modes. Specifically, the peak observed at around 778 cm^{-1} is assigned to the Ti-O stretching vibration, while the broadband spanning 450-650 cm^{-1} corresponds to the Ti-O-Ti bridging stretching vibrations.(55) These peaks indicate the presence of both anatase and rutile phases of TiO_2, supporting the Raman spectra and XRD findings.

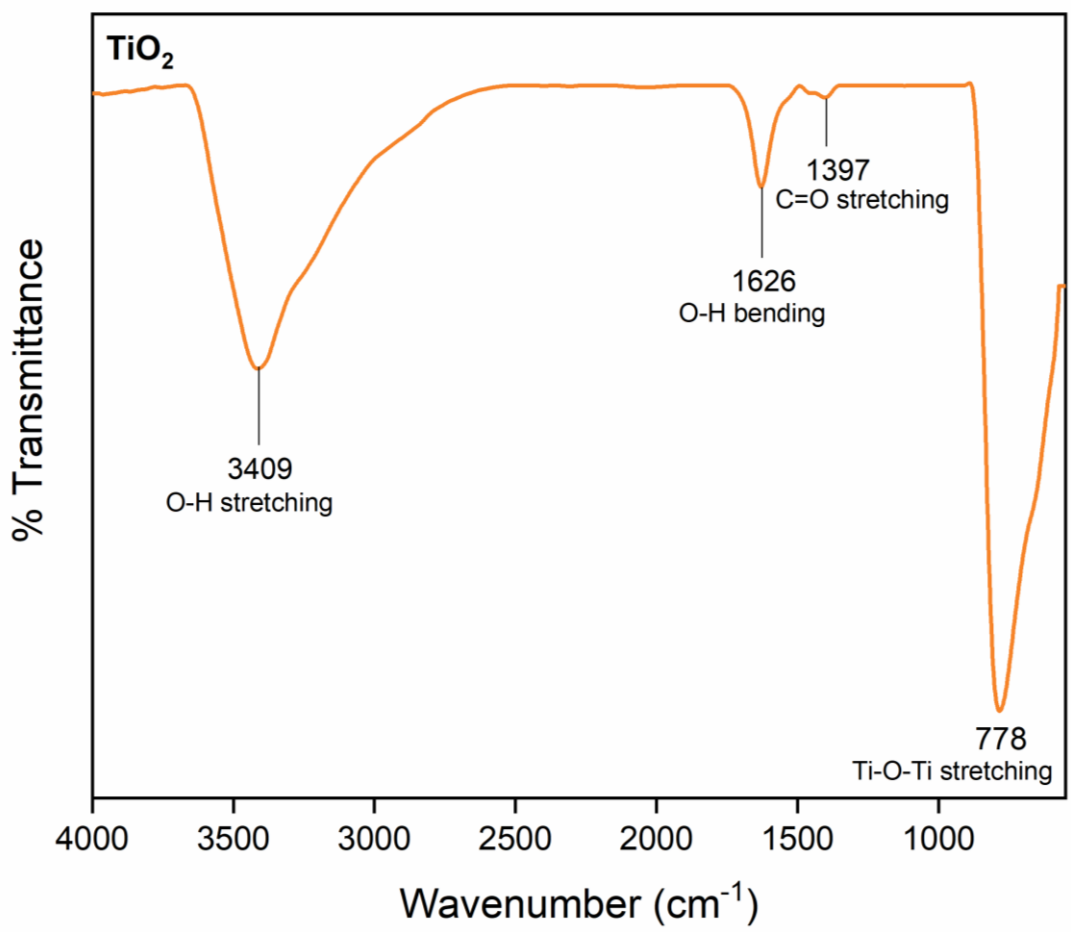

Figure 23 FTIR spectra of TiO_2

4.1.1.2 Raman Spectroscopy

The Raman spectra of TiO_2 as shown in **Figure 24**. TiO_2 exhibits Raman bands at 638, 515, 396, and 196 cm^{-1}, as well as a very sharp and intense peak at 143 cm^{-1}. The Raman-active modes can be assigned based on group-theoretical analysis for the anatase phase, which belongs to the space group $D4h^{19}$ and proposed site symmetries for the Ti and O atoms within the unit cell (D_{2d} for Ti; C_{2v} for O) as follows: A_{1g} (515 cm^{-1}), B_{1g} (638 cm^{-1} and 396 cm^{-1}), E_g (143 cm^{-1} and 196 cm^{-1}). These Raman-active modes provide valuable information about the vibrational properties and symmetry of the TiO_2 crystal structure. The strong and sharp peak at 143 cm^{-1} (E_g mode) is particularly notable and is commonly used as a fingerprint for the anatase phase of TiO_2. This peak and other characteristic bands confirm the successful synthesis of anatase TiO_2 nanoparticles. Raman spectroscopy also detects phase transitions and the presence of mixed phases.

The intensity and sharpness of the Raman peak at 196 cm^{-1}, corresponding to the E_g mode, a lattice vibration characteristic of rutile TiO_2, along with other peaks associated with anatase, indicate high crystallinity and minimal structural defects in the nanoparticles. The coexistence of anatase and rutile phases can enhance the photocatalytic properties of TiO_2, as the mixed-phase composition is known to facilitate electron-hole separation and improve overall photocatalytic efficiency. The absence of peaks corresponding to the rutile phase (typically observed at 447 cm^{-1} for the E_g mode) indicates that the synthesized TiO_2 nanoparticles predominantly consist of the anatase phase. (53,56)

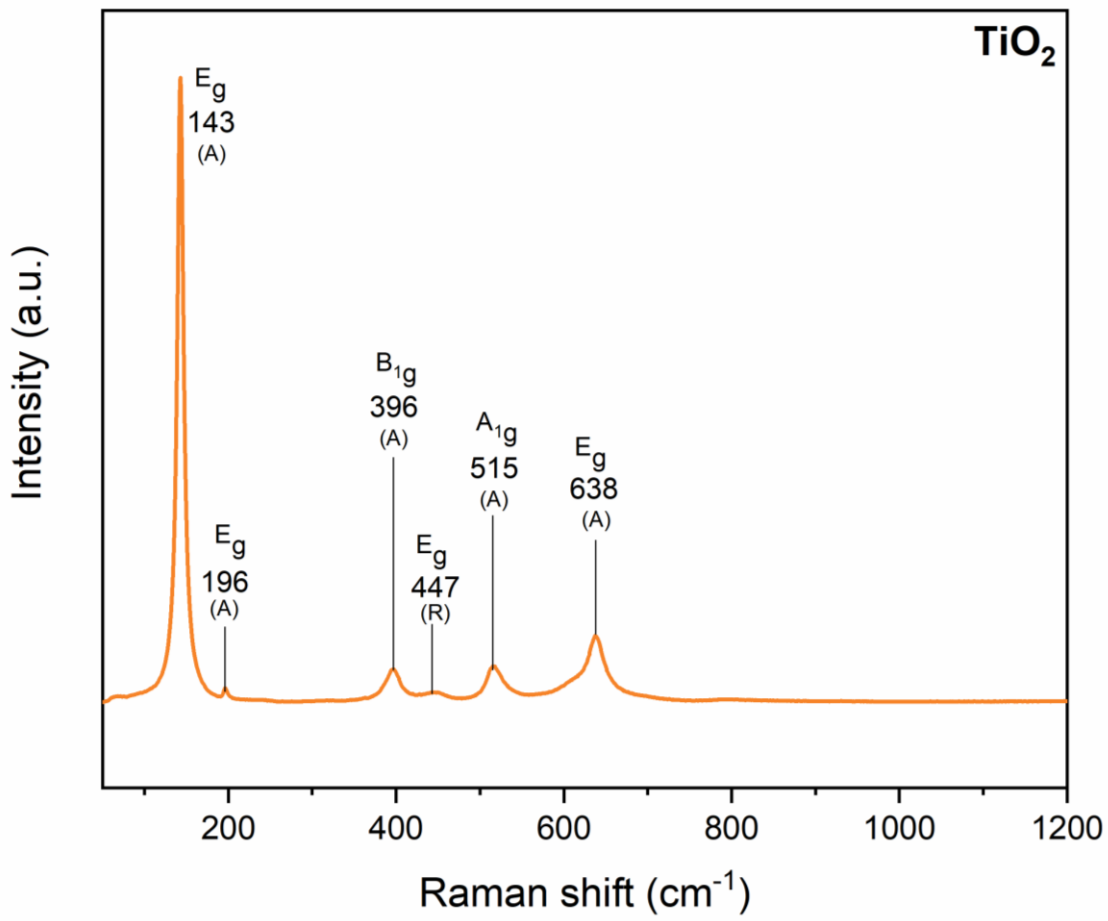

Figure 24 Raman spectra of TiO_2

4.1.1.3 X-ray Diffraction (XRD)

The powder X-ray diffraction pattern of pure TiO_2 nanoparticles showing the crystal family of planes for each diffraction peak is depicted in **Figure 25**. Each of them could be identified as one of the characteristic TiO_2 peaks, which is well correlated with the anatase phase (JCPDS-ICDD card: 21-1272) and rutile phase (JCPDS-ICDD card: 21-1276). The intense diffraction peaks appearing at about 2θ of 25.29°, 27.42°, 36.98°, 38.54°, 48.03°, 55.06°, and 62.67° corresponding with those from (101), (110), (103), (004), (112), (200), (211), and (204) orientations, respectively. These peaks confirm the presence of both anatase and rutile phases in the synthesized TiO_2 nanoparticles.

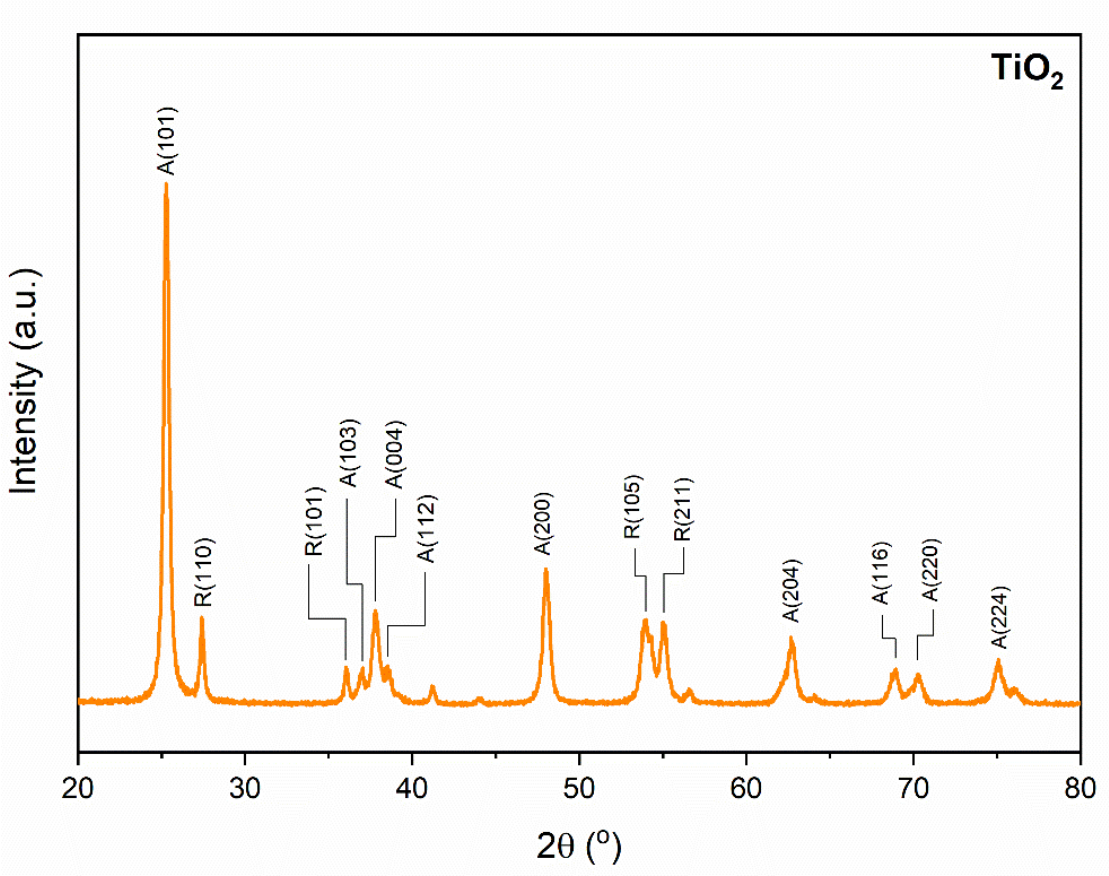

Figure 25 XRD patterns of TiO_2 identifying anatase and rutile crystalline structures.

The crystallite size of the TiO_2 nanoparticles, averaged at 17.55 nm, was estimated using the Debye–Scherrer formula as shown in **Table 8**. The anatase phase,

characterized by the prominent peak at 25.29° (101), and the rutile phase, indicated by the peaks at 27.42° (110) and 36.07° (101), are both well-known for their unique properties. The XRD results are further corroborated by the FTIR and Raman spectroscopy analyses. The absence of significant peaks corresponding to the rutile phase in the Raman spectra suggests that the anatase phase is predominant in the synthesized nanoparticles, aligning with the XRD findings. (57)

I use the Debye-Scherrer relation and the full width at half maximum (FWHM) of the (h k l) peaks, the average crystallite size has been estimated from 2θ. (26)

Table 8 Calculated crystallite sizes of the TiO_2 nanoparticles (Mean: 17.55 nm) by the Debye–Scherrer method.

2θ	FWHM	Cos θ	Size (nm)
25.29	0.44	0.98	19.26
27.42	0.34	0.97	25.28
36.07	0.32	0.95	27.50
36.98	0.57	0.95	15.28
37.81	0.48	0.95	18.26
38.54	0.64	0.94	13.71
48.03	0.52	0.91	17.55
54.04	0.79	0.89	11.82
55.06	0.54	0.89	17.33
56.57	0.41	0.85	22.89
62.67	0.74	0.88	13.12
68.87	0.62	0.82	16.16
70.22	0.74	0.82	13.78
75.10	0.76	0.79	13.70
Crystalline size average			**17.55**

To calculate the Anatase/Rutile ratio using the Spurr and Myers equation from the given intensity data (24,53):

Anatase intensity (I_A) = 2224

Rutile intensity (I_R) = 360

The Spurr and Myers equation is:

$$\frac{W_R}{W_A} = 1.22\left(\frac{I_R}{I_A}\right) - 0.028$$

$$= 1.22\left(\frac{360}{2224}\right) - 0.028$$

$$= 1.22\,(0.1619) - 0.028$$

$$= 0.1971 - 0.028$$

$$= 0.1691$$

So, the ratio of Rutile to Anatase is 0.1691 to 1.

Next, calculate the percentages of Anatase (W_A) and Rutile (W_R) by assuming $W_A+W_R=1$:

$$WR = 0.1691WA$$

$$WA + 0.1691WA = 1$$

$$1.1691WA = 1$$

$$WA = \frac{1}{1.1691}$$

$$WA = 0.8554$$

Therefore:

Percentage of Anatase = $WA\times100 \approx 85.54\%$

Percentage of Rutile = $(1- WA)\times100 \approx 14.46\%$

In conclusion, the sample contains approximately 85.54% Anatase and 14.46% Rutile.

4.1.1.4 Field Emission Scanning Electron Microscope (FE-SEM)

The pristine TiO_2's morphologies, size and chemical composition were determined using FE-SEM and energy-dispersive X-ray spectroscopy (EDX). The FE-SEM image (**Figure 26**) and the particle's size distribution histogram (**Figure 28**) show the TiO_2 nanoparticles have a spherical form with an average nanoparticle size of 19.26 nm, which agrees with the XRD result (**Table 8**). Notably, this size is close to the 17.55 nm value obtained in Table 8, further supporting the consistency between measurements. The EDX spectrum (**Figure 27**) demonstrates the presence of oxygen (O)(51.27 wt.%,25.5 at.%), titanium (Ti) (43.47 wt.%, 19.96 at.%), and carbon (C) (5.25 wt.%, 9.62 at.%).

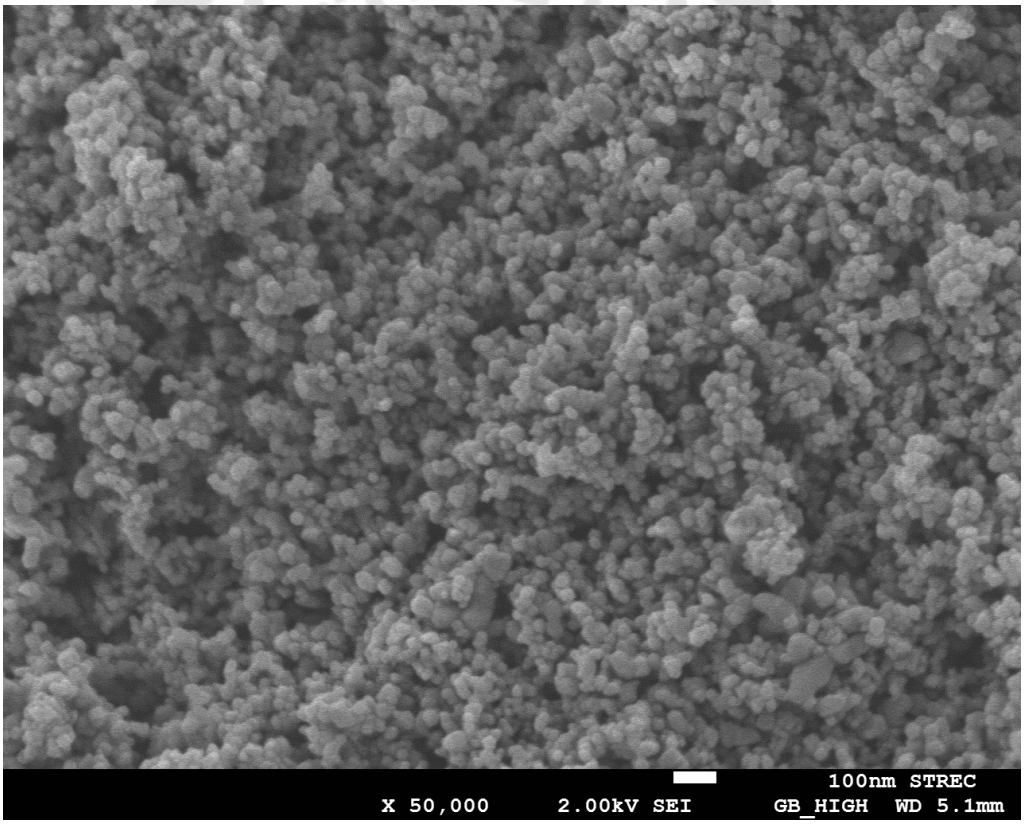

Figure 26 FE-SEM micrograph of TiO_2, scale bar 100 nm

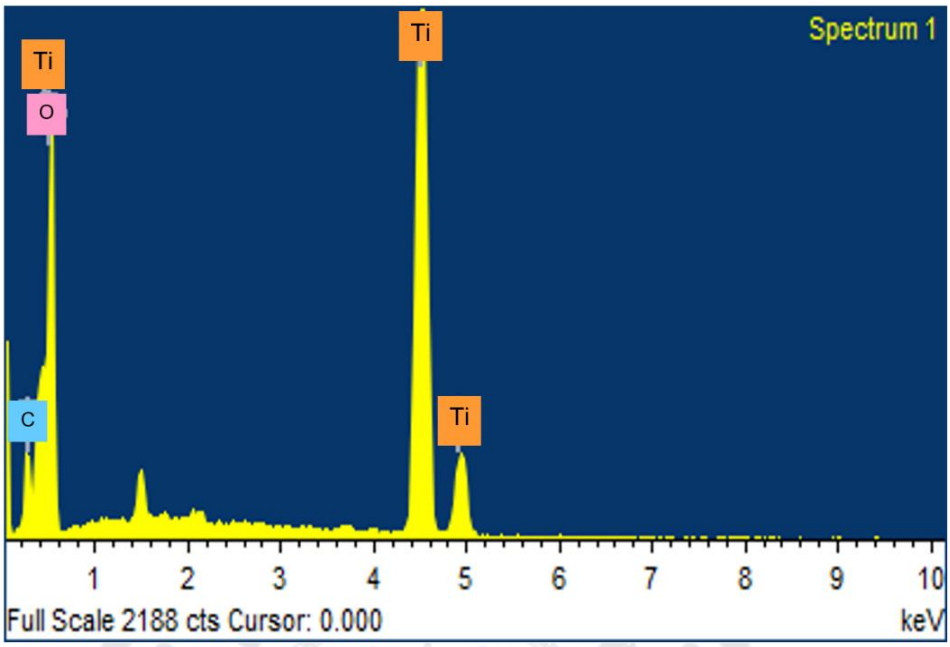

Figure 27 EDX spectrum of TiO_2

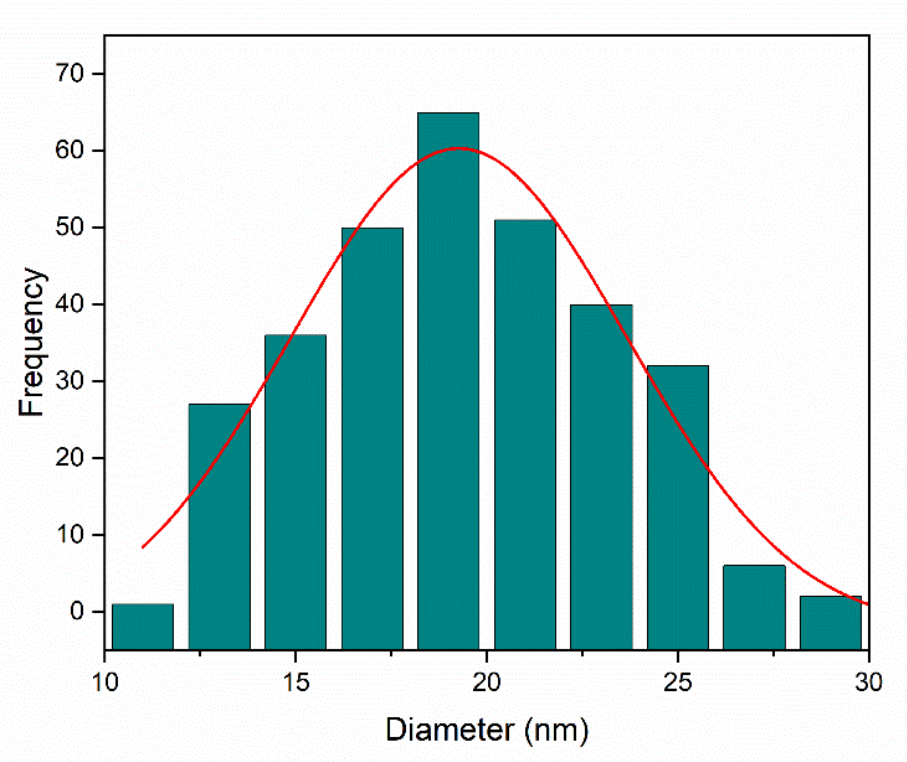

Figure 28 The particle size distribution histogram determined from the FE-SEM images.

4.1.2 Characterization of Graphene Oxide (GO)

The characterization of graphene oxide (GO) was conducted to confirm its chemical structure and evaluate its functional properties. Analytical techniques, including Fourier Transform Infrared Spectroscopy (FTIR), Raman Spectroscopy, X-ray Diffraction (XRD), Scanning Electron Microscopy (SEM), and Energy Dispersive X-ray Spectroscopy (EDS), were employed to investigate the material's functional groups, structural modifications, morphology, and elemental composition, providing comprehensive insights into its chemical and structural characteristics.

4.1.2.1 Fourier transform infrared (FTIR)

The FTIR spectrum of graphene oxide (GO) is shown in **Figure 29**. The GO spectrum reveals a diverse range of vibrational bands indicative of the following: The high-frequency zone peak at 3354 cm^{-1} is identified as O-H stretching, indicating the presence of hydroxyl groups. The carboxyl group (C=O stretching) was assigned to the band seen at 1719 cm^{-1}, suggesting the presence of carboxylic acid functional groups on the GO surface. The carbon double bond (C=C stretching) is responsible for the strident peak detected at 1621 cm^{-1}, characteristic of the sp^2 hybridized carbon present in the graphene structure. The C–the peak represents the O stretching bond at 1367 cm^{-1}, associated with epoxy or alkoxy groups. The C–O–H vibration mode is shown by the peak at 1057 cm^{-1}, indicating the presence of hydroxyl groups. (37,58)

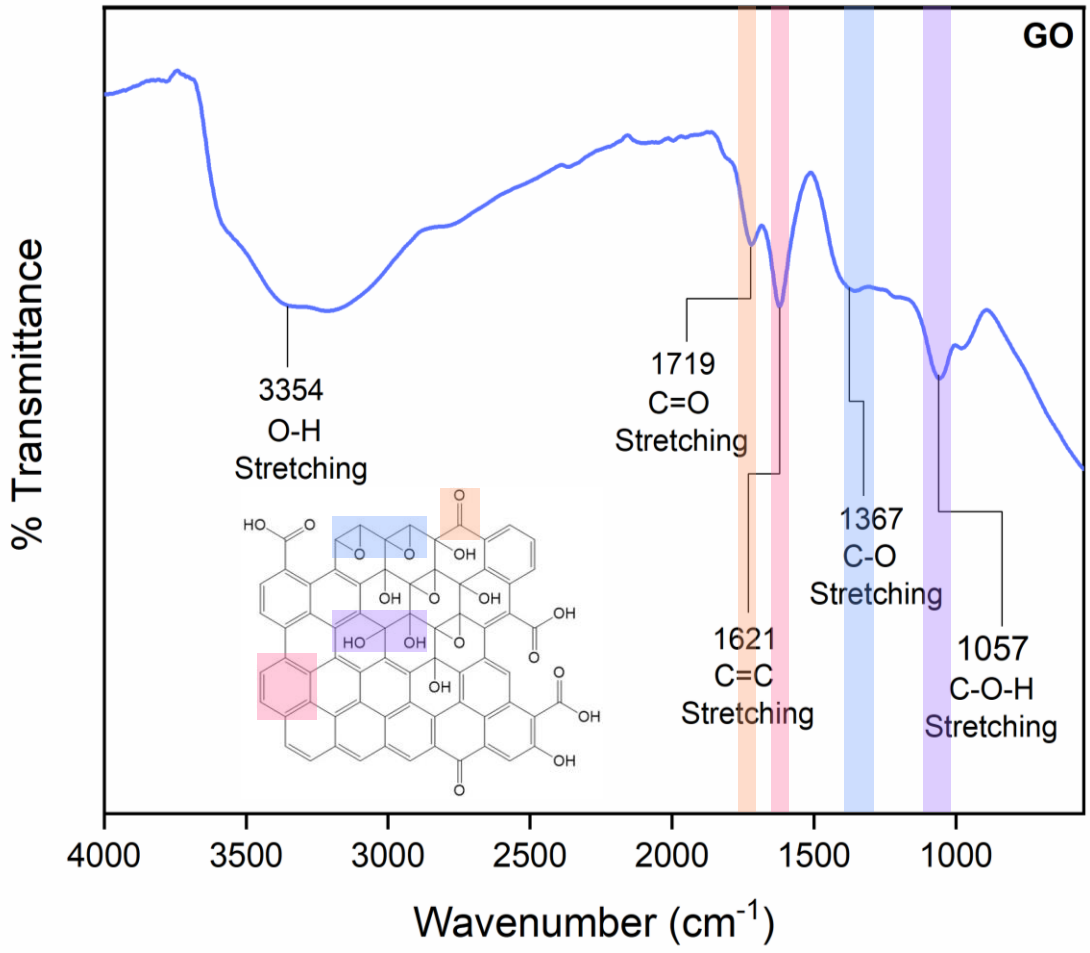

Figure 29 FTIR spectra of graphene oxide

4.1.2.2 Raman Spectroscopy

The Raman spectrum of graphene oxide (GO) is shown in **Figure 30**. The Raman spectrum displays two distinct peaks in the 1000 - 2000 cm^{-1} region, corresponding to the D and G bands. The GO exhibits a prominent G band mode, observed between 1500 and 1700 cm^{-1}, and a D band mode, appearing between 1250 and 1400 cm^{-1}. In contrast, the G vibration band from the first-order E_2g phonon scattering by sp_2 carbon was seen at 1584 cm^{-1}. Moreover, the stretching C-C bond represented in all sp_2 carbon systems also contributed to the G vibration band. As a result of structural imperfections introduced during the oxidation process, GO typically displays a prominent D band in its Raman spectrum. The presence of oxygen-containing functional groups and sp_3 carbon atoms within the structure can cause the G band to shift to higher wavenumbers.

A broad 2D band and 3s band were seen at 2680 and 2929 cm^{-1}. Because the 2D band is sensitive to the stacking of graphene layers, it determines the number of layers (monolayer, double layer, or multilayer). Since monolayer graphene is typically detected around 2679 cm^{-1} from the spectra, the placement of the 2D band thus indicates that the generated GO was monolayer. Hence, direct evidence of the degree of functionalization is provided by the intensity ratio of I_D/I_G. Conversely, the GO I_D/I_G ratio = 0.80. This ratio reflects a significant presence of defects and functional groups, characteristic of GO, due to oxidation. (37,59–61)

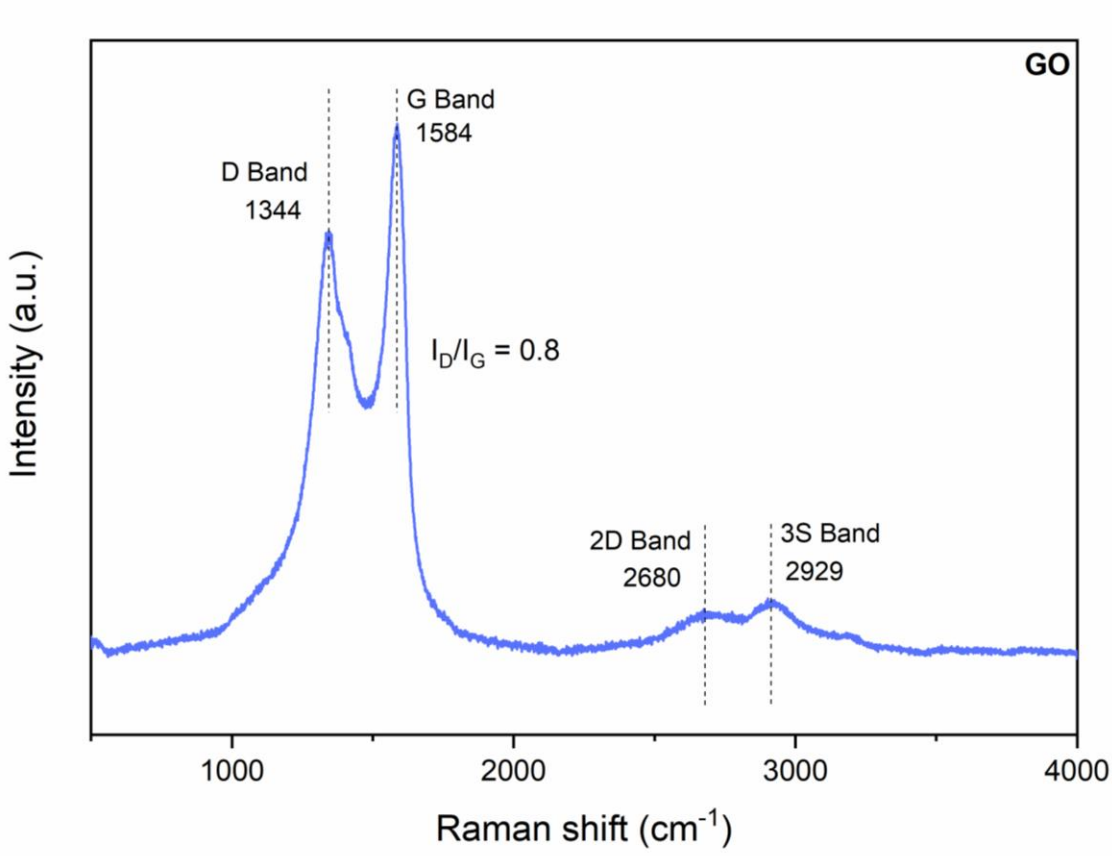

Figure 30 Raman spectra of GO

4.1.2.3 X-ray Diffraction (XRD)

XRD pattern of graphene oxide (GO) as shown in **Figure 31**. The sharp diffraction peak at 2θ of 10.87°and 42.62° correspond to the reflections of (001) and (100), respectively. The full width at half maximum (FWHM) values obtained from the XRD instrument for GO were 12.02. The interplanar spacing d001 of GO was calculated to be 0.813 nm, suggesting that the graphene layers are separated by oxygen-containing functional groups. (37,62)

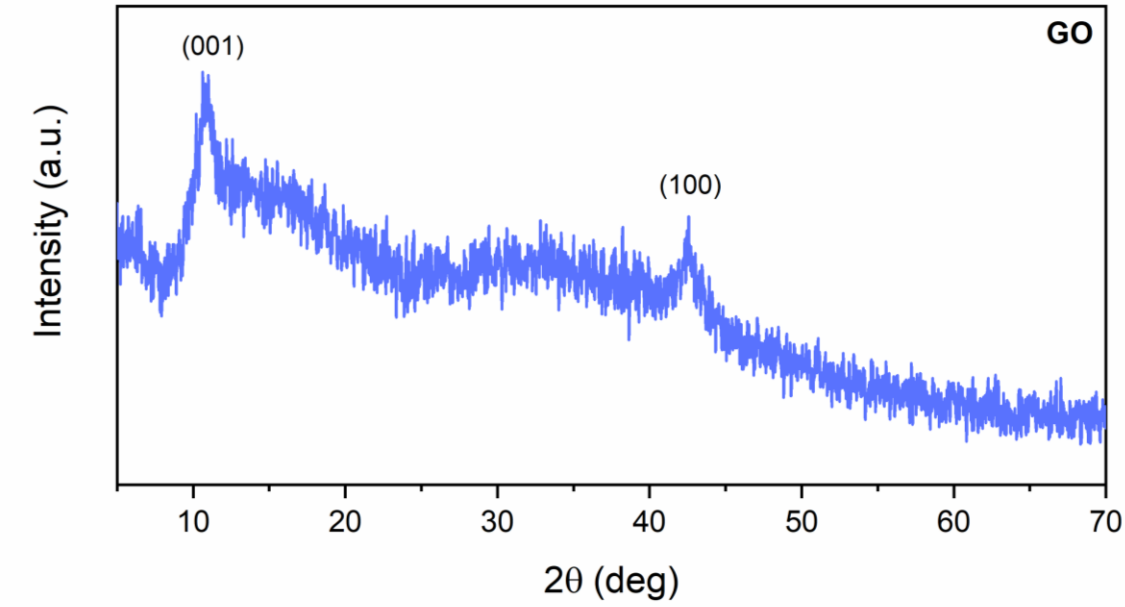

Figure 31 XRD pattern of GO

4.1.2.4 Field Emission Scanning Electron Microscope (FE-SEM)

Figure 32 depicts a micrograph of graphene oxide, captured with x50000 magnification. The micrograph shows the layered structure of graphene oxide with wrinkles and folds. (37) **Figure 33** shows the EDX spectrum of graphene oxide. As expected, EDX data presents Carbon (C) (56.06 wt.% , 62.98 at.%) and Oxygen (O) (43.94 wt.% , 37.02 at.%) elements, consistent with the functional groups identified by FTIR.

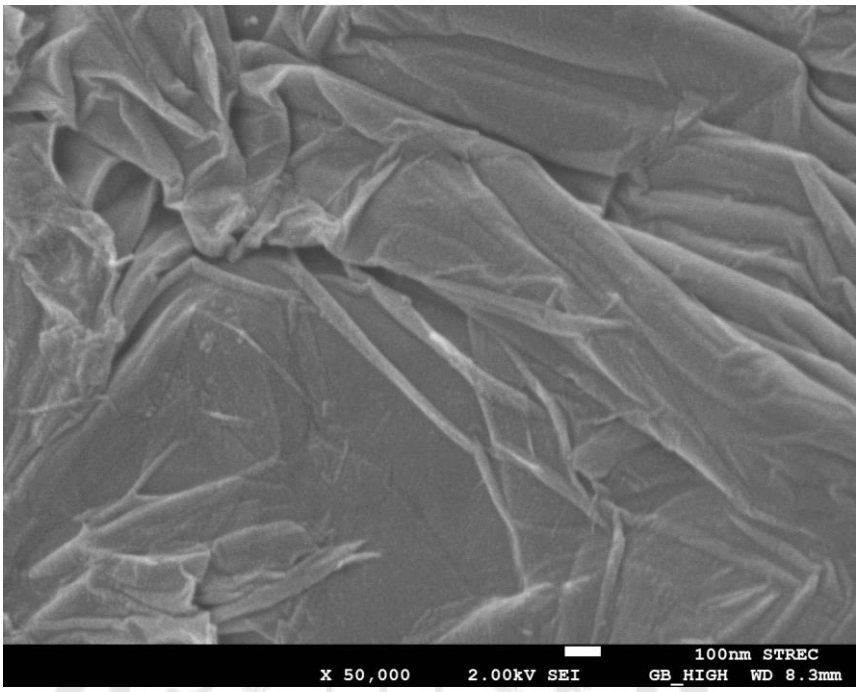

Figure 32 FE-SEM image of GO

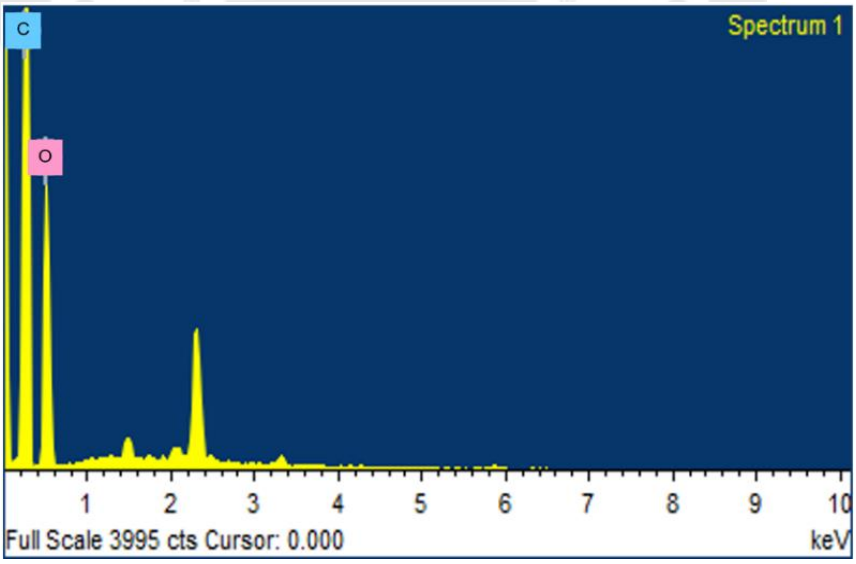

Figure 33 EDX spectrum of GO

4.1.3 Characterization of Zinc Oxide (ZnO)

The characterization of ZnO nanoparticles was conducted to evaluate their structural, optical, and morphological properties using Fourier Transform Infrared Spectroscopy (FTIR) to confirm Zn–O bonding and vibrational modes, Raman Spectroscopy to study lattice vibrations and crystalline structure, X-ray Diffraction (XRD) to identify the wurtzite structure and Scanning Electron Microscopy (SEM) combined with Energy Dispersive X-ray Spectroscopy (EDS) to investigate particle morphology and confirm elemental composition and purity.

4.1.3.1 Fourier transform infrared (FTIR)

The FTIR spectrum of ZnO is shown in **Figure 34**. The FTIR spectrum represents interatomic vibration peaks at 3439, 2926, 1626, 1447, 1024, 872 and 778 cm^{-1}. The distinctive peaks of the Zn-O bonding were located at around 1024 cm^{-1}. The absorption peak at 1626 and 1447 cm^{-1} results from the capping agent C=C stretching vibration. Meanwhile, Zn-O is confirmed by peaks at 1024, 872, and 778 cm^{-1}. Conversely, the stretching vibrations of O-H are indicated by the peak at 3439 cm^{-1}. (63)

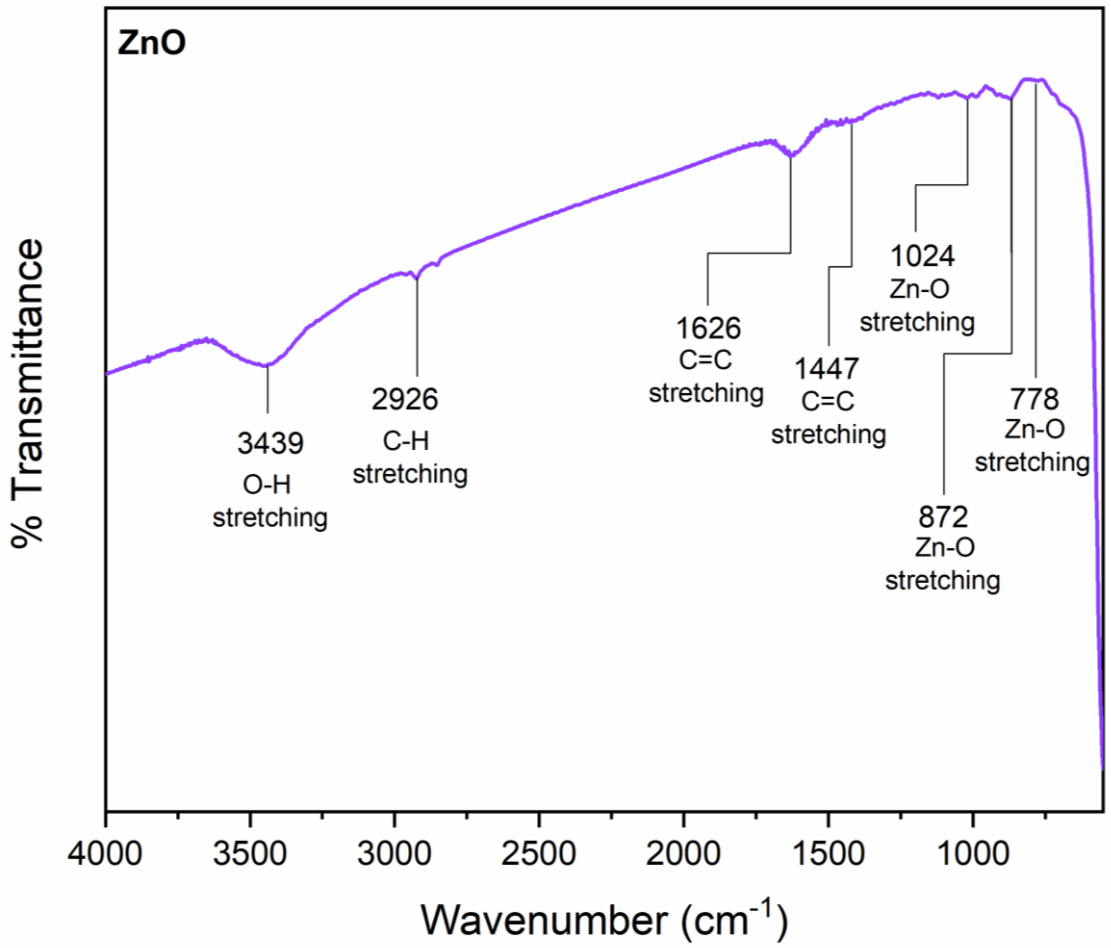

Figure 34 FTIR spectra of ZnO

4.1.3.2 Raman Spectroscopy

The Raman spectrum is shown in **Figure 35**. Concerning the ZnO nanocrystals are identified by bands at 333 cm^{-1} (second-order Raman processes, E_2-E_1 vibration modes), 437 cm^{-1} (E_2 high vibration mode, associated with oxygen atoms), and 584 cm^{-1}(A_1-E_1modes). The crystalline structure of ZnO is characterized by bands at 98 cm^{-1} (E_2 low, coupled with the Zn sublattice), 381 cm^{-1} (A_1), and 412 cm^{-1}(E_1). The two nonpolar low and high-frequency phonon modes (E_{2L} and E_{2H}) that make up the E_2 mode are linked to the vibration of the heavy Zn sublattice and oxygen atoms, respectively. The Raman selection rule states that the A_1, E_1, and E_2 modes are first-order Raman-active modes. Additionally, Raman peaks, situated approximately at 663 cm^{-1}, may

originate from the multi-phonon scattering modes 2(E_{2H}-E_{2L}). Furthermore, a broad Raman peak corresponding to the acoustic combination of A_1 and E_2 is observed between 1102 and 1152 cm^{-1}. Approximately 1129 cm^{-1}, the broad peak, is expected to represent a part of the multi-phonon process. (64)

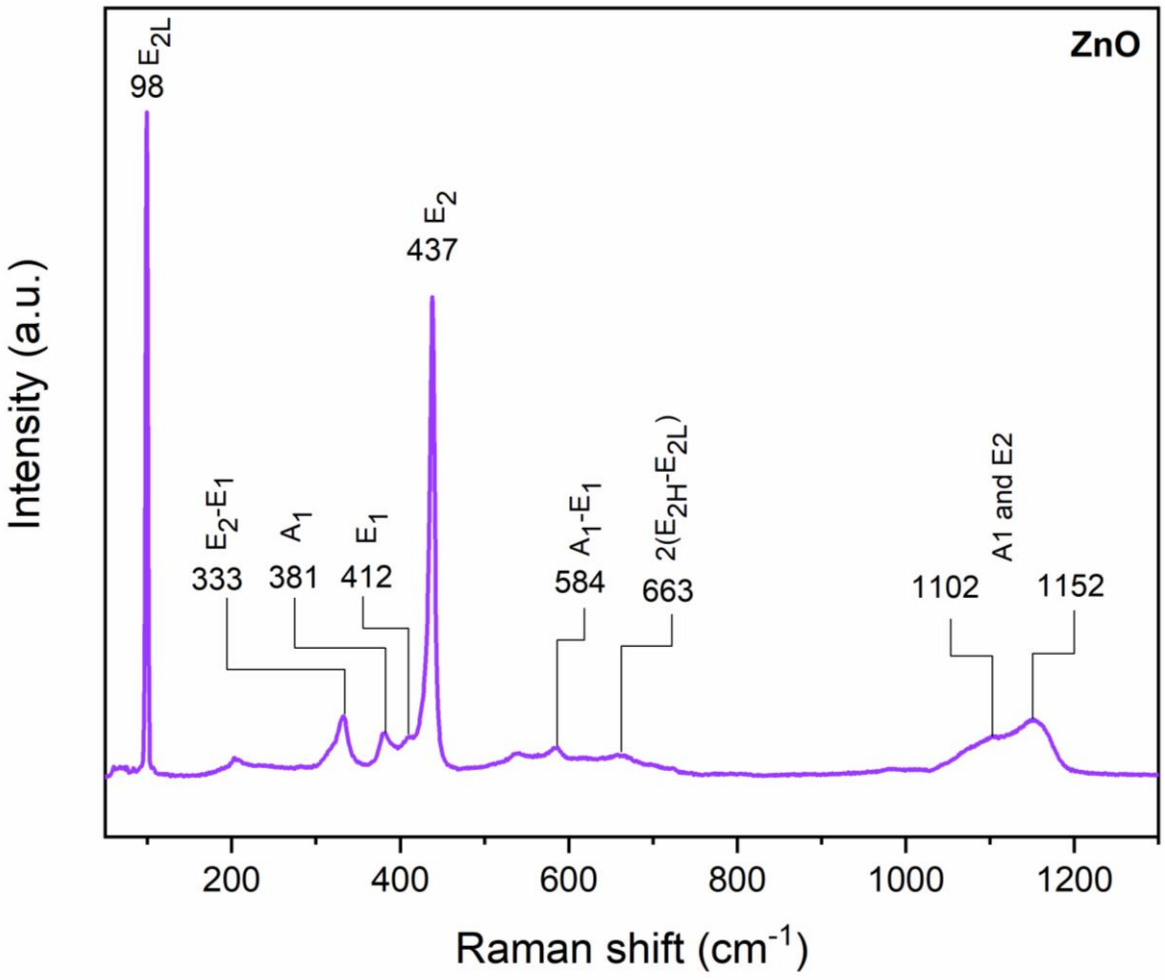

Figure 35 Raman spectra of ZnO

4.1.3.3 X-ray Diffraction (XRD)

XRD investigated the phase analysis of ZnO, as shown in **Figure 36**. Peak observed at the 2θ of 31.75°, 34.41°, 36.24°, 47.53°, 56.59°, 62.86°, 66.37°, 67.95°, 69.14°, 72.57° and 76.99° corresponding with those from (100), (002), (101), (102), (110), (103), (200), (112), (201), (004) and (202) reflections, respectively, of the hexagonal wurtzite crystal structure of ZnO with JCPDS card no. 36-1451. The crystallite size of ZnO, with a mean value of 46.44 nm, was determined using the Debye–Scherrer method, as shown in **Table 9**. (65–67)

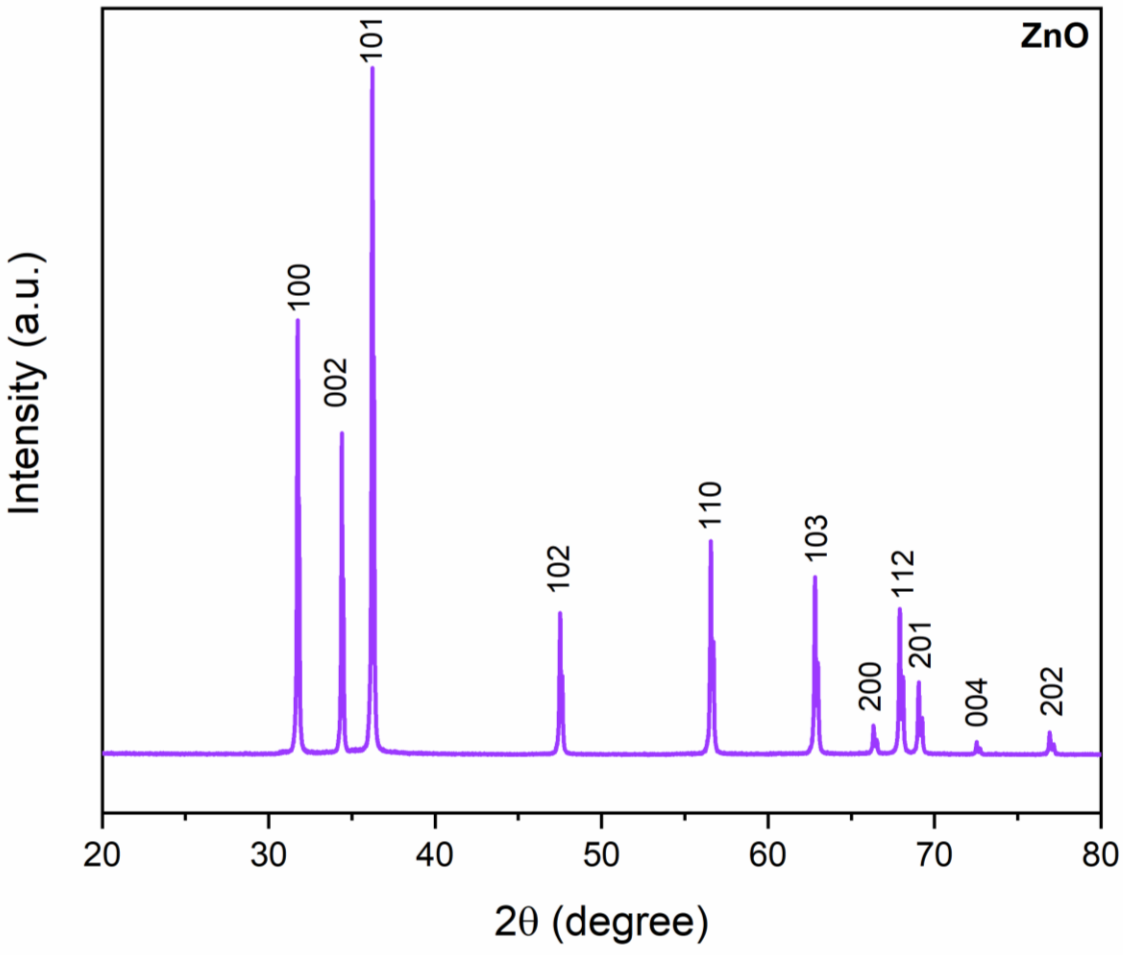

Figure 36 XRD patterns of ZnO confirming its wurtzite hexagonal crystalline structure

Table 9 Calculated crystallite sizes of the ZnO (Mean: 46.44 nm) by Debye–Scherrer method.

(26)

2θ	FWHM	Cos θ	Size (nm)
31.75	0.16	0.96	55.60
34.41	0.16	0.96	55.77
36.24	0.17	0.95	51.10
47.53	0.21	0.92	42.90
56.59	0.24	0.88	38.75
62.86	0.27	0.85	35.87
67.95	0.29	0.83	34.26
69.14	0.18	0.82	57.28
Crystalline size average			**46.44**

4.1.3.4 Field Emission Scanning Electron Microscope (FE-SEM)

FE-SEM image (**Figure 37**) shows the surface morphology of the ZnO particles with an average particle size of 137 nm. The image confirms the crystallinity and the hexagonal shape of ZnO particles, which agree with the XRD result characteristic of ZnO stable crystalline structure. (68) The EDX spectrum (**Figure 38**) involves Zinc (Zn) (79.5 wt.%, 48.69 at.%) and Oxygen (O) (20.5 wt.%, 48.69 at.%). The crystallite size distribution of ZnO (**Figure 39**) aligns with the FE-SEM image, ranging from 50 to 400 nm.

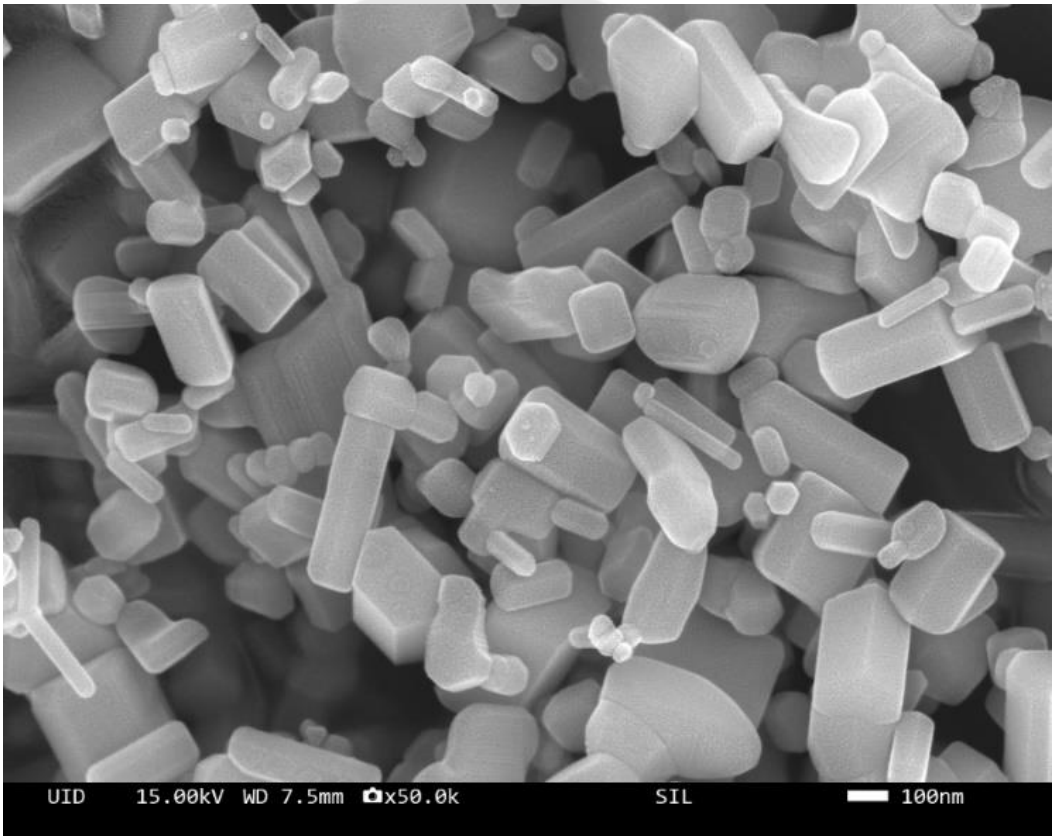

Figure 37 FE-SEM of ZnO

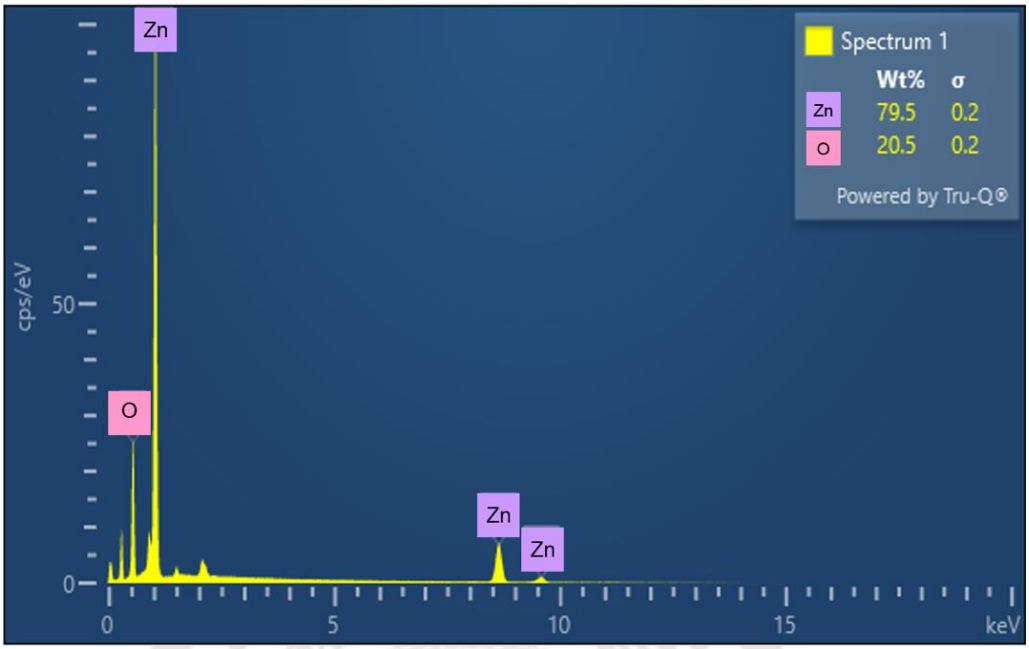

Figure 38 EDX spectrum of ZnO

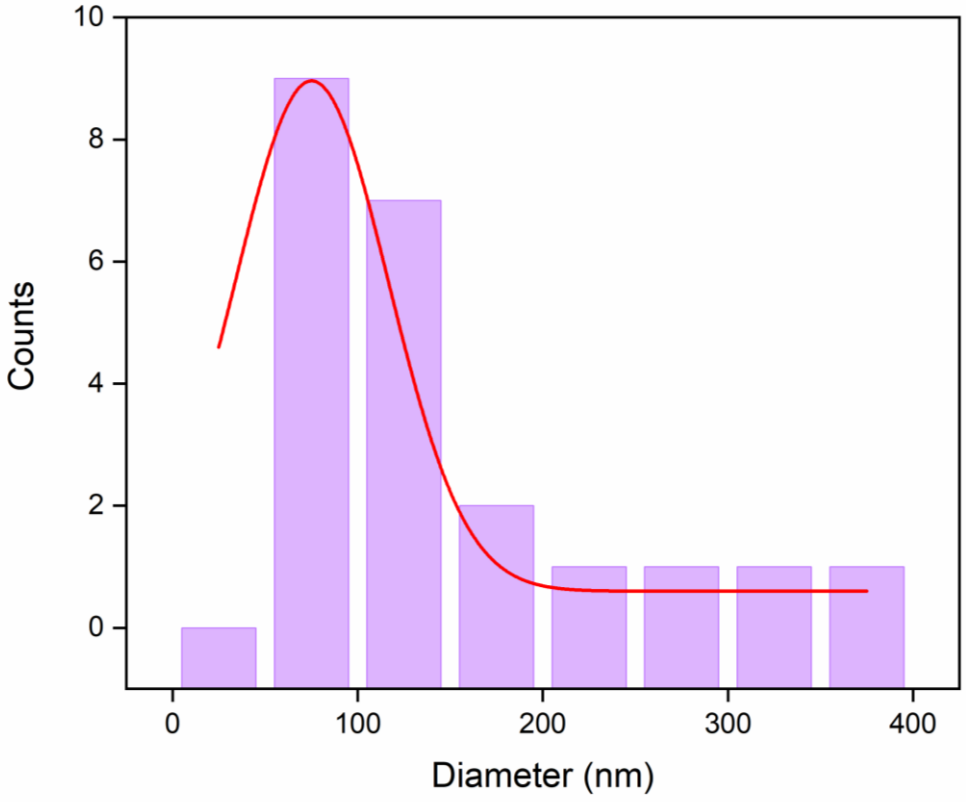

Figure 39 Size distribution of ZnO

4.2 Effect of multiple coating layers on hydrophobic properties of TNPsGZ-coated fabrics

4.2.1 Characterization of TNPsGZ composite

The TNPsGZ composite materials were prepared using TiO_2, graphene oxide, and ZnO. The structural properties of these composites were analyzed using FTIR to identify the functional groups and confirm the successful integration of the components. The results provide insights into the chemical interactions that influence the composite's performance.

4.2.1.1 Fourier transform infrared (FTIR)

The FTIR spectra of the TNPsGZ composites as shown in **Figure 40**. Notably, a broad absorption band at 680 cm^{-1} corresponds with the Zn-O stretching vibration. The spectra further reveal prominent peaks associated with GO-specific peaks, such as the skeletal vibration of unoxidized graphite domains at 1626 cm^{-1}, asymmetric C-H vibrations at 2922 cm^{-1}, and O-H stretching at 3456 cm^{-1}.(69) Given the TiO_2 to ZnO weight ratio in this composite, the Zn-O peaks within the 400-1000 cm^{-1} range are anticipated to be more prominent, reflecting the significant presence of ZnO in the composite structure. (30) A summary of the FTIR absorption bands and their corresponding vibrations is provided in **Table 10**.

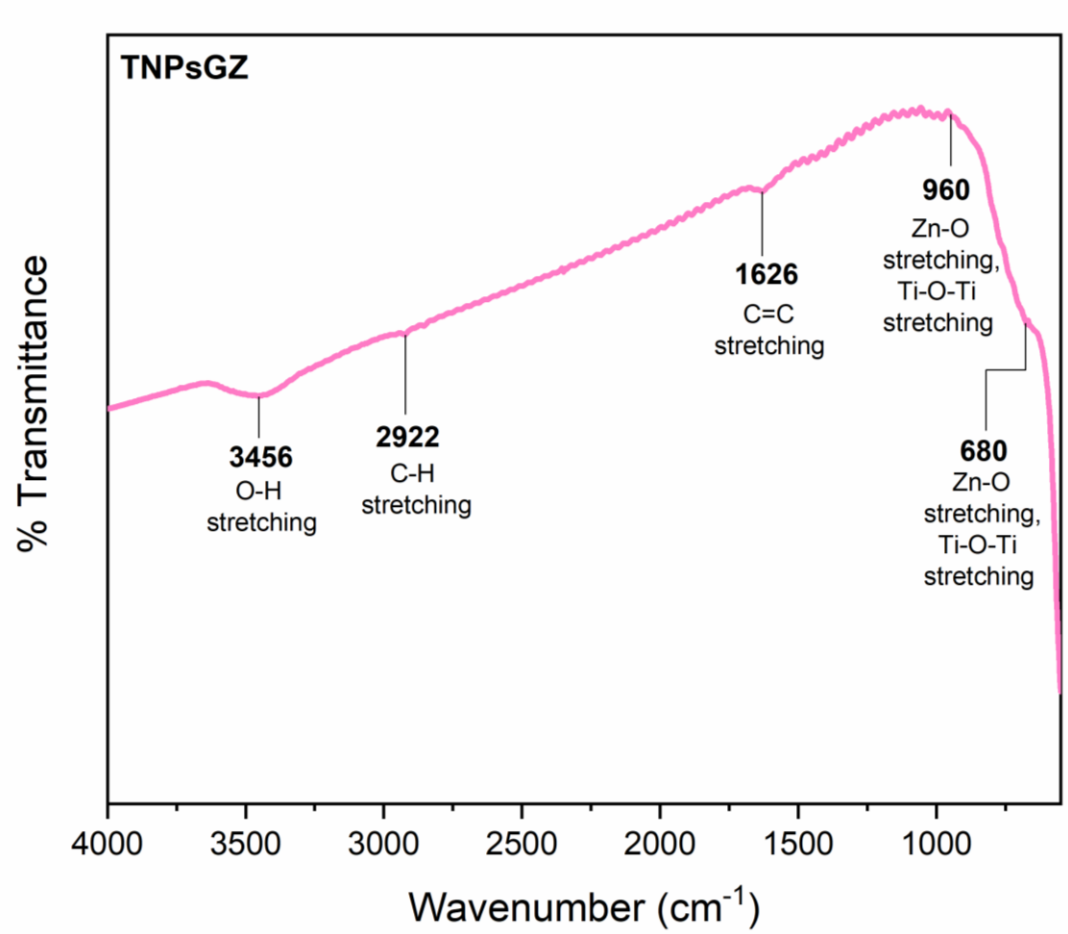

Figure 40 FTIR spectra of TNPsGZ

Table 10 FT-IR peaks for identification in TNPsGZ composite

Wavenumber (cm^{-1})	Characteristic bond
3456	O-H stretching
2922	C-H stretching
1626	C=C stretching
960	Zn-O, Ti-O stretching
680	Zn-O, Ti-O stretching

4.2.2 Characteristics of Cotton Fabric and TNPsGZ-Coated Fabric

4.2.2.1 Fabric Appearance

Figure 41 presents the untreated plain weave cotton fabric, highlighting its surface structure under **Figure 41(a)** normal visual inspection and **Figure 41(b)** optical microscope observation at 500x magnification. This serves as a baseline for comparison with the coated samples. **Figure 42** illustrates the appearance of the cotton fabric coated with TNPsGZ before and after the curing process. The initial white color of the cotton fabric remains mostly unchanged after coating, regardless of the number of TNPsGZ layers applied. Additionally, the curing process does not visibly alter the fabric's color, preserving the original material's aesthetic. Upon closer inspection under the optical microscope at 500x magnification, the TNPsGZ coating appears transparent, evenly covering the cotton fabric surface and permeating the spaces between the yarns. Notably, graphene oxide particles are seen to have infiltrated into the yarn structure, indicating good penetration and integration of the composite material with the fabric.

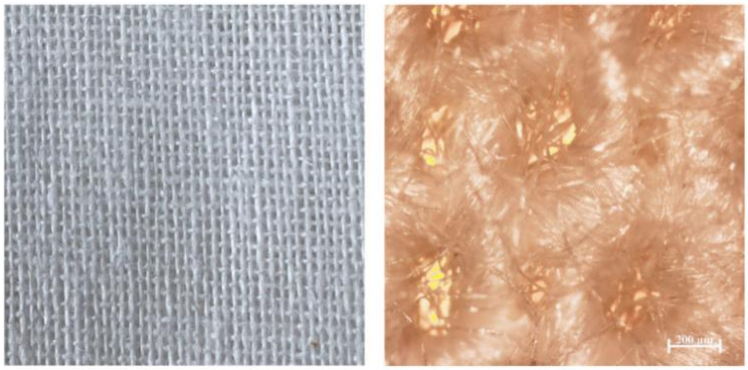

Figure 41 shows cotton fabric: a) cotton fabric used in the experiment, and b) optical microscope image at 500x magnification.

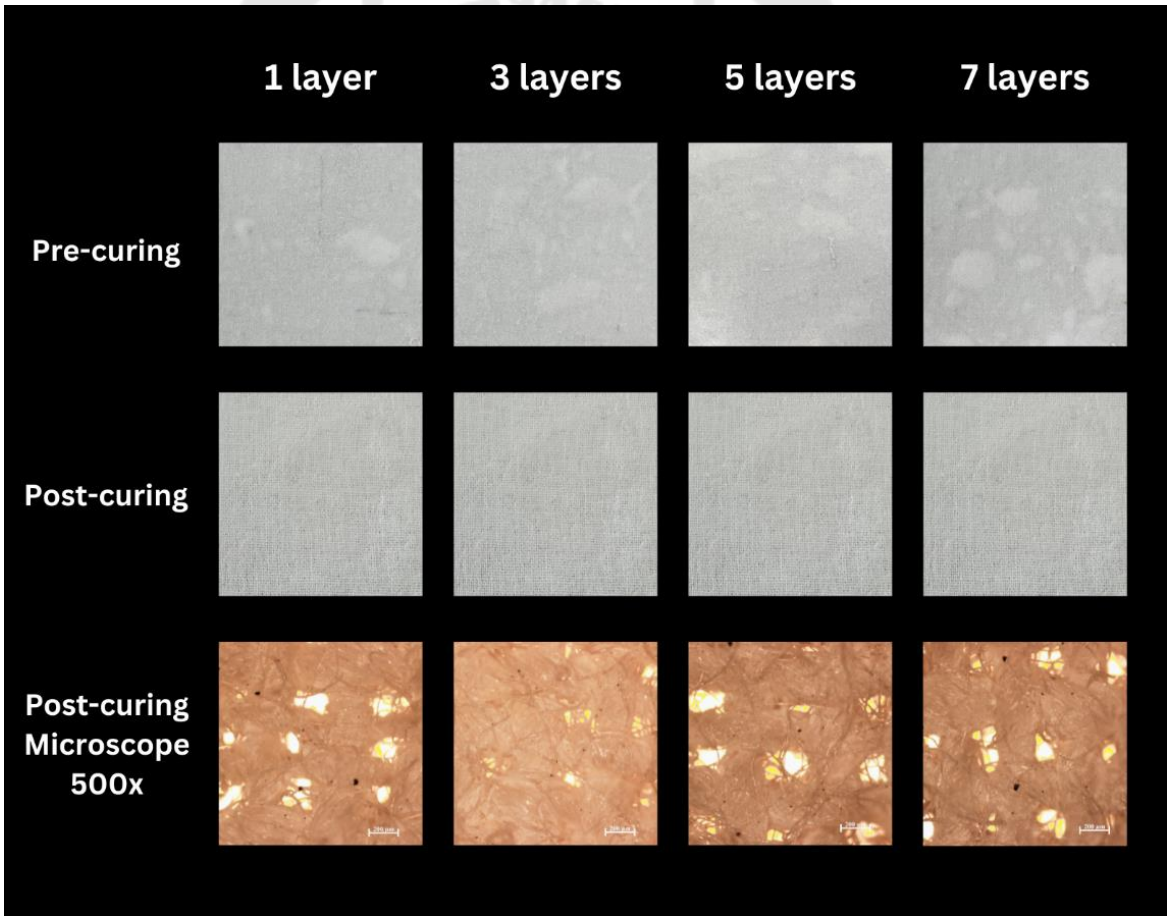

Figure 42 Appearances of cotton fabric coated with TNPsGZ in varying layer numbers (1, 3, 5, and 7 layers), showing the differences in pre-curing, post-curing, and detailed surface morphology observed under an optical microscope at 500x magnification.

4.2.2.2 Surface Morphology of Fabrics

Figure 43(a) reveals the yarns of untreated cotton fabric with a smooth surface without particles on its surface. After the first coating, **Figure 43(b)** shows a homogeneous distribution of TNPsGZ particles on the yarn surface. The PVP binder is very helpful in the permanence of composite particles in cotton fabric. Moreover, with the increase in the number of coating layers, TNPsGZ particles were found to integrate into a thin TNPsGZ film on the cotton fiber surface (**Figure 43(d-e)**). After one wash (**Figure 43(f)**), the TNPsGZ particles remain tightly adhered to the surface of the cotton fabric.

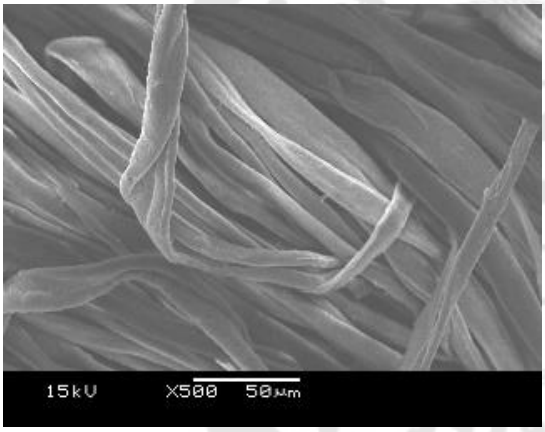

a.

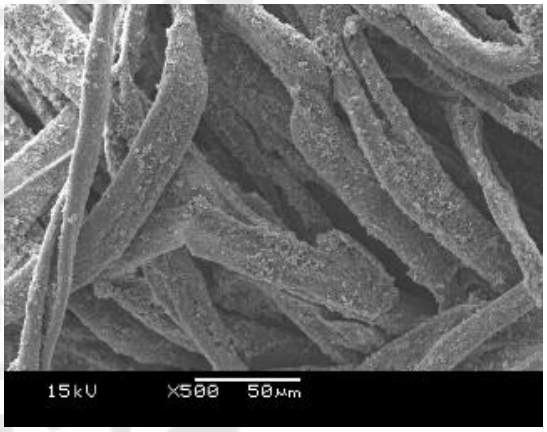

b.

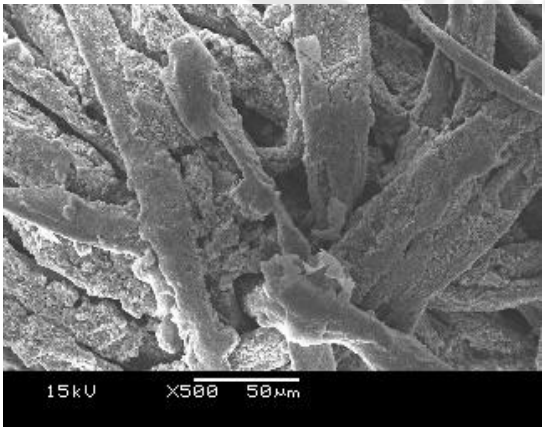

c.

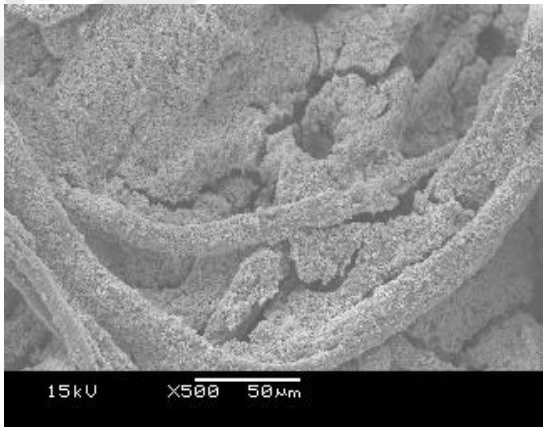

d.

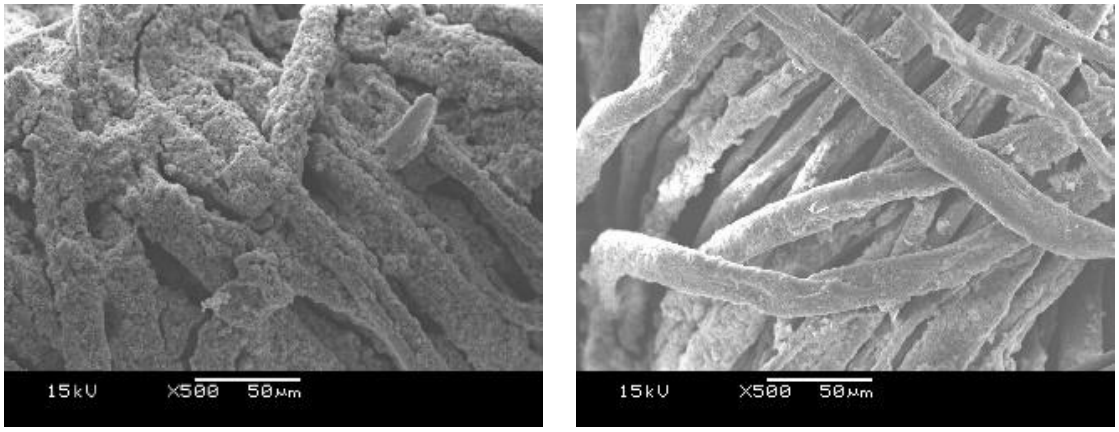

e. f.

Figure 43 SEM image of cotton fabric (a) the untreated cotton fabric and the TNPsGZ-coated cotton fabric, (b) 1-layer coating, (c) 3-layer coating, (d) 5-layer coating, (e) 7-layer coating and (f) a 1-layer coating after one wash.

4.2.2.3 Analysis of Functionalized Cotton Fabrics with TNPsGZ Composite

The chemical characteristics of cotton fabric, TNPsGZ-coated cotton fabric, and TNPsGZ-coated cotton fabric after one wash were examined using FT-IR analysis. According to Vaideki et al. and Ahmad et al. (70,71), **Figure 44** depicts the FT-IR spectrum of untreated cotton fabric. The spectrum demonstrates vibrational modes of C=O stretching, C-O stretching, and O-H deformation between 1,200 and 1,700 cm^{-1}. A peak in the 2,800 cm^{-1} region is attributed to OH-C=O, while the broad peak observed between 3,100 and 3,500 cm^{-1} represents O-H stretching vibrations from H-bonded hydroxyl groups. Additionally, a peak at 891 cm^{-1} corresponds to the asymmetric stretching of C1-O-C4 in cellulose.

In the TNPsGZ/PVP composite coated on cotton fabric spectrum, the peak at 3,407 cm^{-1} is linked to the stretching vibrations of hydroxyl groups (O-H), indicating PVP on the coated fabric surface. Peaks related to asymmetric (2,943 cm^{-1}) and symmetric (2,892 cm^{-1}) CH_2 stretching confirm the presence of aliphatic hydrocarbons. A band at 1,646 cm-1 represents the C=O stretching, characteristic of pure PVP. Moreover, the FT-IR spectra of multilayered TNPsGZ-coated fabrics show an increase in peak intensity **Figure 45**. The –C–N stretching at 1,422 cm^{-1} and –C–H bending at 1,280 cm^{-1}, attributed to the PVP polymer, further validate PVP's presence in the composite.(72)

For the TiO_2 in composite, the broad absorption band at 450-800 cm^{-1} corresponds to Ti–O–Ti stretching vibrations, signifying the incorporation of TiO_2 within the PVP matrix. This observation aligns with previous findings that confirm strong interactions between the polymer matrix and the nanoparticles through the carbonyl (C=O) group. (72) For the ZnO in composite, Singh et al. identified key FT-IR peaks, including C=O stretching (1,646 cm^{-1}), O-H stretching (3,407 cm^{-1}), and CH2 stretching (2,943 and 2,892 cm^{-1}), indicating strong interactions between the C=O group and Zn^{2+} ions on ZnO nanoparticles. The Zn-O stretching (~450-500 cm^{-1}) remains distinct, confirming the coexistence of ZnO and PVP (73)

The FT-IR spectra of the washed cotton fabric, shown in **Figure 46**, reveal notable changes. The peak intensity of the band at 1,650 cm^{-1} is reduced, suggesting that the washing process may have altered the coating's chemical composition. These results highlight the necessity of understanding how washing and environmental conditions impact the performance and longevity of coated fabrics.

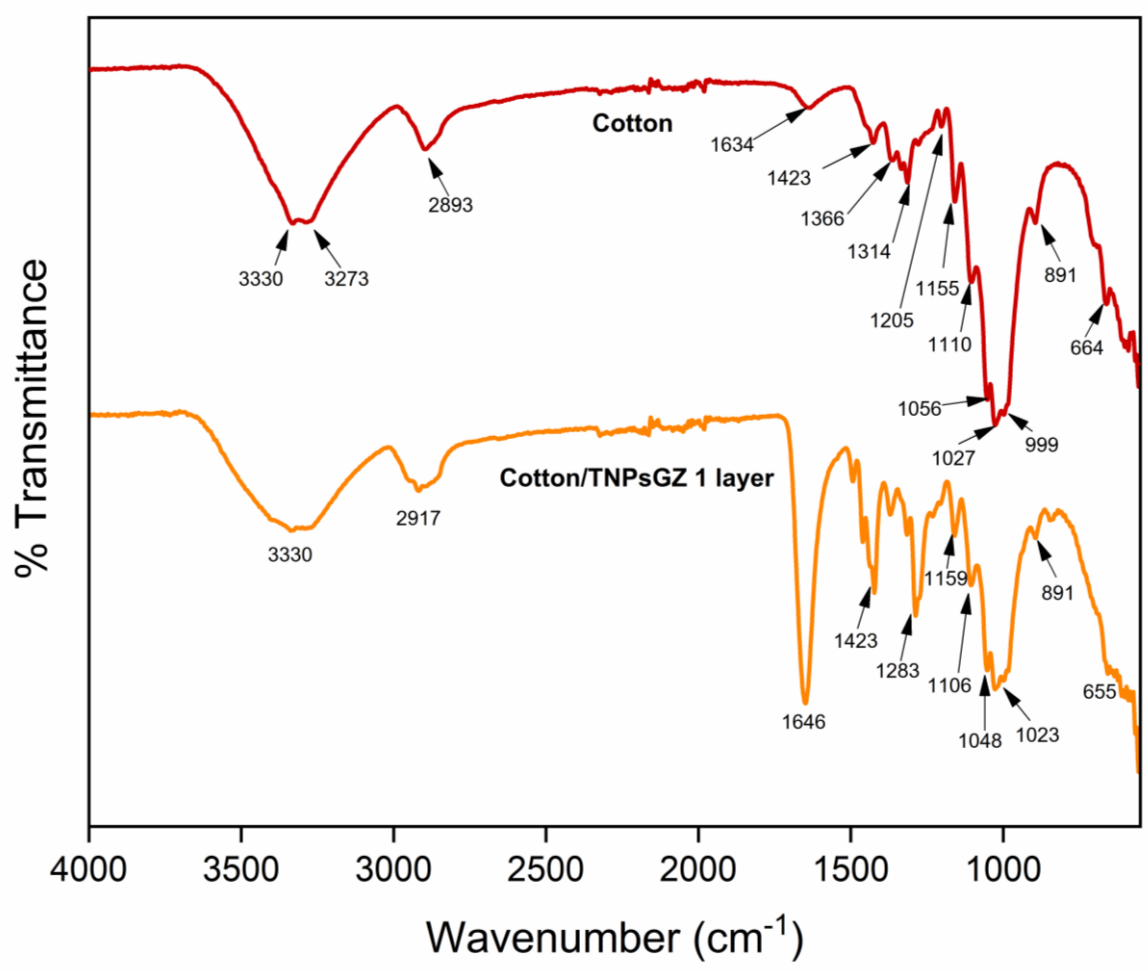

Figure 44 FTIR spectra of cotton fabric (red line)
and 1 layer of the TNPsGZ-coated cotton fabric (orange line)

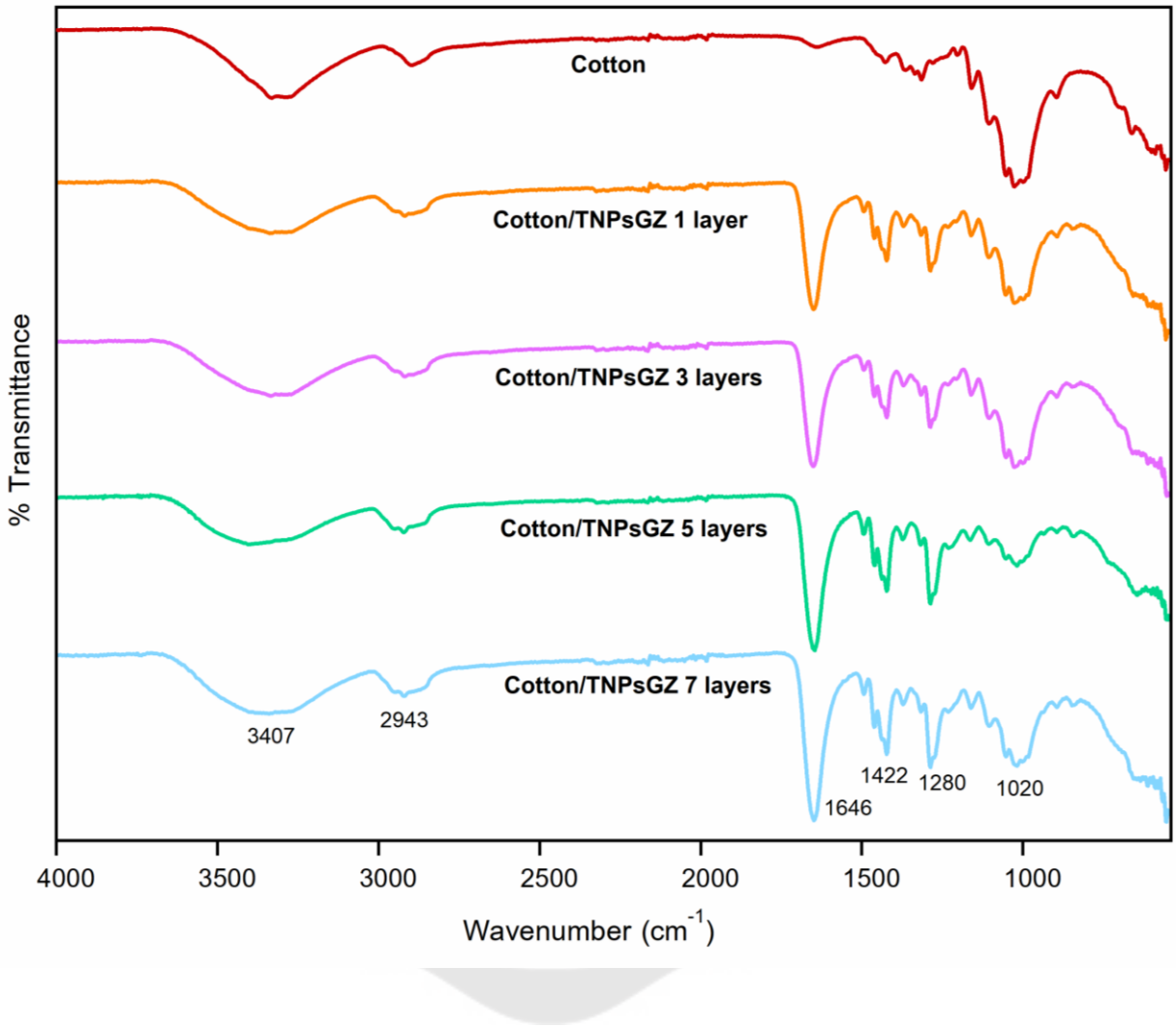

Figure 45 FTIR spectra of cotton fabric and

the different coated layers of the TNPsGZ-coated cotton fabric

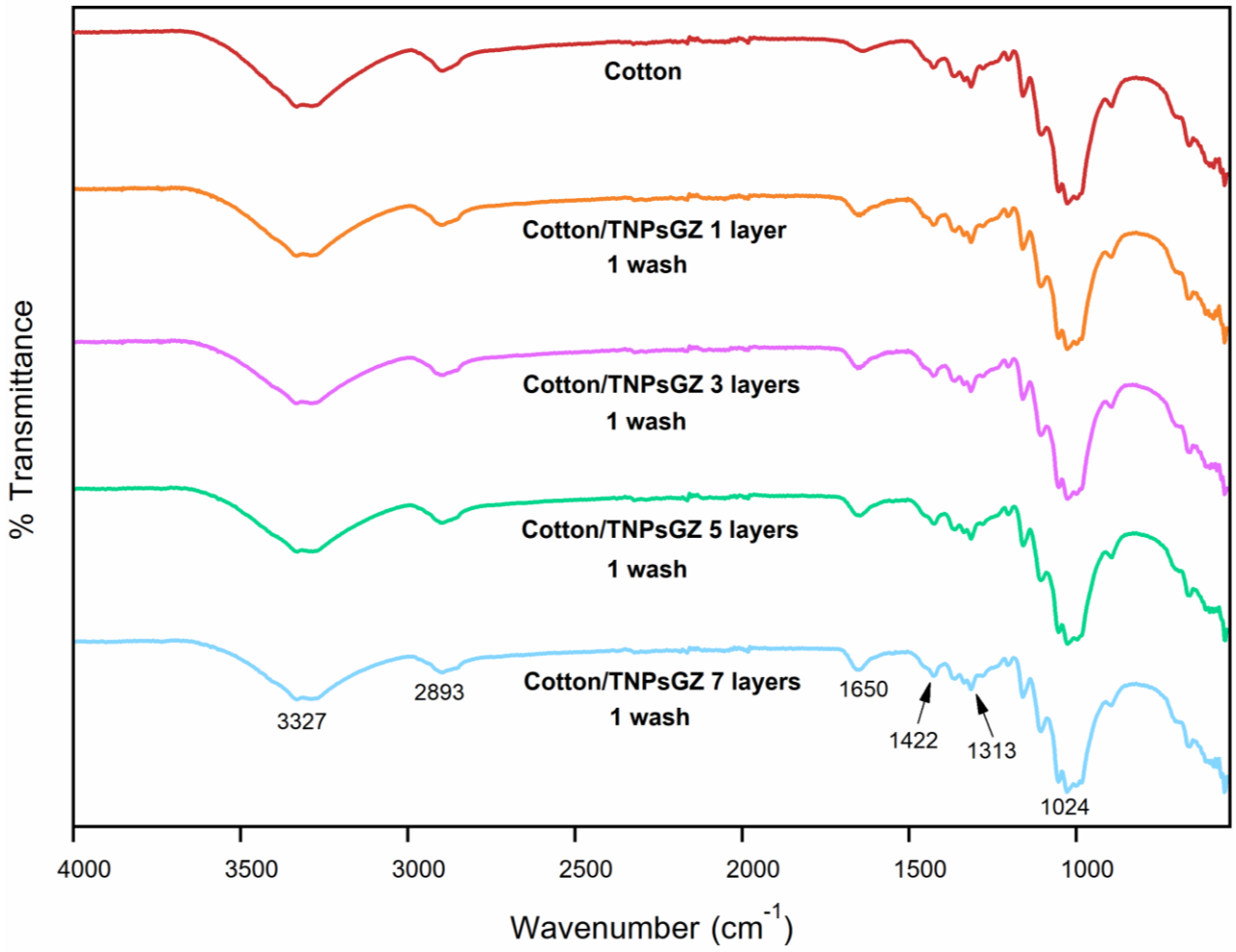

Figure 46 FTIR spectra of cotton fabric and

the different coated layers of the TNPsGZ-coated cotton fabric after one wash

4.2.3 Hydrophobic property of cotton fabrics coated with TNPsGZ composite

The contact angle measurement assesses the surface wettability of both untreated and modified cotton fabrics. Water droplets were instantly absorbed by the pristine cotton fabric, resulting in no measurable contact angle. **Figure 47** presents the results of water contact angles for TiO_2-coated, ZnO-coated, and various layers of TNPsGZ-coated cotton fabrics. TiO_2-coated cotton exhibits strong hydrophilicity with a water contact angle of 0°. In contrast, the ZnO-coated cotton fabric demonstrates hydrophobic properties, with an average contact angle of 78.5°.

In comparison, fluoropolymer-based coatings demonstrated in other studies exhibited superior hydrophobicity, retaining water contact angles above 120° even after 10 wash cycles. which significantly outperformed TNPsGZ-coated fabrics in terms of wash durability and long-term water repellency. (9)

After coating the cotton fabric with TNPsGZ, the water absorption capability of the fabric increased. The average water contact angles on the TNPsGZ-coated fabric ranged between 70° and 85°. Notably, increasing the number of coating layers did not significantly alter the contact angle of the coated fabrics. After a single wash, the contact angle decreased to 29°, likely due to the partial removal of the coating from the fabric surface. This leaching effect was corroborated by SEM analysis, as shown in **Figure 44(f)**, which revealed changes in the surface morphology of the TNPsGZ-coated cotton fabric post-washing.

To impart hydrophobic properties to cotton fabric, the TNPsGZ composites were applied using the dip-dry-cure method, which offers several advantages, including low cost, user-friendliness, and non-destructive processing. SEM analysis indicated that the TNPsGZ composites uniformly coated each cotton sample without any signs of splintering. The addition of poly(N-vinylpyrrolidone) (PVP) as a stabilizing agent played a significant role in ensuring uniform dispersion of nanoparticles, as previously demonstrated by Gutul et al. in their study of PVP-stabilized ZnO colloids.(74) The TNPsGZ composites combined with PVP were effective in producing hydrophobic cotton fabrics with higher water contact angles than those of

pristine cotton. For the sample coated with a single layer, the water contact angle reached 85°. However, the observed water contact angle was still below 90°, which suggests that the synergistic effect between TiO_2, ZnO, and PVP in the composite could be optimized further to achieve superhydrophobicity. Singh et al. also noted that PVP improved the uniformity and functional performance of ZnO nanoparticles, which may play a crucial role in future experiments to enhance hydrophobic properties.(73) Although a noticeable increase in water contact angle was achieved with the TNPsGZ composite coating, the resulting angle remained below 90° in the mixed nanoparticle system. This outcome fell short of the research' s objective to create tertiary nanocomposites capable of achieving superhydrophilicity. Enhanced hydrophobic properties might be achieved with an optimal combination of TiO_2, ZnO, and PVP.

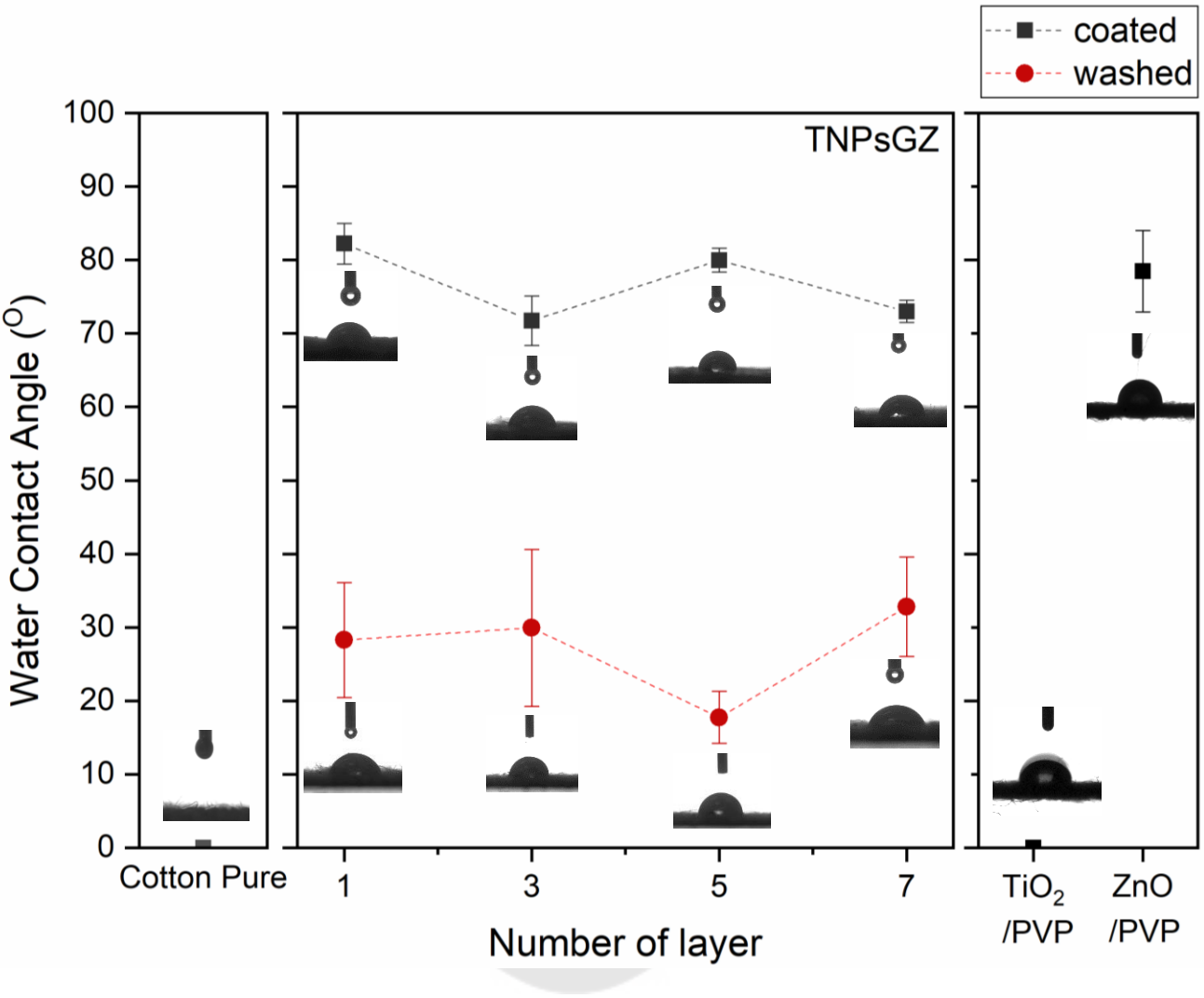

Figure 47 The shape of water droplets and contact angles on the surface of the layer of TNPsGZ-coated on cotton fabric (black line) and the layer of TNPsGZ-coated on cotton fabric after one wash (red line).

Building on the findings from 4.2, which demonstrated that a single-layer coating was sufficient for achieving hydrophobicity, it was also observed that increasing the number of TNPsGZ coating layers did not significantly improve water resistance. Therefore, in 4.3, the focus shifts toward optimizing the PVP ratio to enhance hydrophobic properties further while also adjusting the TG: ZnO ratios to 1:1, 1:3, 1:5, and 1:7. This refinement aims to comprehensively evaluate how these compositional modifications impact the structural, morphological, and functional characteristics of the TNPsGZ-coated fabrics, ensuring the material's adaptability and performance across different applications. (75) ZnO was used in higher ratios compared to TiO_2 because it demonstrated superior antibacterial properties, as shown in the study by M. Mintu Ali et al. ZnO releases Zn^{2+} ions that disrupt bacterial membranes and generate reactive oxygen species (ROS), enhancing its ability to inhibit bacterial growth effectively (76)

4.3 Impact of TG: ZnO ratios on hydrophobicity, UV-protection, and antibacterial activity of TNPsGZ-Coated Fabrics

4.3.1 Characterization of TNPsGZ composite

The characterization of TNPsGZ composites was performed to examine the effects of varying TG: ZnO ratios (1:1, 1:3, 1:5, and 1:7) on the structural, chemical, and morphological properties of the material. Analytical techniques, including Fourier Transform Infrared Spectroscopy (FTIR), Raman Spectroscopy, X-ray Diffraction (XRD), Scanning Electron Microscopy (SEM), and Energy Dispersive X-ray Spectroscopy (EDS), were employed to analyze bonding, crystalline phases, structural composition, particle morphology, and elemental distribution, providing insights into the interactions between TiO_2, GO, and ZnO in the composite.

4.3.1.1 Fourier transform infrared (FTIR)

The FTIR spectra of the TNPsGZ composite are shown in **Figure 48**. These results demonstrate the interaction between the TiO_2/GO/ZnO. The peaks located at approximately 3450, 1640, and 1433 cm^{-1} are attributed to the stretching vibration of the hydroxyl group, while carboxyl C=O and C-O cause the bands. The FTIR spectra of the TNPsGZ composite peaks that correspond to TiO_2 are shown in **Figure 49**. A summary of the TiO_2 peak identifications is provided in **Table 11**. The stretching modes of Ti-O and Ti-O-Ti bridging are characterized by significant absorption bands of 1000 to 400 cm^{-1}. Notably, the broad band spanning 650 - 450 cm^{-1} corresponds to the Ti-O-Ti bridging stretching vibrations, while the peak found at about 778 cm^{-1} is attributed to the Ti-O stretching vibration. In the TNPsGZ (TG: ZnO) with a 1:1 ratio, the pronounced peak intensity at around 820 cm^{-1} corresponds to a vibrational mode associated with the TiO_2 component. (57)

FTIR spectra of the TNPsGZ composite peaks that correspond to GO, as shown in **Figure 50**. A summary of the GO peak identifications is provided in **Table 12**. In GO, the sharp peak observed at approximately 1621 cm^{-1}, indicates the sp_2 hybridized carbon found in the graphene structure is caused by the carbon double bond (C= C stretching). The peak of C= O related at 1367 cm^{-1}, which is connected to epoxy or alkoxy groups, represents the C–O stretching bond. The peak at 1057 cm^{-1} displays the C–O–H vibration mode and indicates the presence of hydroxyl groups. The peak at 1635 cm^{-1} generally corresponds to the stretching vibrational of the C=O bond (carbonyl group) within the carboxyl (-COOH) group. The peak at 1415 cm^{-1} is attributed to the bending of the C-O bond. (58,69)

FTIR spectra of the TNPsGZ composite peaks that correspond to ZnO as shown in **Figure 51**. A summary of the ZnO peak identifications is provided in **Table 13**. In ZnO, the peak of Zn-O was observed at approximately 1024 cm^{-1}. The absorption peaks at 1626 and 1447 cm^{-1} are attributed to the C=C stretching vibration of the capping agent. Meanwhile, the peaks at 1024, 872, and 778 cm^{-1} confirm the presence of Zn-O. The broad absorption peak around 659 cm^{-1} is associated with the

Zn-O stretching vibration in ZnO. This peak is indicative of the characteristic vibrational mode of the ZnO lattice structure. The TNPsGZ (TG: ZnO) composite can be observed in the broad peak at approximately 624 cm^{-1}. (30) What remains unclear in this part of the analysis requires further investigation. The results from Raman and XRD need to be analyzed in greater detail.

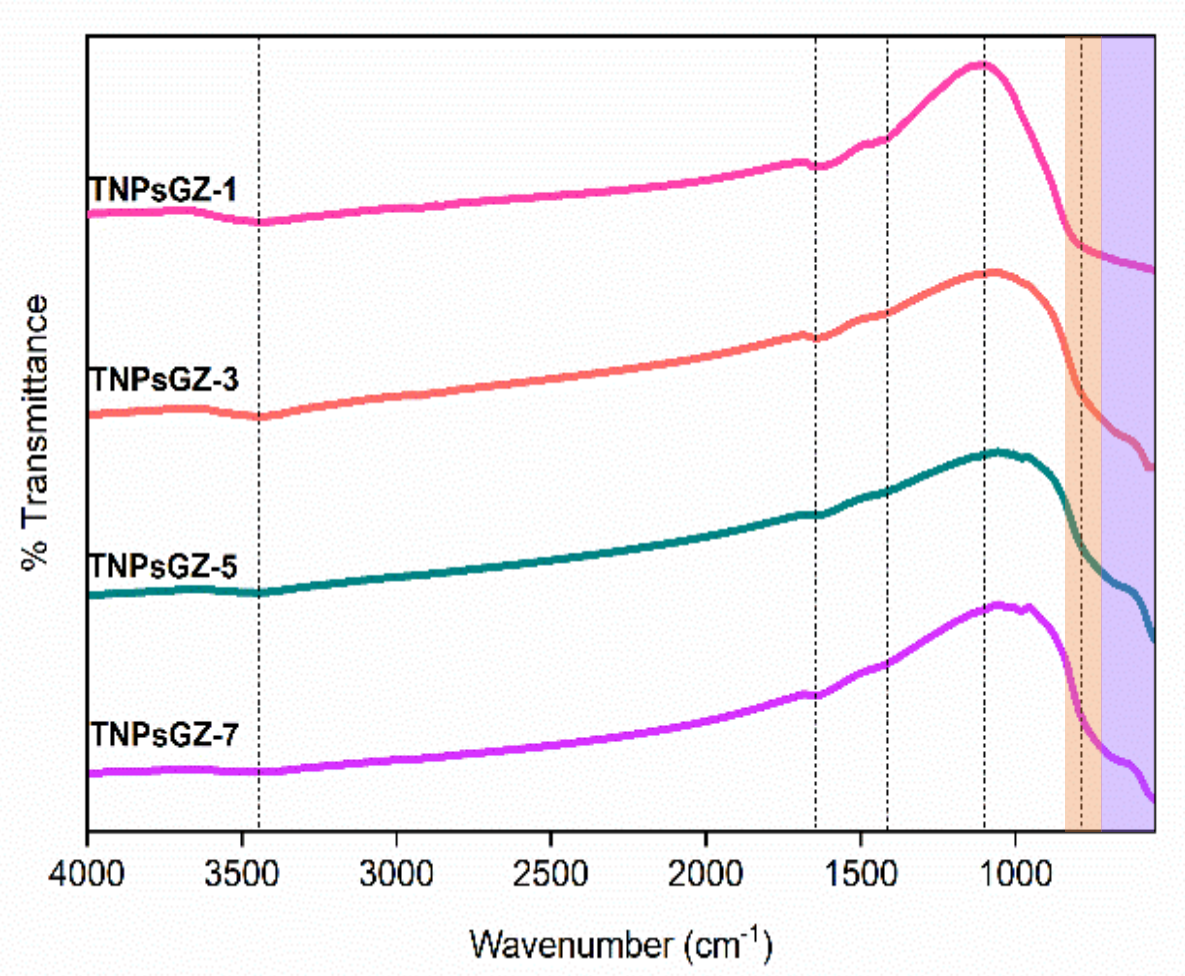

Figure 48 An overview of the FTIR spectra of TNPsGZ based on the TG: ZnO ratios (1:1, 1:3, 1:5, 1:7) is provided to outline key functional groups and trends before comparing the materials individually.

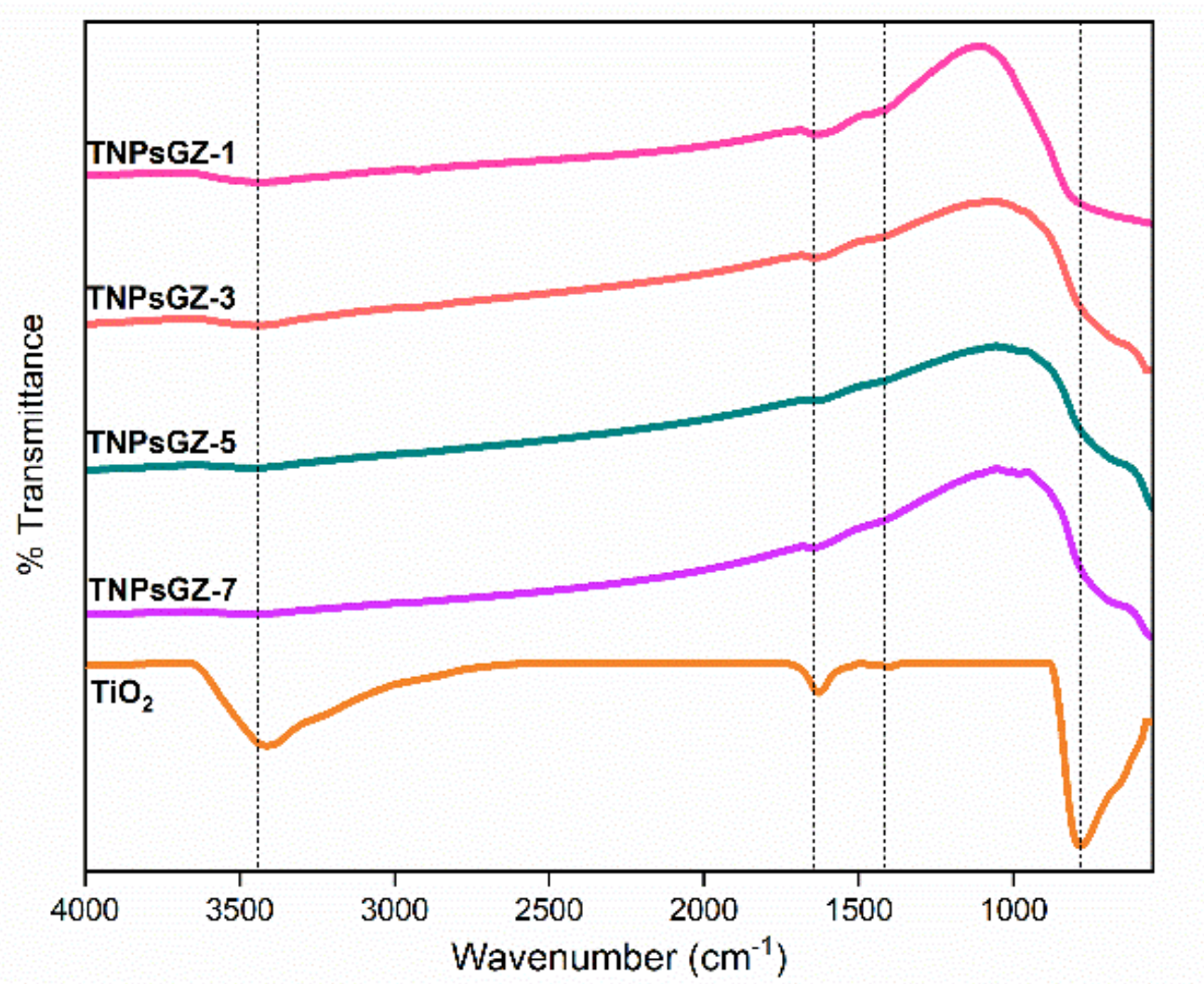

Figure 49 FTIR spectra of TNPsGZ based on the TG: ZnO ratios (1:1, 1:3, 1:5, 1:7) compare with TiO_2

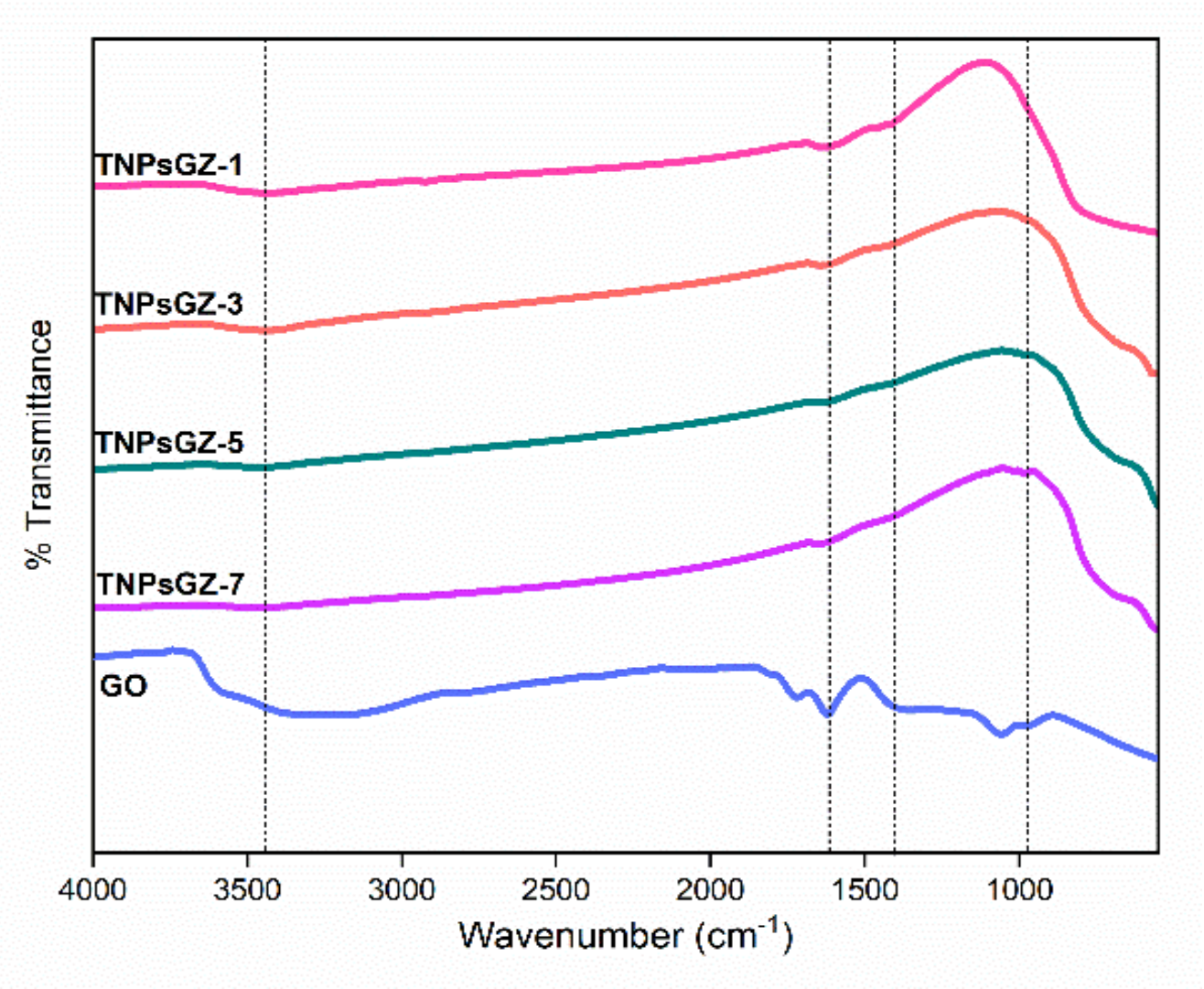

Figure 50 FTIR spectra of TNPsGZ based on the TG:ZnO ratios (1:1, 1:3, 1:5, 1:7) compare with GO

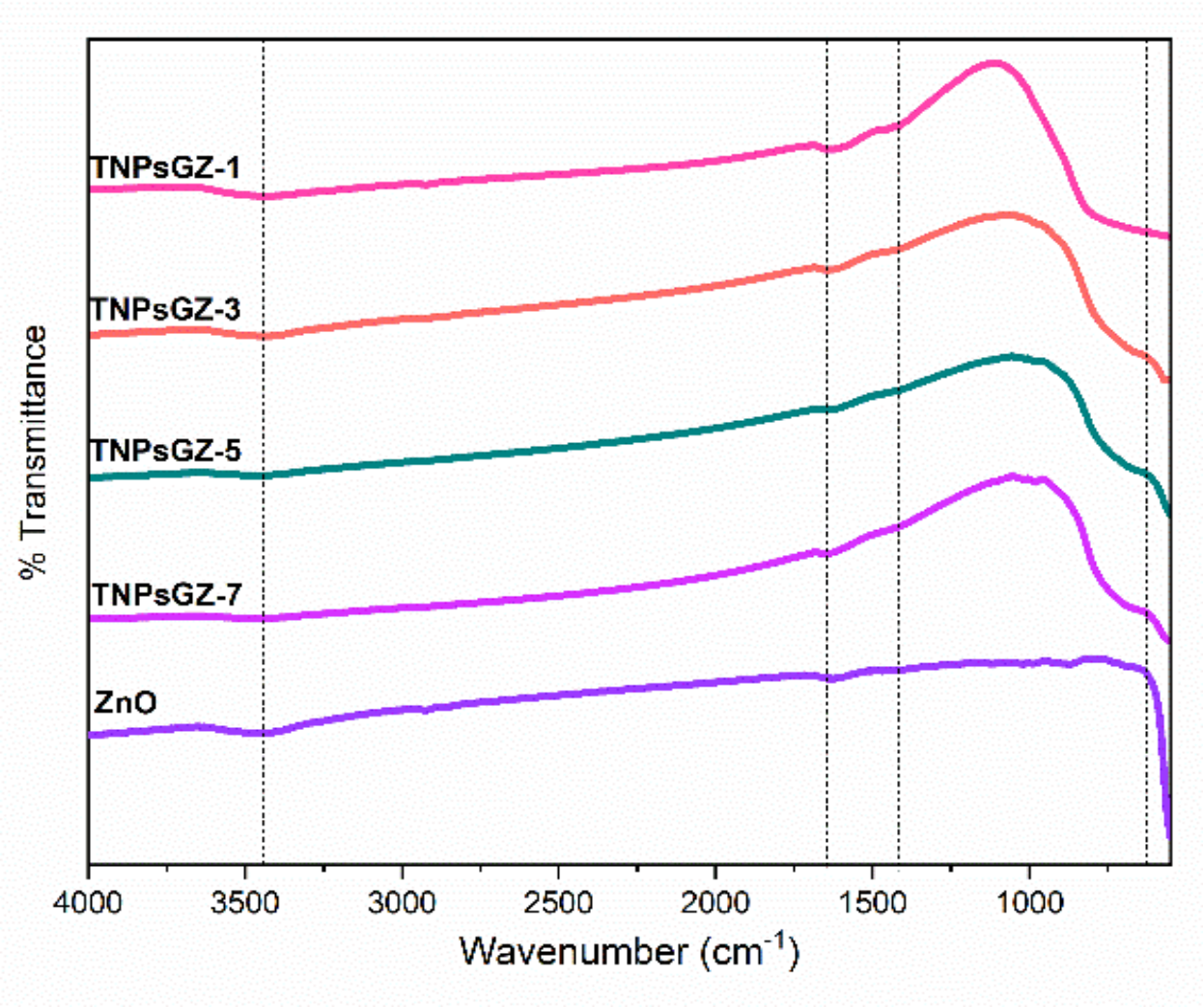

Figure 51 FTIR spectra of TNPsGZ based on the TG:ZnO ratios (1:1, 1:3, 1:5, 1:7) compare with ZnO

Table 11 FTIR peaks for TiO_2 identification in TNPsGZ composite

Wavenumber (cm^{-1})	Characteristic bond
3450	O-H stretching
1640	C=O stretching
1433	C-O stretching
778	Ti-O stretching
650 - 450	Ti-O-Ti bridging stretching

Table 12 FTIR peaks for GO identification in TNPsGZ composite

Wavenumber (cm^{-1})	Characteristic bond
1621	C=C stretching
1367	C-O stretching
1057	C–O–H vibration

Table 13 FTIR peaks for ZnO identification in TNPsGZ composite

Wavenumber (cm^{-1})	Characteristic bond
1626 and 1447	C=C stretching
1024, 827 and 778	Zn-O stretching

4.3.1.2 Raman spectroscopy

Raman spectra of TNPsGZ composite are shown in **Figure 52.** This figure provides a comprehensive overview of the results obtained from the composite, offering a detailed summary of the key findings and observations. The Raman spectra of the TNPsGZ composite peaks that correspond to TiO_2 as shown in **Figure 53.** A summary of the TiO_2 peak identifications is provided in **Table 14.** The Raman spectra of TiO_2 show Raman bands at 638, 515, 396, and 196 cm^{-1}, with a particularly sharp and intense peak observed at 143 cm^{-1}. The Raman-active modes can be identified through group-theoretical analysis of the anatase phase, which is associated with the space group $D4h^{19}$. The site symmetries for Ti and O atoms within the unit cell are proposed as D_{2d} for Ti and C_{2v} for O, leading to the following assignments: A_{1g} at 515 cm^{-1}, B_{1g} at 638 cm^{-1} and 396 cm^{-1}, and E_g at 143 cm^{-1} and 196 cm^{-1}. These Raman-active modes offer important insights into the vibrational characteristics and symmetry of the TiO_2 crystal structure. The prominent and well-defined peak at 143 cm^{-1} (E_g mode) is especially significant and is often recognized as a distinguishing feature of the anatase phase in TiO_2. (36) The appearance of this peak, together with other distinctive bands, verifies the successful synthesis of anatase TiO_2 nanoparticles, which aligns with the characteristics of TiO_2 within the composite.

The Raman spectra of the TNPsGZ composite peaks that correspond to GO as shown in **Figure 54.** A summary of the GO peak identifications is provided in **Table 15.** The Raman spectra of GO reveal two prominent peaks within the 1000-2000 cm^{-1} range, corresponding to the D and G bands. GO features a prominent G band mode, observed between 1500 and 1700 cm^{-1}, and a D band mode, appearing between 1250 and 1400 cm^{-1}, which in the composite aligns with graphene oxide, displaying peaks at approximately 1344 and 1684 cm^{-1}, respectively. (39)

The Raman spectra of the TNPsGZ composite peaks that correspond to ZnO as shown in **Figure 55.** A summary of the ZnO peak identifications is provided in **Table 16.** The crystalline structure of ZnO is defined by distinct bands at 333 cm^{-1} (second-order Raman processes, E_2-E_1 vibration modes), 437 cm^{-1} (E_2 high

vibration mode, associated with oxygen atoms), 98 cm^{-1} (E_2 low, associated with the Zn sublattice), 381 cm^{-1} (A_1), and 412 cm^{-1} (E_1). The two nonpolar phonon modes, E_{2L} and E_{2H}, which correspond to low and high frequencies, are linked to the vibrations of the heavy Zn sublattice and oxygen atoms, respectively. (77) Which, in the composite, corresponds with the properties of ZnO as outlined above.

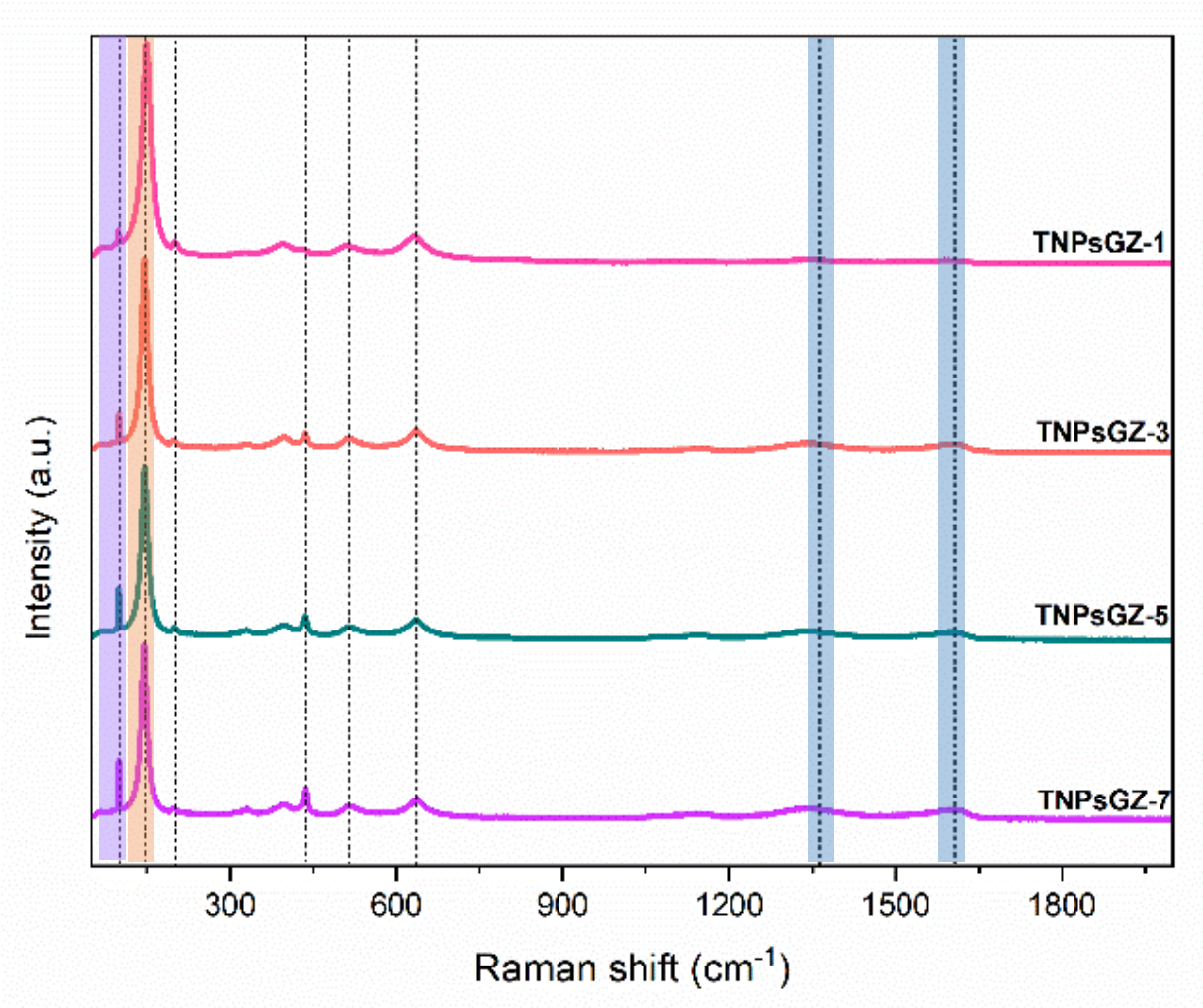

Figure 52 An overview of the Raman spectra of TNPsGZ composite based on the TG: ZnO ratios (1:1, 1:3, 1:5, 1:7) is provided to outline key functional groups and trends before comparing the materials individually.

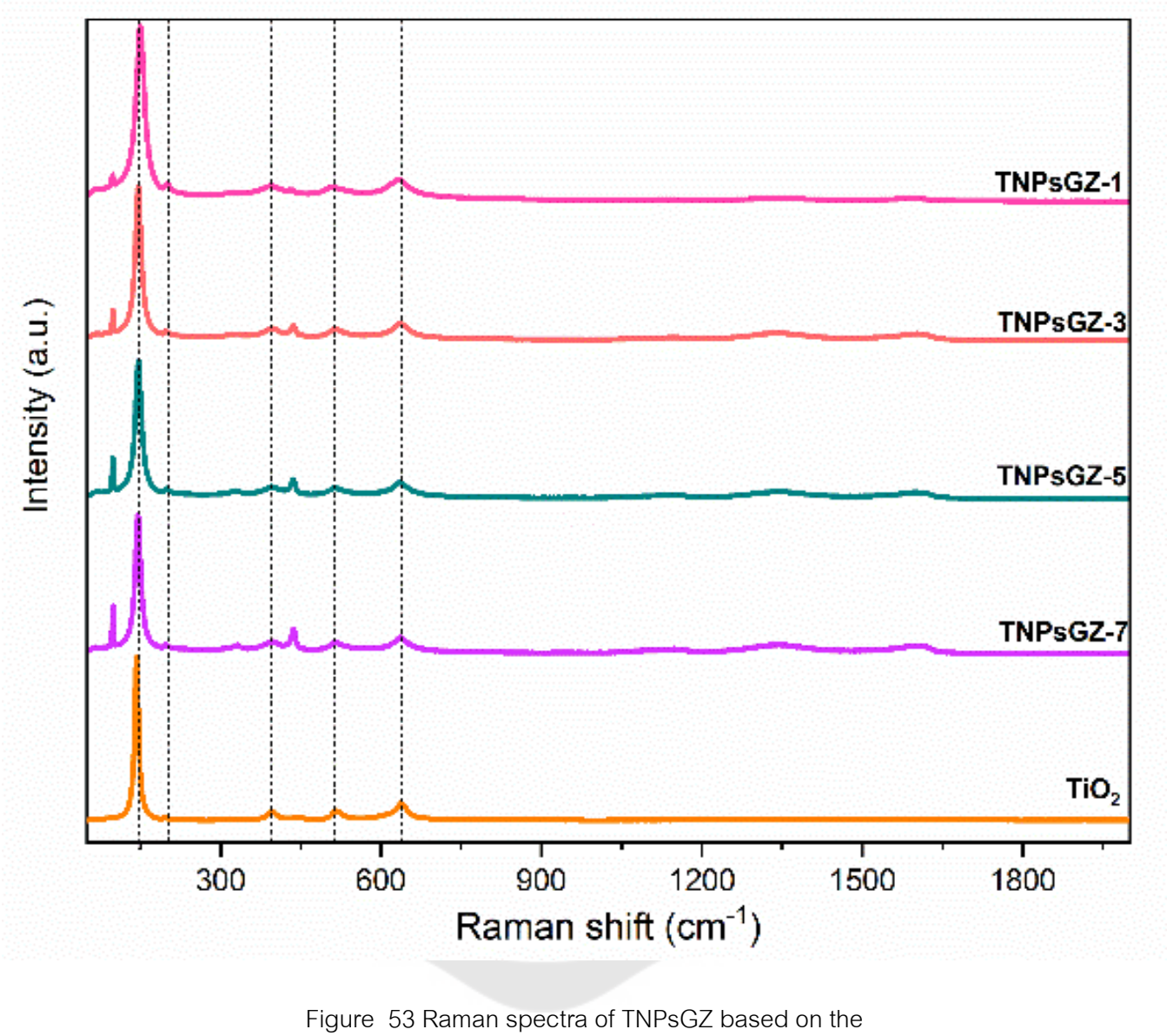

Figure 53 Raman spectra of TNPsGZ based on the TG: ZnO ratios (1:1, 1:3, 1:5, 1:7) compare with TiO_2

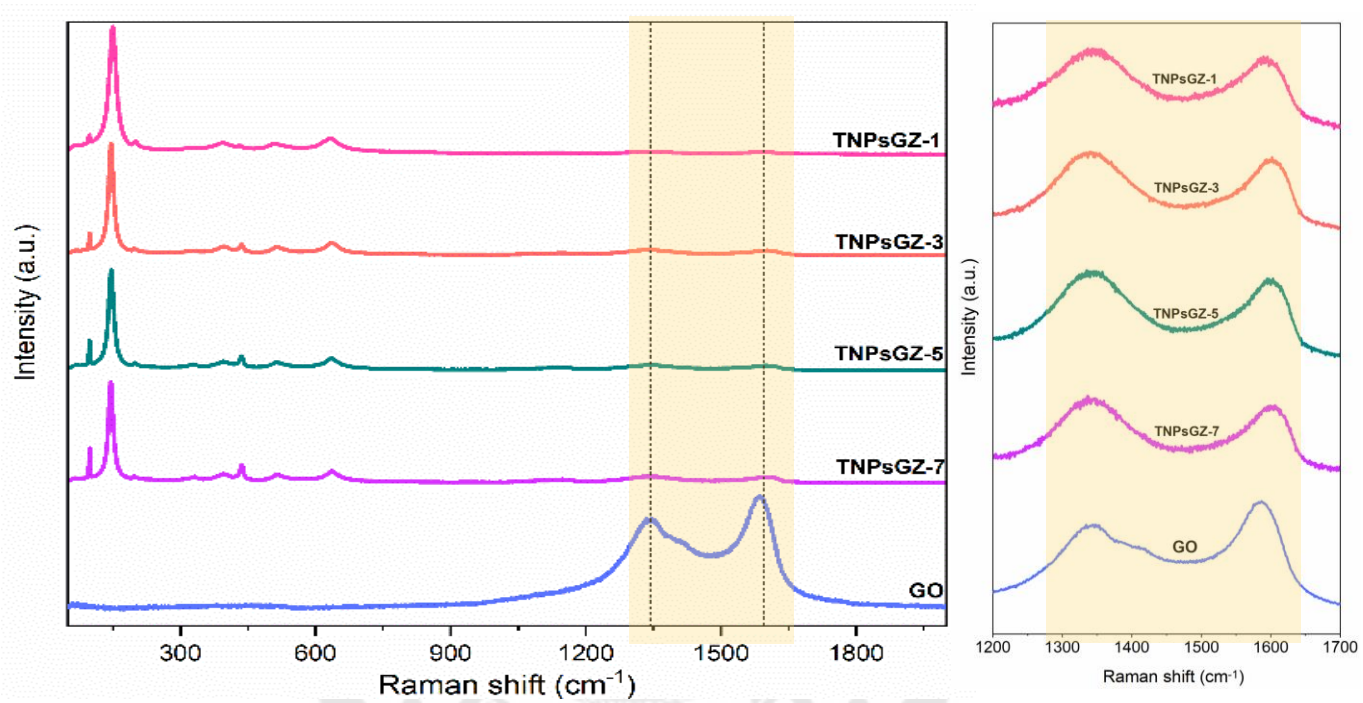

Figure 54 Raman spectra of TNPsGZ based on the TG: ZnO ratios (1:1, 1:3, 1:5, 1:7) compare with GO

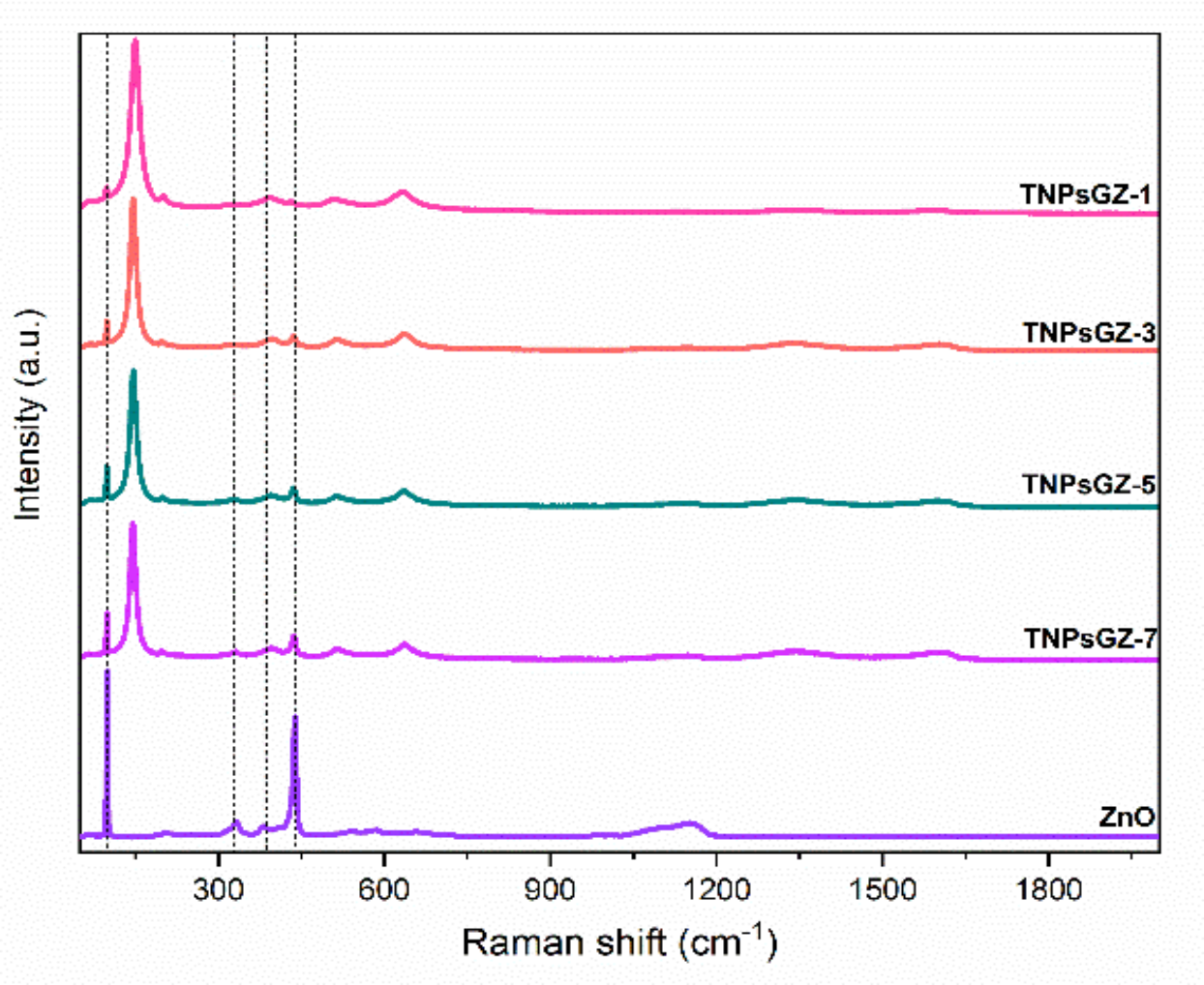

Figure 55 Raman spectra of TNPsGZ based on the TG: ZnO ratios (1:1, 1:3, 1:5, 1:7) compare with ZnO

Table 14 Raman peaks for TiO_2 identification in TNPsGZ composite

Wavenumber (cm^{-1})	Characteristic bond
638 and 396	B_{1g} mode
515	A_{1g} mode
196 and 143	E_g mode

Table 15 Raman peaks for GO identification in TNPsGZ composite

Wavenumber (cm^{-1})	Characteristic bond
1684	G Band
1344	D Band

Table 16 Raman peaks for ZnO identification in TNPsGZ composite

Wavenumber (cm^{-1})	Characteristic bond
437	E_2 high vibration mode
412	E_1 mode
381	A_1 mode
333	E_2-E_1 vibration mode
98	E_2 low vibration mode

4.3.1.3 X-ray Diffraction (XRD)

The XRD pattern of the TNPsGZ composite samples as shown in **Figure 56**. The prepared product exhibited several distinct diffraction peaks, each of which corresponded to characteristic TiO_2 peaks, closely matching the anatase phase (JCPDS-ICDD card: 21-1272) (30) and rutile phase (JCPDS-ICDD card: 21-1276). A summary of the TiO_2 peak identifications is provided in **Table 17**. The TNPsGZ composite samples reveal additional 2θ peaks at 25.3°, 27.5°, 36.9°, 53.8°, and 55.1°, corresponding to the crystalline planes of TiO_2 represented by (101), (110), (103), (105), and (211). The anatase phase, identified by its prominent peak at 25.3° (101), and the rutile phase, signified by the 2θ peaks at 27.5° (110), are both renowned for their distinct properties. (78) The 2θ peaks at 31.8°, 34.5°, 36.3°, 47.5°, 56.7°, and 62.9° are evident in the ZnO XRD pattern, corresponding to the (100), (002), (101), (102), (110), and (103) crystalline planes of ZnO, respectively, indicating a wurtzite structure (JCPDS No. 36-1451). A summary of the ZnO peak identifications is provided in **Table 18**.

The Debye calculated the crystallite sizes of the TNPsGZ composite samples–Scherrer method, with mean values of 42.00 nm for TNPsGZ-1 (**Table 19**), 42.36 nm for TNPsGZ-3 (**Table 20**), 42.44 nm for TNPsGZ-5 (**Table 21**), and 42.55 nm for TNPsGZ-7 (**Table 22**). In the TNPsGZ (TG: ZnO) composite with a 1:1 ratio, it can be observed that the 2θ peaks 25.3°, 27.5°, 36.9°, 53.8°, and 55.1° are more pronounced compared to those of other composite ratios, as this ratio contains the highest amount of TiO_2. It is evident that in other composite ratios, the TiO_2 peaks are barely visible, as the ZnO peaks exhibit higher intensity than TiO_2, varying according to the amount of ZnO used.

Furthermore, the relative intensity of the peaks suggests a strong interaction between the TiO_2 and ZnO phases within the composite. The pronounced peaks at 25.3° and 27.5° indicate a well-developed crystallinity in the TiO_2 structure, which is likely enhanced by the ZnO matrix. This interaction may contribute to stabilizing anatase and rutile phases, as evidenced by the clear separation of their characteristic peaks. Additionally, the presence of high-intensity ZnO peaks implies that the ZnO

phase dominates in composites with lower TiO_2 content, potentially influencing the overall photocatalytic properties of the material. This suggests that the ratio of TiO_2-GO to ZnO plays a crucial role in determining the crystalline structure and, consequently, the functional properties of the composite. The data in **Tables 19–22** show a slight and statistically insignificant increase in crystallite size, from 42.00 nm for TNPsGZ-1 to 42.55 nm for TNPsGZ-7, as the ZnO content increases. This minor trend likely does not reflect a significant impact of ZnO addition on crystallite growth.

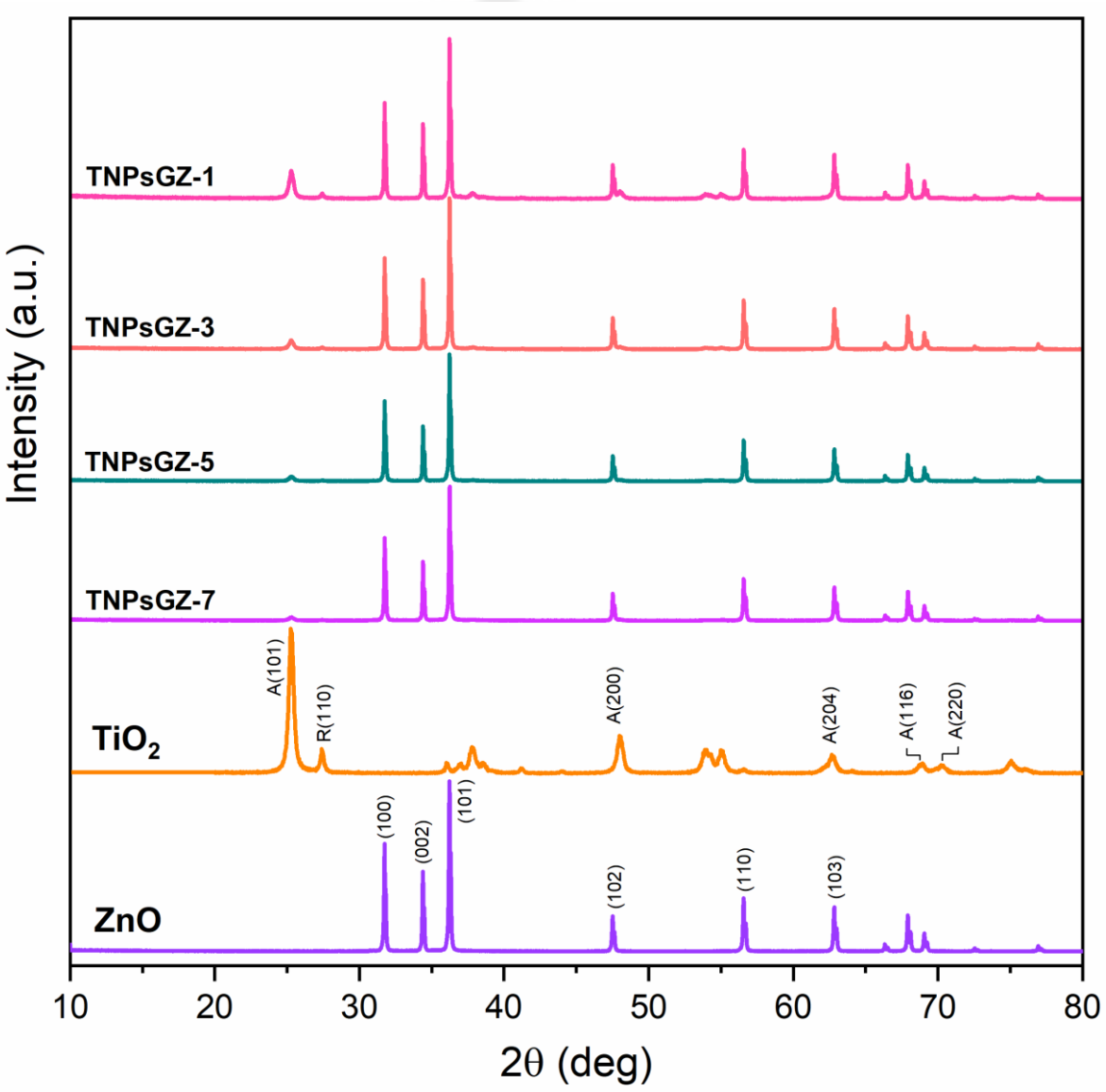

Figure 56 XRD patterns of TNPsGZ composite

Table 17 XRD peaks for TiO_2 identification in TNPsGZ composite

2θ (deg)	Crystalline plane
25.3	A(101)
27.5	R(110)
36.9	A(103)
53.8	A(105)
55.1	A(201)

Table 18 XRD peaks for ZnO identification in TNPsGZ composite

2θ (deg)	Crystalline plane
31.8	(100)
34.5	(002)
36.3	(101)
47.5	(102)
56.7	(110)
62.9	(103)

Table 19 Calculated crystallite sizes of the TNPsGZ-1 (Mean: 42.00 nm) by Debye–Scherrer method.

2θ	FWHM	Cos θ	Size (nm)
25.30	0.42	0.98	20.43
27.42	0.29	0.97	29.90
31.76	0.15	0.96	58.62
34.42	0.16	0.96	55.68
36.25	0.17	0.95	52.85
47.54	0.21	0.92	42.48
56.60	0.22	0.88	41.97
62.86	0.29	0.85	34.05
Crystalline size average			**42.00**

Table 20 Calculated crystallite sizes of the TNPsGZ-3 (Mean: 42.36 nm) by Debye–Scherrer method.

2θ	FWHM	Cos θ	Size (nm)
25.30	0.40	0.98	21.07
27.42	0.27	0.97	31.34
31.76	0.15	0.96	57.78
34.42	0.15	0.96	58.49
36.25	0.17	0.95	52.68
47.55	0.22	0.92	41.89
56.60	0.23	0.88	40.11
62.86	0.27	0.85	35.50
Crystalline size average			**42.36**

Table 21 Calculated crystallite sizes of the TNPsGZ-5 (Mean: 42.44 nm) by Debye–Scherrer method.

2θ	FWHM	Cos θ	Size (nm)
25.30	0.41	0.98	20.70
27.43	0.27	0.97	32.14
31.76	0.15	0.96	57.69
34.42	0.15	0.96	57.77
36.25	0.17	0.95	52.32
47.54	0.21	0.92	42.96
56.60	0.24	0.88	39.36
62.86	0.27	0.85	36.57
Crystalline size average			**42.44**

Table 22 Calculated crystallite sizes of the TNPsGZ-7 (Mean: 42.55 nm) by Debye–Scherrer method.

2θ	FWHM	Cos θ	Size (nm)
25.30	0.41	0.98	20.51
27.42	0.25	0.97	34.14
31.76	0.15	0.96	57.33
34.42	0.15	0.96	57.40
36.25	0.17	0.95	51.91
47.54	0.21	0.92	43.87
56.60	0.24	0.88	39.80
62.86	0.27	0.85	35.44
Crystalline size average			**42.55**

4.3.1.4 Field Emission Scanning electron microscope (FE-SEM)

The surface morphology of the nanoparticles of TNPsGZ as shown in Figures 57-64. The FE-SEM image of the TNPsGZ composite (TG: ZnO) with a 1:1 ratio, as shown in **Figure 57**, revealed nano-sized TiO_2 grains with a substantial surface area and well-defined mesopores and uniform particle dispersion. The morphology analysis of TiO_2 showed particles with a size of around 10 to 40 nm. In morphology analysis of ZnO confirmed a hexagonal structure. The uniform distribution of particles in this ratio indicates effective interaction between TiO_2 and ZnO. The homogeneous integration of TiO_2 and ZnO within this composite demonstrates a strong interaction between the two materials, ensuring consistency and uniformity throughout the structure. In contrast, in **Figures 59, 61, and 63**, as the ZnO content increases in the 1:3, 1:5, and 1:7 ratios, noticeable particle agglomeration occurs, leading to a thicker composite layer. This aggregation could influence the mechanical and functional properties of the material. Furthermore, the EDS analysis in **Figure 58**, for the 1: 1 ratio confirmed that the composite consists of carbon (40 wt% , 62.5 at.%), oxygen (21.7 wt% , 25.5at%), zinc (28.1 wt% , 8.1at%), and titanium (10.2 wt% , 3.9at%), which verifies the successful incorporation of TiO_2, ZnO, and GO into the composite matrix. Additionally, the EDS results for other TG: ZnO ratios further support these findings. In **Figure 60** (for the 1:3 ratio), the composite composition was measured to be approximately carbon (39.2 wt%, 62.57at%), oxygen (20.4 wt% 24.44 at%), zinc (29.7 wt%, 8.71 at%), and titanium (10.7 wt%, 4.28 at%), indicating similar incorporation of the materials with a slight increase in zinc content due to the higher ZnO ratio. **Figure 62** (for the 1:5 ratio) showed a composition of carbon (38.5 wt%, 62.5%), oxygen (19.9 wt%, 24.1 at%), zinc (31.3 wt%, 9.3 at%), and titanium (10.3 wt% , 4.1 at%), further demonstrating that as the ZnO ratio increases, the zinc content in the composite rises proportionally. **Figure 64** (for the 1:7 ratio), the composite consisted of carbon (37.8 wt%, 62.3 at%), oxygen (19.5 wt%, 23.8 at%), zinc (32.1 wt% , 9.8 at%), and titanium (10.6 wt% , 4.1 at%), confirming a steady integration of ZnO and TiO_2 in higher ZnO ratios.

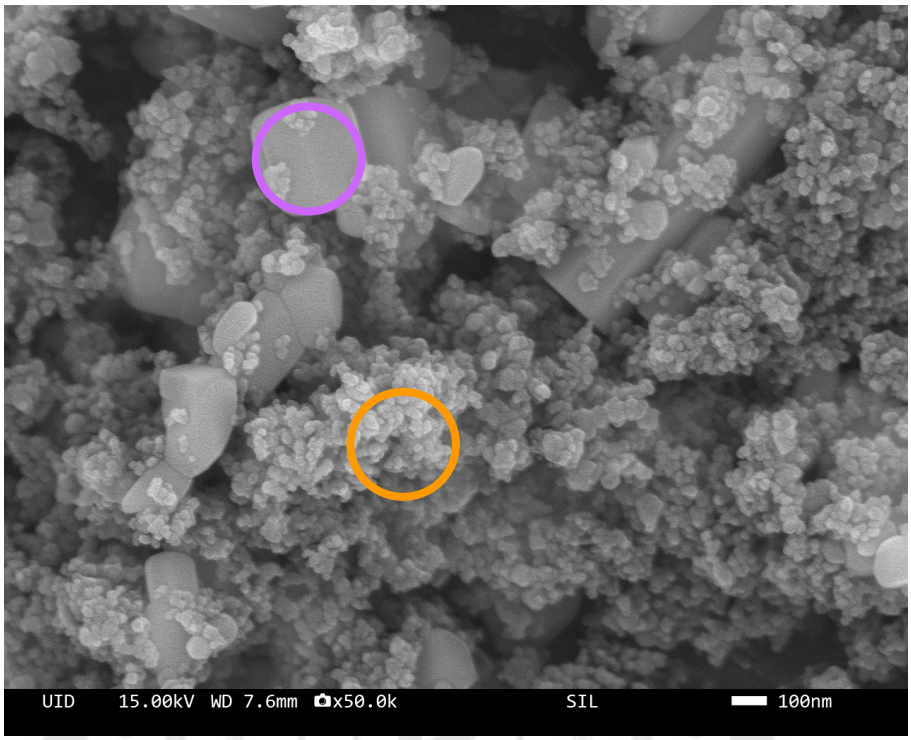

Figure 57 FE-SEM image of TNPsGZ based on the TG: ZnO ratios 1 : 1

The orange circle indicates TiO_2, while the purple circle represents ZnO.

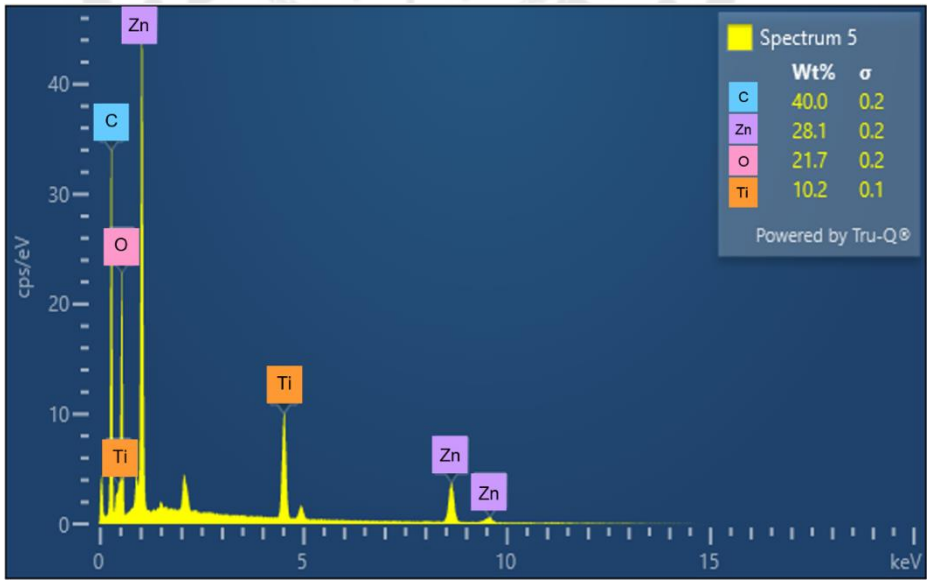

Figure 58 EDS image of TNPsGZ based on the TG: ZnO ratios 1 : 1

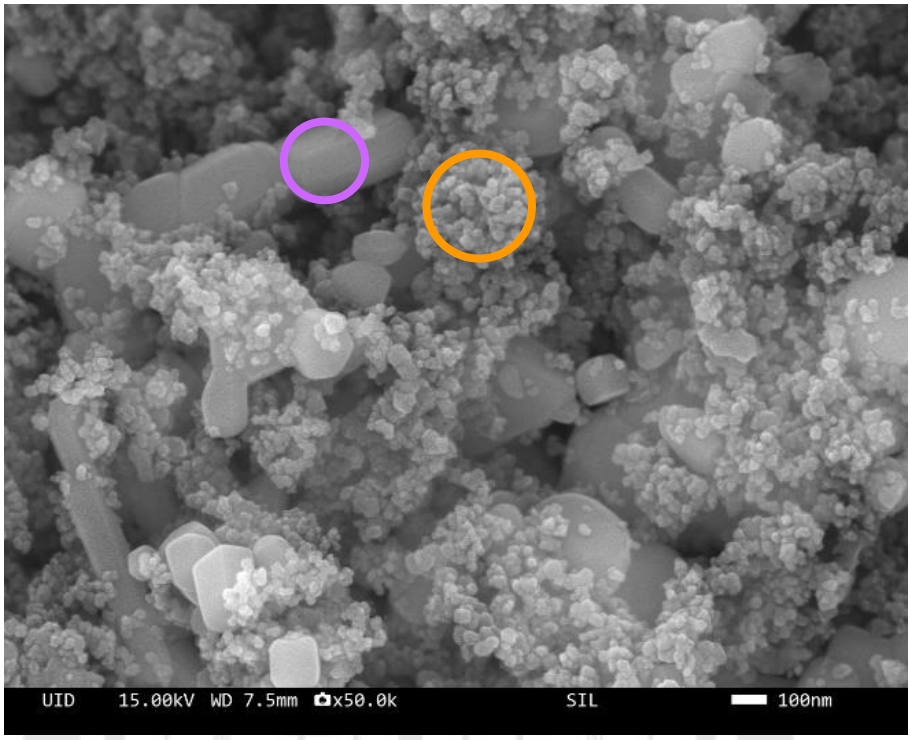

Figure 59 FE-SEM image of TNPsGZ based on the TG: ZnO ratios 1 : 3

The orange circle indicates TiO_2, while the purple circle represents ZnO.

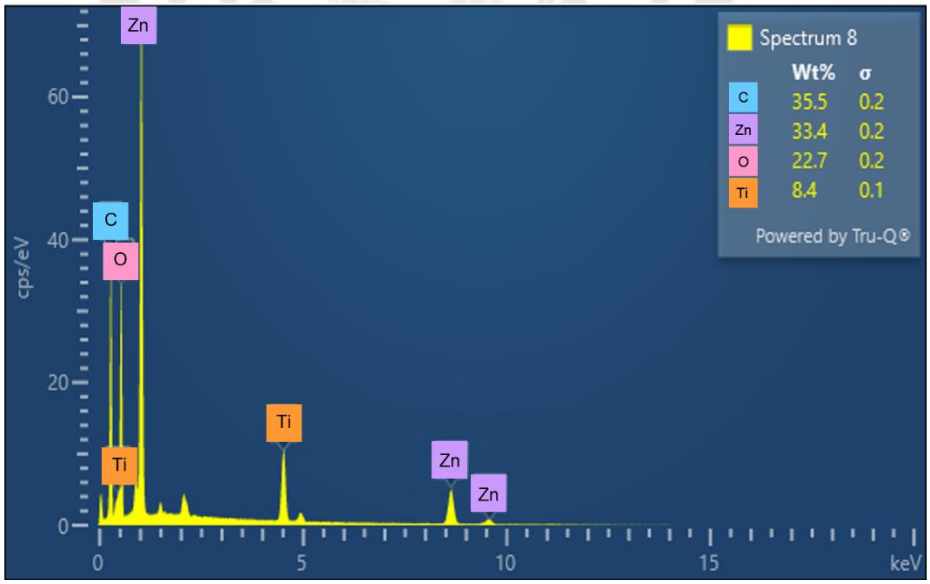

Figure 60 EDS image of TNPsGZ based on the TG: ZnO ratios 1 : 3

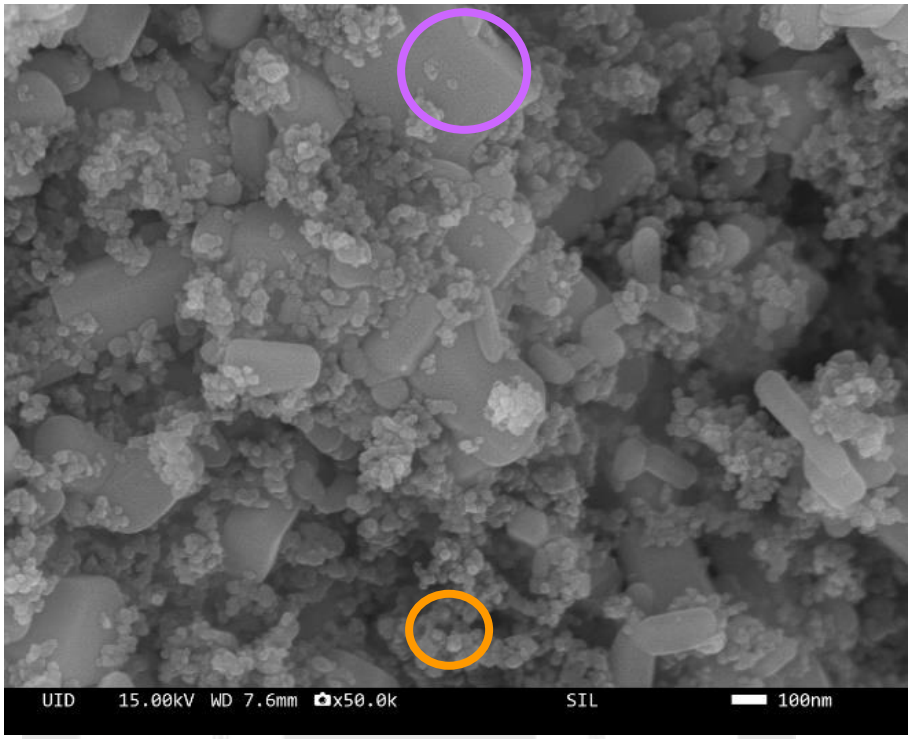

Figure 61 FE-SEM image of TNPsGZ based on the TG: ZnO ratios 1: 5

The orange circle indicates TiO_2, while the purple circle represents ZnO.

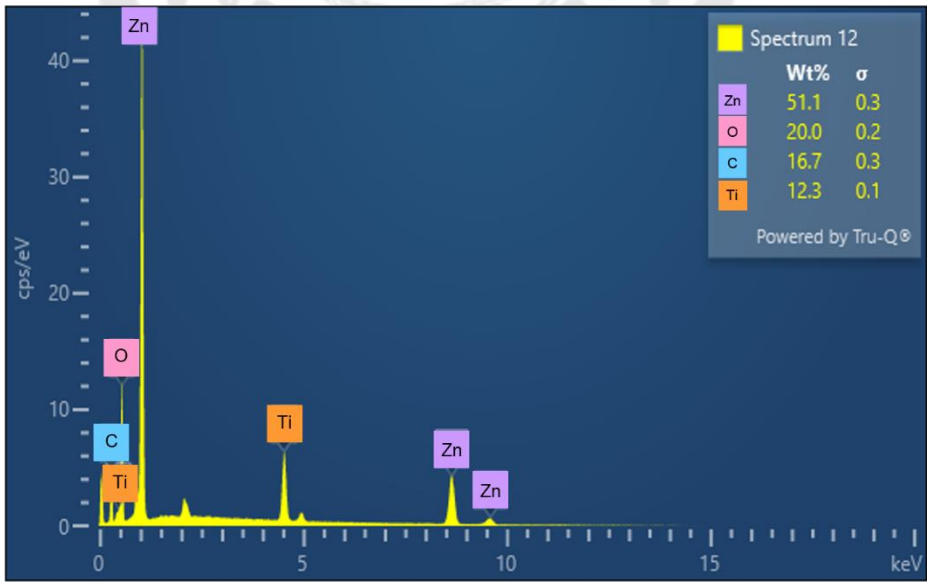

Figure 62 EDS image of TNPsGZ based on the TG: ZnO ratios 1 : 5

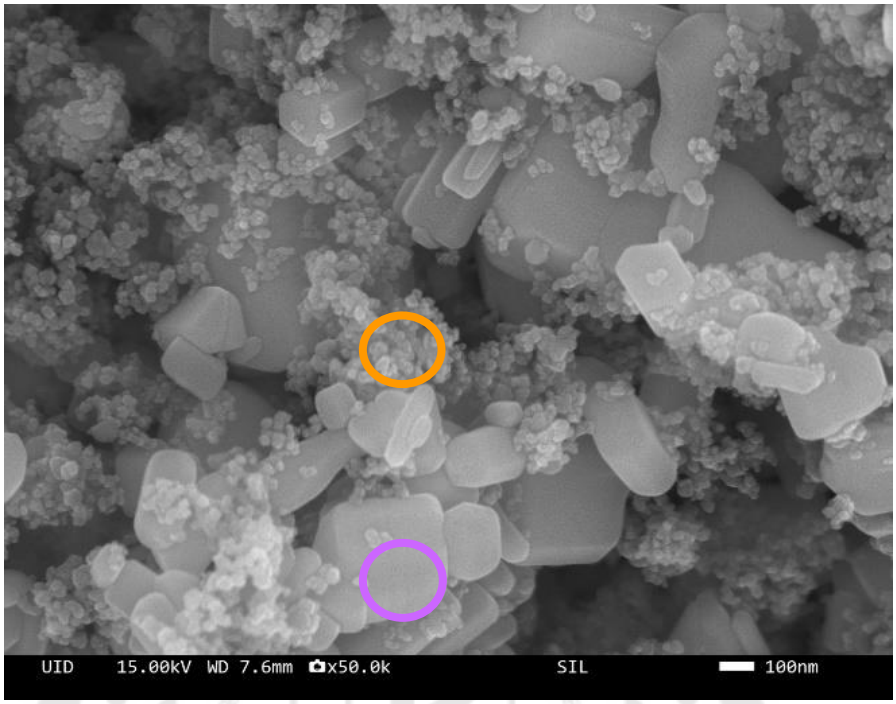

Figure 63 FE-SEM image of TNPsGZ based on the TG: ZnO ratios 1 : 7

The orange circle indicates TiO_2, while the purple circle represents ZnO.

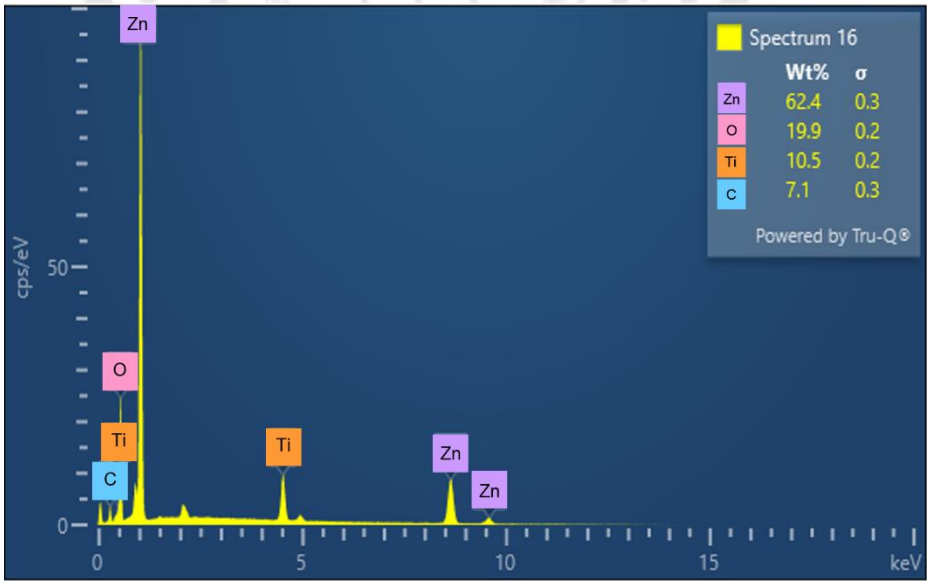

Figure 64 EDS image of TNPsGZ based on the TG: ZnO ratios 1 : 7

4.3.2 Characterization of cotton fabric coated with TNPsGZ composite

The characterization of TNPsGZ-coated cotton fabrics aimed to evaluate the morphology and chemical composition of fabrics coated with composites at different TG: ZnO ratios. Techniques such as Scanning Electron Microscopy (SEM) and energy-dispersive X-ray Spectroscopy (EDS) were utilized to analyze the surface structure and elemental composition.

4.3.2.1 Fabric Appearance

The comparison between the untreated cotton fabric (**Figure 41**) and cotton fabric coated with TNPsGZ, TiO_2/PVP, and ZnO/PVP reveals that, after the curing process, as shown in **Figure 65**, the coated samples retained the original white color of the fabric without significant visible changes, indicating that the coating materials preserved the aesthetic properties of the cotton; under 500x magnification, the TNPsGZ coating demonstrated a uniform distribution across the fiber surface and effectively penetrated the inter-yarn spaces, while the TiO_2/PVP and ZnO/PVP coatings exhibited similar surface coverage, with ZnO/PVP showing a denser coating layer, suggesting variations in coating characteristics that may influence the physical and chemical properties of the fabric in subsequent applications.

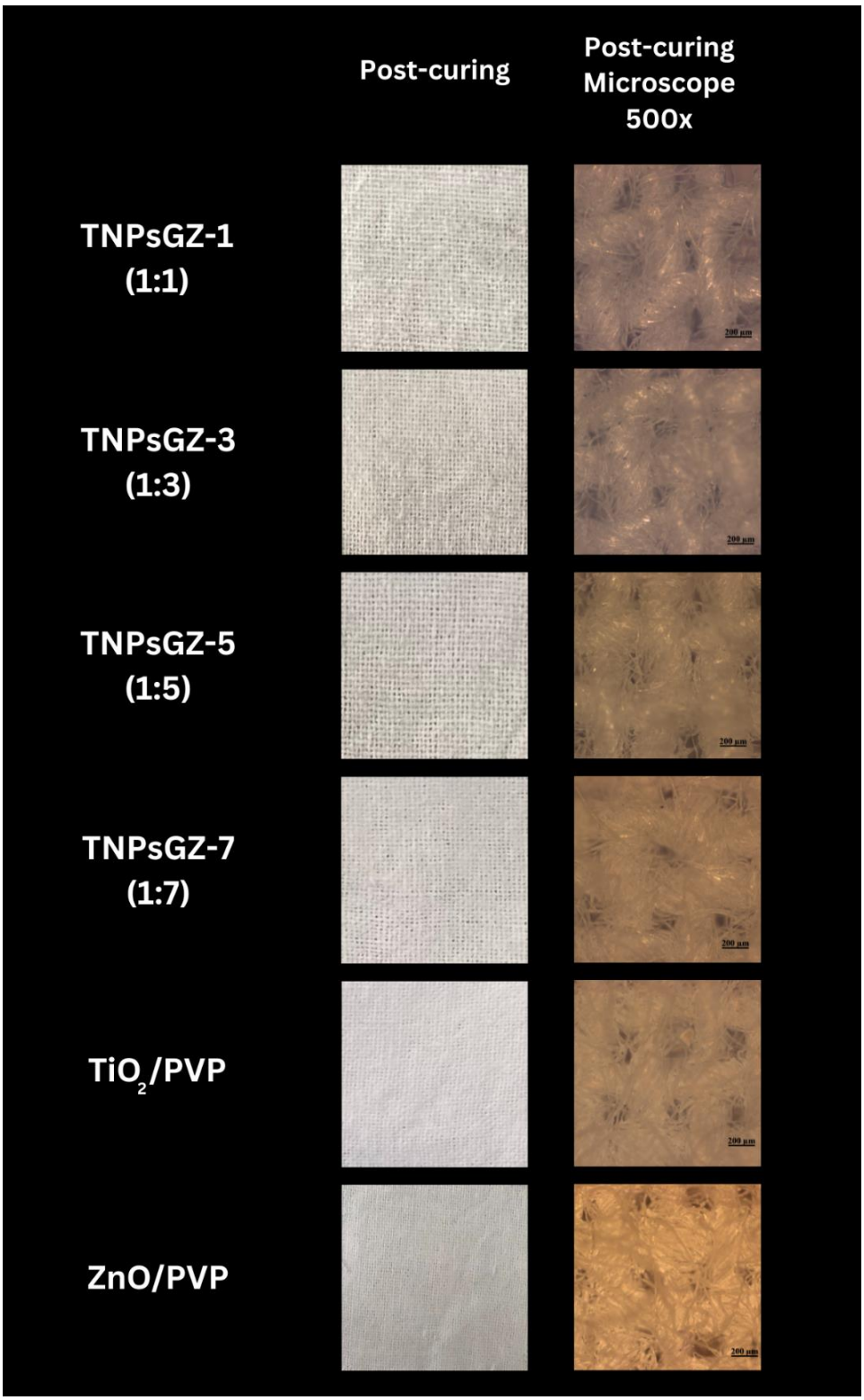

Figure 65 Appearances of cotton fabric coated with TNPsGZ in varying TG: ZnO ratios (1:1, 1:3, 1:5, and 1:7), showing the post-curing and detailed surface morphology observed under an optical microscope at 500x magnification.

4.3.2.2 Fourier transform infrared (FTIR)

The FTIR spectra for Cotton fabric with TNPsGZ composite as shown in **Figure 66**, exhibit significant differences when compared to uncoated cotton fabric. The uncoated cotton fabric primarily shows peaks related to the cellulose structure, including the characteristic O-H stretching vibration around 3330 cm^{-1} and C-H stretching vibrations between 2900 cm^{-1} and 2840 cm^{-1}. These peaks indicate the presence of hydroxyl groups and aliphatic hydrocarbons, which are typical for natural cotton fibers.(79) Moreover, peaks observed in the TNPsGZ/PVP, the peak observed at 1649 cm^{-1}, representing the stretching of carbonyl (C= O) groups, is characteristic of pure PVP and confirms its successful incorporation into the composite matrix. Additionally, the –C–N stretching vibrations and –C–H bending vibrations of the PVP polymer were observed at 1422 and 1280 cm^{-1}, respectively, providing further confirmation of PVP's presence in the composite material. (72) For TiO_2, the absorption band at 450–800 cm^{-1} corresponds to Ti–O–Ti stretching vibrations, confirming its incorporation into the PVP matrix. For ZnO, characteristic peaks such as C=O stretching (1,646 cm^{-1}), O-H stretching (3,407 cm^{-1}), and Zn–O stretching (~450–500 cm^{-1}) highlight strong interactions between ZnO and PVP. The presence of this peak suggests that PVP plays a crucial role in enhancing the stability and interaction between the composite components, contributing to better overall dispersion and adhesion to the cotton fabric. The inclusion of PVP in the composite not only results in an increase in the intensity of specific peaks but also enhances the uniformity and distribution of the coating on the fabric. This improvement is likely due to the polymer's ability to act as a stabilizer, preventing agglomeration of nanoparticles and ensuring a more consistent coating.

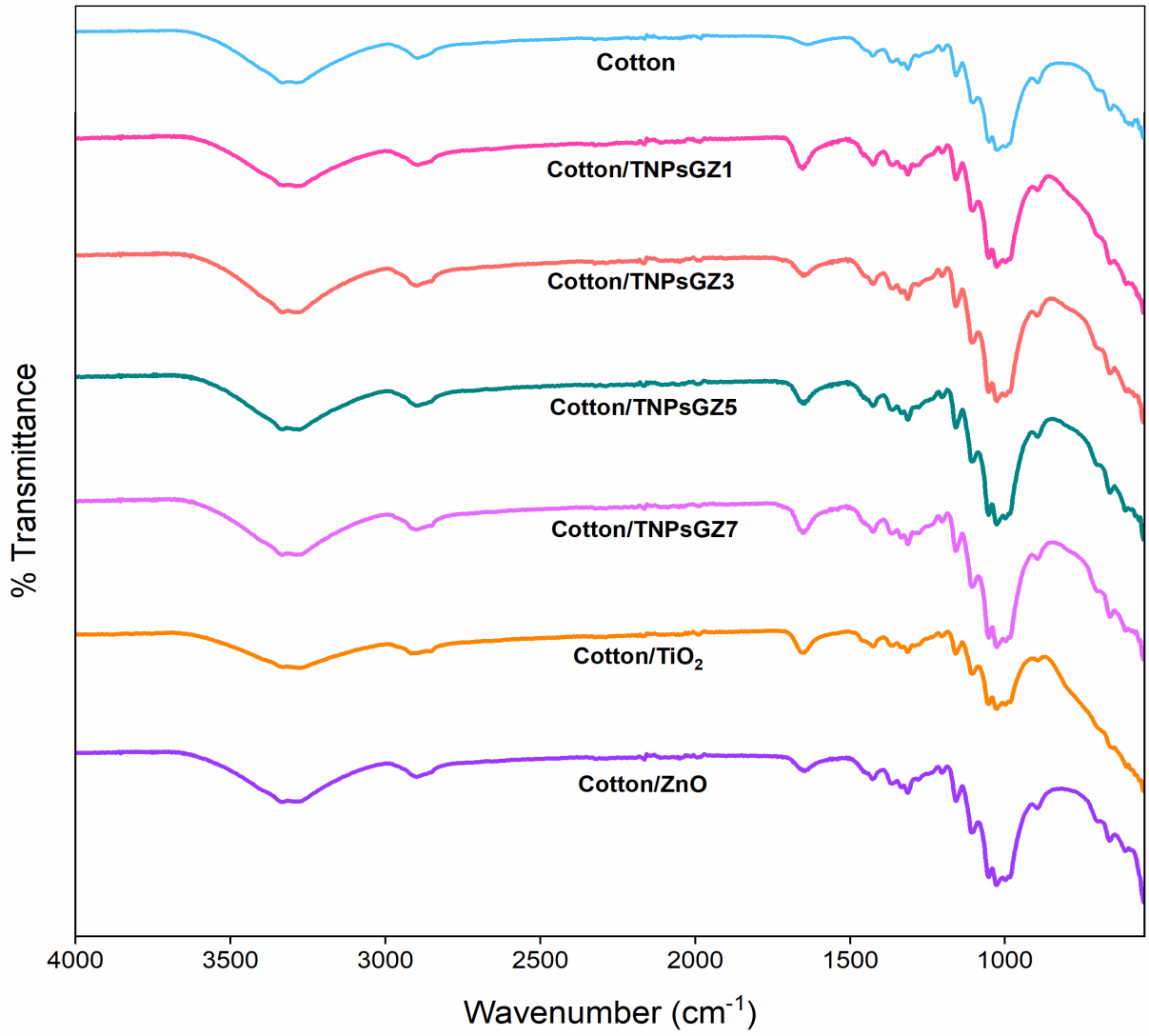

Figure 66 FTIR spectra of cotton fabric coated with TNPsGZ composite and Control (TiO_2 and ZnO)

4.3.2.3 Scanning electron microscope (SEM)

The morphology of the cotton fabric coated with TNPsGZ composite was investigated by SEM as shown in Figures 67 to 73. These images show notable differences compared to the uncoated cotton fabric (**Figure 67**), revealing a clear difference in particle distribution depending on the TG: ZnO ratio. In the sample with a 1:1 ratio (**Figure 68**), the particles were well-dispersed, covering the surface of the cotton fabric uniformly. This even distribution is indicative of a strong interaction between the TiO_2, ZnO, and GO components, leading to an optimal coating on the fabric. As the ZnO ratio increases (**Figures 69 to 71**), the SEM images show noticeable agglomeration of particles, particularly in the 1:3, 1:5 and 1:7 ratios. This clumping may result from the excess ZnO in the composite, which reduces the homogeneity of the coating. The aggregation could potentially impact the functional properties of the material, as uneven particle distribution might hinder the composite's effectiveness in areas like hydrophobicity. In comparison with control samples, the TiO_2-coated fabric (**Figure 72**) exhibited visible particle clumping and breakage, which could explain its lower performance in some applications. On the other hand, the ZnO-coated fabric (**Figure 73**) demonstrated a more uniform particle distribution, like the TNPsGZ 1:1 ratio sample, further supporting the idea that the balanced incorporation of ZnO in the composite plays a key role in enhancing the coating quality.

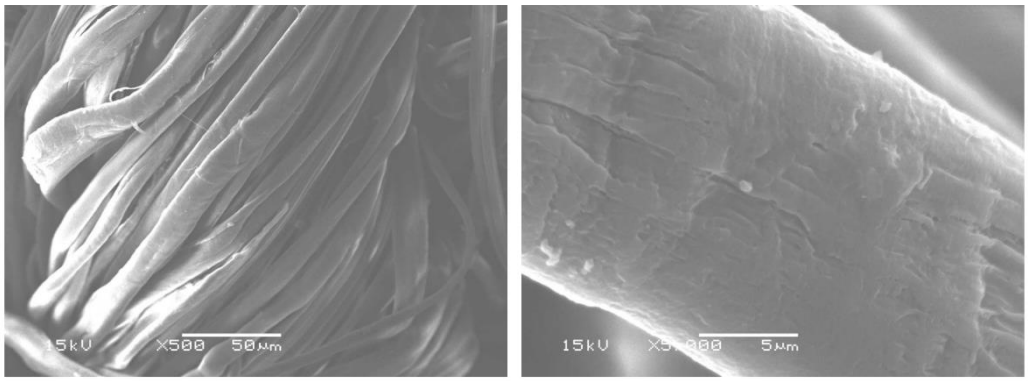

a. b.

Figure 67 SEM image of cotton fabric (a) 500X (b) 5000X

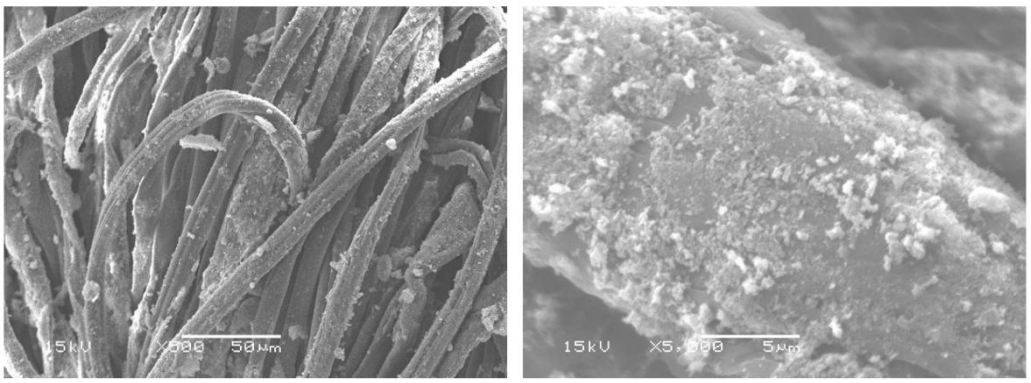

a. b.

Figure 68 SEM image of cotton fabric coated with TNPsGZ (TG: ZnO ratios 1 : 1)

(a) 500X (b) 5000X

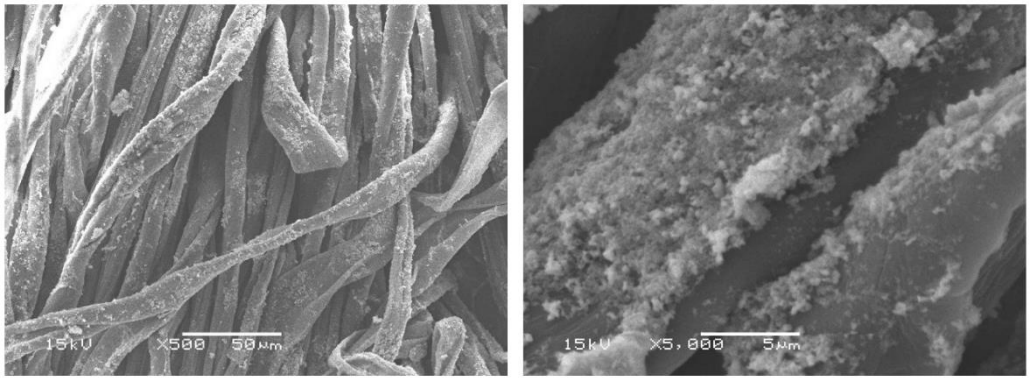

a. b.

Figure 69 SEM image of cotton fabric coated with TNPsGZ (TG: ZnO ratios 1 : 3)

(a) 500X (b) 5000X

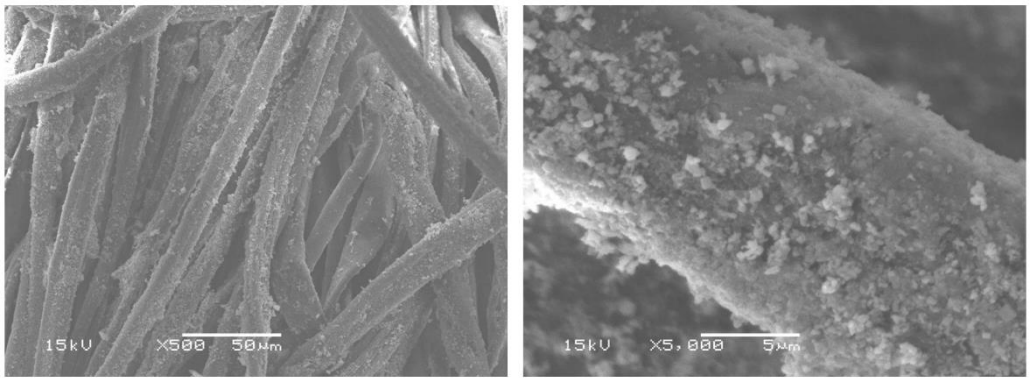

a. b.

Figure 70 SEM image of cotton fabric coated with TNPsGZ (TG: ZnO ratios 1 : 5)

(a) 500X (b) 5000X

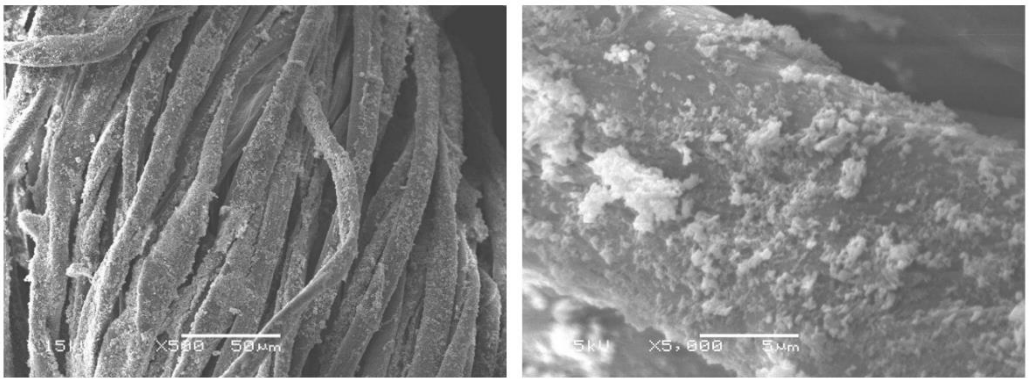

a. b.

Figure 71 SEM image of cotton fabric coated with TNPsGZ (TG: ZnO ratios 1 : 7)

(a) 500X (b) 5000X

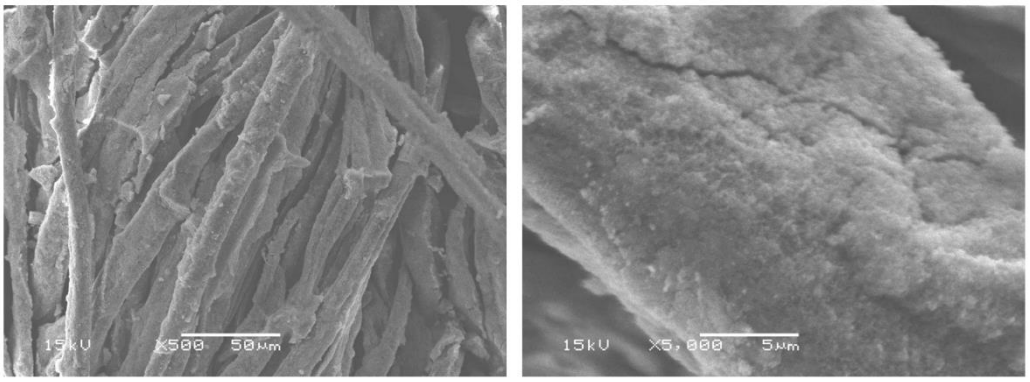

a. b.

Figure 72 SEM image of cotton fabric coated with TiO_2 composite (a) 500X (b) 5000X

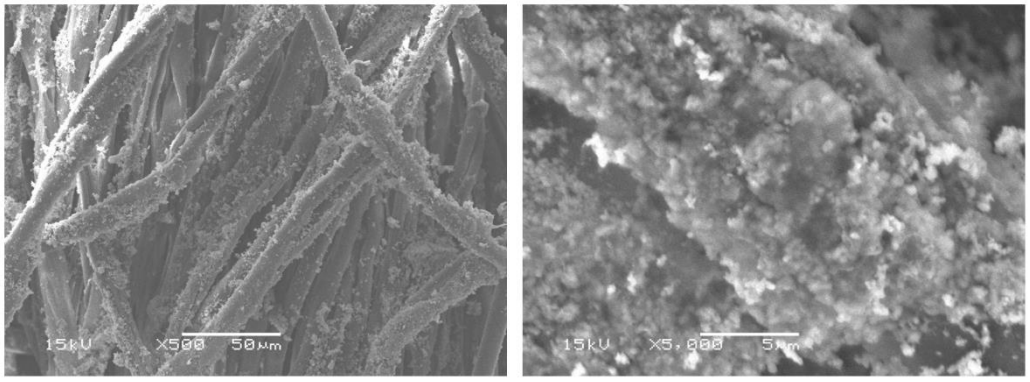

a. b.

Figure 73 SEM image of cotton fabric coated with ZnO composite (a) 500X (b) 5000X

The SEM image of the cotton fabric coated with the TNPsGZ composite (TG: ZnO ratio 1:1), coupled with EDS mapping as shown in **Figures 74, 75, and 76** provides valuable insights into the distribution and concentration of elements within the composite. The EDS mapping highlights the uniform dispersion of key elements carbon (C), oxygen (O), titanium (Ti), and zinc (Zn) across the fabric surface, which corroborates the observations from the SEM analysis discussed earlier. Specifically, the EDS analysis revealed that the composite consists of approximately 21.61 wt% carbon, 34.29 wt% oxygen, 21.27 wt% titanium, and 22.83 wt% zinc. The even distribution of titanium and zinc, accounting for 21.27 wt% and 22.83 wt% , respectively, is particularly noteworthy, as shown in **Table 23**. These two elements, derived from TiO_2 and ZnO, are critical to the composite's functionality. The uniform dispersion of TiO_2 particles contributes to the enhancement of UV protection. In contrast, the ZnO particles, well-distributed across the fabric, play a significant role in both UV-blocking and water-repelling properties. This even distribution of Zn and Ti ensures that the fabric maintains consistent performance across its surface, avoiding weak spots that could compromise its protective qualities. Additionally, the carbon mapping, which accounts for 21.61 wt% of the composite, indicates the presence of GO within the matrix, further supporting the structural integrity of the coating. GO's presence enhances the mechanical strength and improves the interaction between TiO_2 and ZnO, facilitating better adhesion of the composite to the cotton fibers. The oxygen content, at 34.29 wt%, reflects the involvement of both TiO_2 and ZnO, along with the hydroxyl groups present in GO, creating a well-integrated composite matrix.

The overall uniformity in the distribution of these elements, as demonstrated by the EDS data, confirms the successful incorporation of the TNPsGZ composite onto the cotton fabric. This homogeneity is crucial for ensuring the composite's functional properties, such as UV protection and hydrophobicity, remain effective throughout the material. The balanced TG: ZnO ratio of 1:1 offers an optimal integration of the materials, allowing for enhanced interaction between the nanoparticles and providing a stable, consistent coating. (28–30)

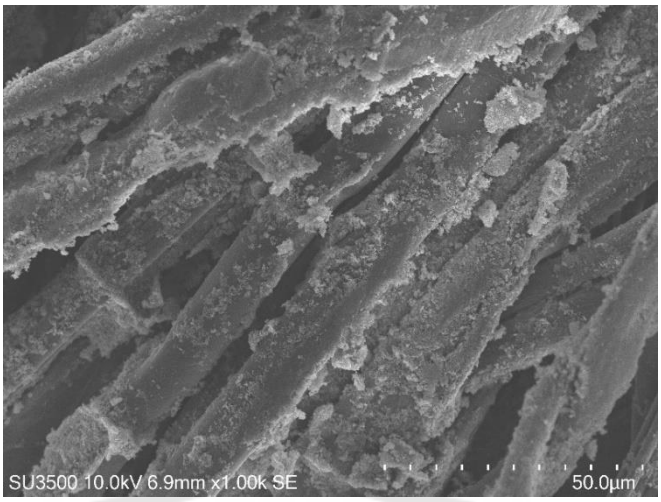

Figure 74 SEM image of cotton fabric coated with TNPsGZ (TG: ZnO ratios 1 : 1)

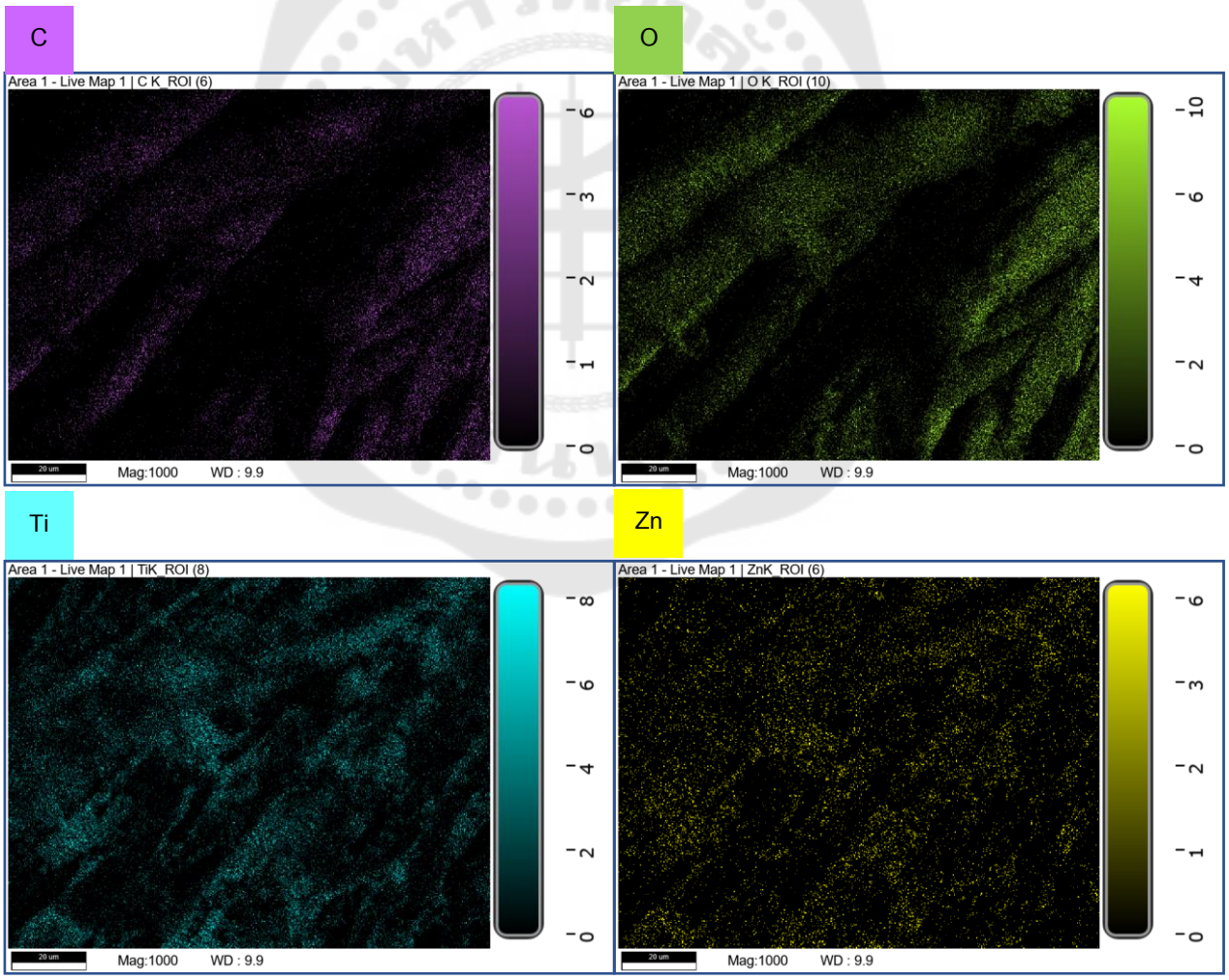

Figure 75 Elemental mapping image of cotton fabric coated with TNPsGZ

(TG: ZnO ratios 1 : 1)

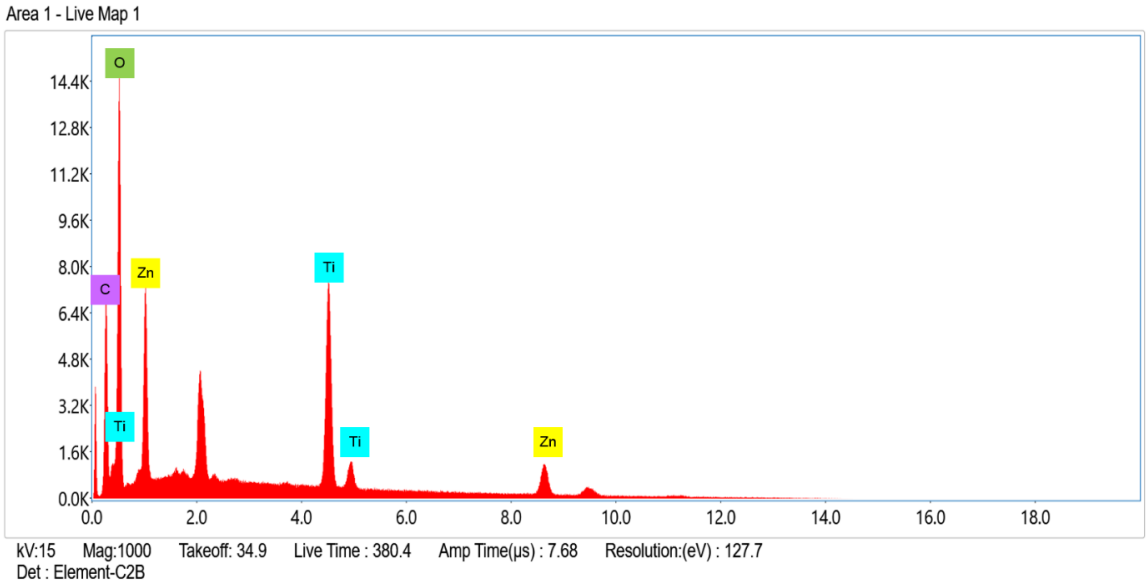

Figure 76 EDX spectra image of cotton fabric coated with TNPsGZ (TG: ZnO ratios 1 : 1)

Table 23 EDX spectra of cotton fabric coated with TNPsGZ (TG: ZnO ratios 1 : 1)

Element	Weight %	Atomic %
C K	21.61	37.99
O K	34.29	45.26
Ti K	21.27	9.38
Zn K	22.83	7.38

4.3.3 Properties of cotton fabric coated with TNPsGZ composite

4.3.3.1 Hydrophobic property

From **Figures 77 and 78**, obviously, the angles are just slightly different; the best result of the research is the cotton fabric coated with TNPsGZ-1 based on a ratio of 1:1 with an average angle of 129°. The coated fabric exhibits hydrophobic properties (>90°), which is comparable to samples like TiO_2 and ZnO, both of which are considered to be reasonably valuable for both examples. However, when measuring angles with TiO_2, it was unable to find a specific angle value due to the rapid permeation of water. In the case of ZnO, although angles can be measured, they are less valuable compared to the best results and tend to be hydrophilic. Based on the SEM results shown in **Figure 69**, the findings remain consistent, as the particles exhibit uniform distribution.

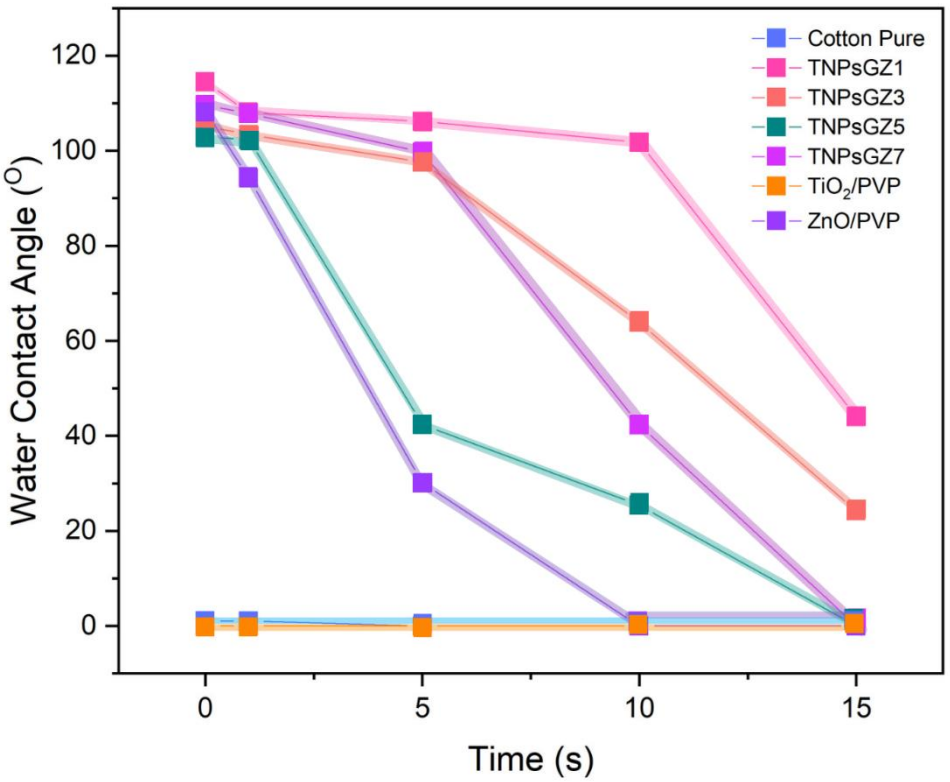

Figure 77 Water contact angle as a function of time for pure cotton fabric, TNPsGZ-coated samples with varying TG: ZnO ratios (1:1, 1:3, 1:5, and 1:7), and control samples coated with TiO_2/PVP and ZnO/PVP.

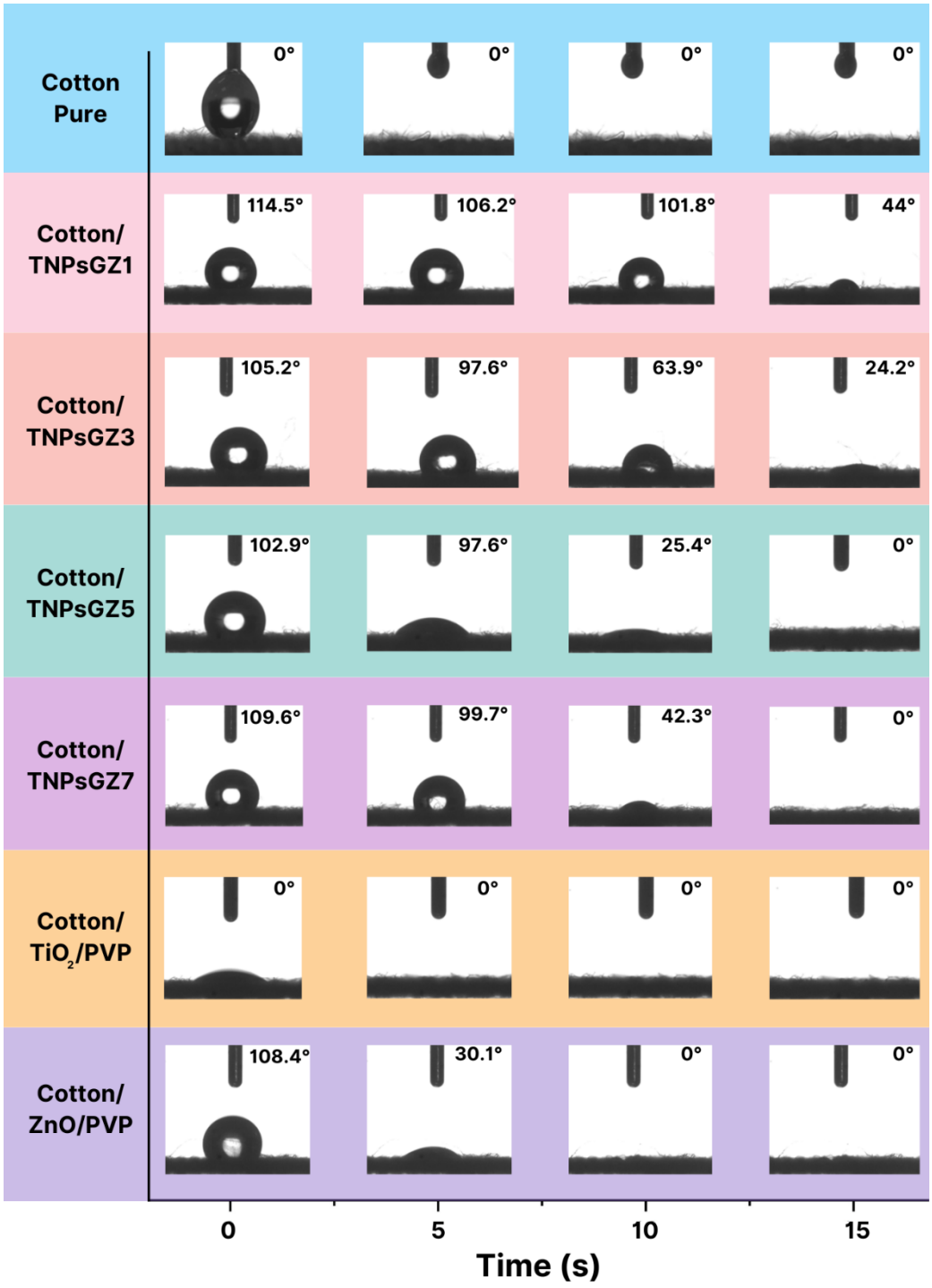

Figure 78 The water contact angles were measured at short time intervals (0, 5, 10, and 15 seconds) to observe the immediate behavior of water droplets on the surface and evaluate the hydrophobic performance of the TNPsGZ composite coating compared to uncoated cotton fabric and control samples with TiO_2 and ZnO coatings.

The optimal ratio of ZnO ensures proper dispersion. Conversely, the observed particle clumping and breakage in TiO_2 samples suggest a potential factor contributing to rapid water permeation.

In addition to the initial observations, the hydrophobic properties of the TNPsGZ-coated cotton fabric were further analyzed by comparing the water contact angles of different samples. The cotton fabric coated with a TNPsGZ-1 (TG: ZnO) ratio of 1:1 exhibited the highest water contact angle, averaging 129°. This significant angle demonstrates that the fabric surface is strongly hydrophobic, as a contact angle greater than 90° is indicative of hydrophobicity. In comparison to control samples, the TiO_2-coated fabric was unable to retain water droplets for contact angle measurement due to rapid water permeation, suggesting a highly hydrophilic nature. Conversely, the ZnO-coated fabric, while allowing for contact angle measurement, displayed lower values compared to the TNPsGZ-1-coated fabric, indicating less hydrophobicity and a tendency towards hydrophilicity.

This behavior correlates well with the SEM analysis, where the uniform distribution of ZnO particles at the optimal 1:1 ratio in the TNPsGZ composite contributes to enhanced hydrophobic properties. In contrast, the observed agglomeration and particle breakage in TiO_2 samples may explain the rapid water permeation and the lack of measurable hydrophobicity. Therefore, the TNPsGZ-1 composite with a (TG:ZnO) ratio of 1:1 proves to be the most effective in imparting strong hydrophobic properties to the cotton fabric, making it suitable for applications requiring water-resistant textiles.

4.3.3.2 UV-Protection property

The cotton fabric coated with TNPsGZ composite demonstrated excellent UV protection properties, as evidenced by the results of the UV-blocking tests, as shown in **Table 24**. The samples, particularly those coated with a TNPsGZ composite with a TG: ZnO ratio of 1: 1, exhibited significantly higher UV-blocking capacity compared with control samples. The results indicate that the fabric blocks 96.14% of UVA (315–400 nm) and 97.25% of UVB (280–315 nm) radiation.

Table 24 Results of the UV-blocking tests

TRANSMITTANCE OR BLOCKING OF ERYTHEMALLY WEIGHTED ULTRAVIOLET RADIATION THROUGH FABRIC : AATCC 183 (2020)	
	DRY TEST
The mean ultraviolet protection factor, UPF	35.28
- The mean UV-A transmittance, T(UV-A)	3.86 %
- The mean UV-B transmittance, T(UV-B)	2.75 %
The percent blocking (UV-A)	96.14 %
The percent blocking (UV-B)	97.25 %
UPF rating	30

Additionally, the fabric's Ultraviolet Protection Factor (UPF) is 30, which places it in a high protection category according to international standards. Fabrics with a UPF of 30-49 block approximately 96-97% of UV radiation. This can be attributed to the synergistic effect of TiO_2, ZnO, and GO within the composite matrix, which enhances the material's UV absorption and scattering properties. In comparison to the control fabrics, the TNPsGZ-coated fabric achieved superior performance in. blocking both UVA and UVB radiation.

This result aligns with the known properties of ZnO and TiO_2, which are widely recognized for their ability to absorb and reflect UV radiation. According to industry standards for UV-protective textiles, such as the UPF (Ultraviolet

Protection Factor) rating system, a fabric with a UPF of 50+ provides excellent protection, blocking over 98% of UV radiation. While the current UPF rating of the TNPsGZ-coated fabric is 30, its superior UV-blocking results suggest it could meet or exceed the UPF 50+ standard in optimized conditions. This makes the TNPsGZ-coated fabric a promising candidate for applications in protective clothing, outdoor gear, or other textiles requiring enhanced UV protection. (11,47,71)

4.3.3.3 Anti-bacterial activity

The antibacterial testing of the TNPsGZ-coated cotton fabric against *Staphylococcus aureus* (*S. aureus*), as shown in **Figure 79**, and *Escherichia coli* (*E. coli*), as shown in **Figure 80**, revealed that the fabric exhibited negligible antibacterial activity against both strains. These figures illustrate the antibacterial testing of TNPsGZ-coated cotton fabric against *Staphylococcus aureus* and *Escherichia coli* using a modified AATCC 100 method. Both tests show no significant inhibition zones around the fabric samples, indicating limited antibacterial activity under the testing conditions. Despite its excellent hydrophobic properties and UV protection, the composite's inability to inhibit bacterial growth suggests that the TiO_2, ZnO, and GO components, while blocking UV radiation and repelling water, may not possess strong antimicrobial properties in this specific composite formulation. One potential explanation for this outcome is the distribution and concentration of ZnO and TiO_2 within the fabric.

Although ZnO and TiO_2 have been shown to exhibit antibacterial properties under certain conditions, such as under UV light exposure, which generates reactive oxygen species (ROS) capable of destroying bacterial cells, the experimental conditions may not have been optimal for activating this antibacterial mechanism.

For instance, if the fabric was not exposed to sufficient UV light during testing, the photocatalytic activity of TiO_2 and ZnO may not have been adequately triggered to produce the ROS needed for bacterial inhibition. Additionally, the particle size and irregular distribution of ZnO and TiO_2 could further limit their effectiveness. Larger and unevenly distributed particles often exhibit a reduced specific surface area, which, as observed in prior studies, may impair ROS production and thus diminish antibacterial efficiency. (80)

Moreover, the hydrophobic nature of the fabric could contribute to the reduced antibacterial effectiveness. While the hydrophobic surface may prevent moisture absorption, which can inhibit bacterial growth to some extent, it also prevents the close interaction between bacteria and the active components of the composite, further limiting the antibacterial action. Ultimately, while the TNPsGZ-coated

fabric excels in providing UV protection and water repellency, its lack of antibacterial properties highlights the complexity of designing multifunctional materials. Improvements in antibacterial performance could be achieved by modifying the composition or processing conditions, such as increasing the ZnO content, optimizing particle dispersion, or introducing additional antibacterial agents.

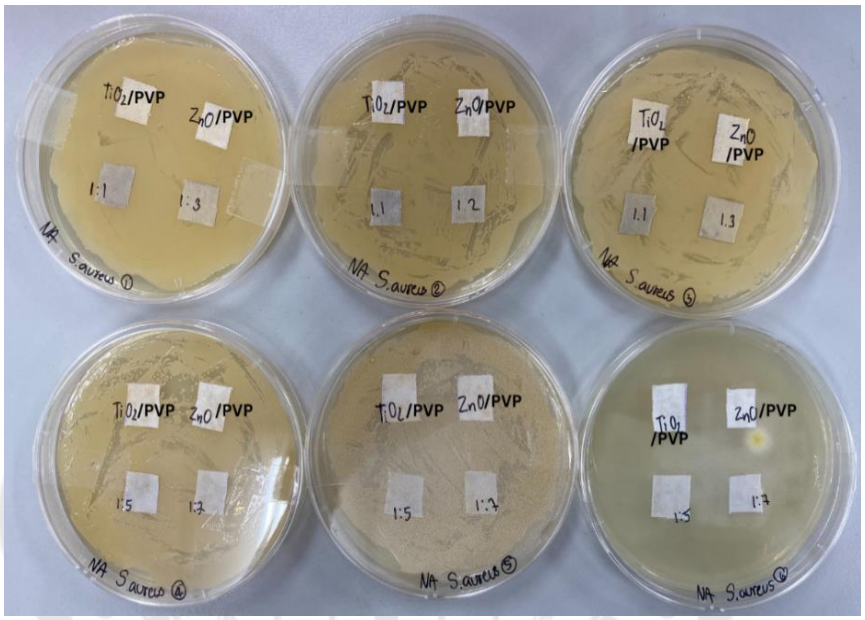

Figure 79 Antibacterial testing of the TNPsGZ-coated cotton fabric against *S.aureus*

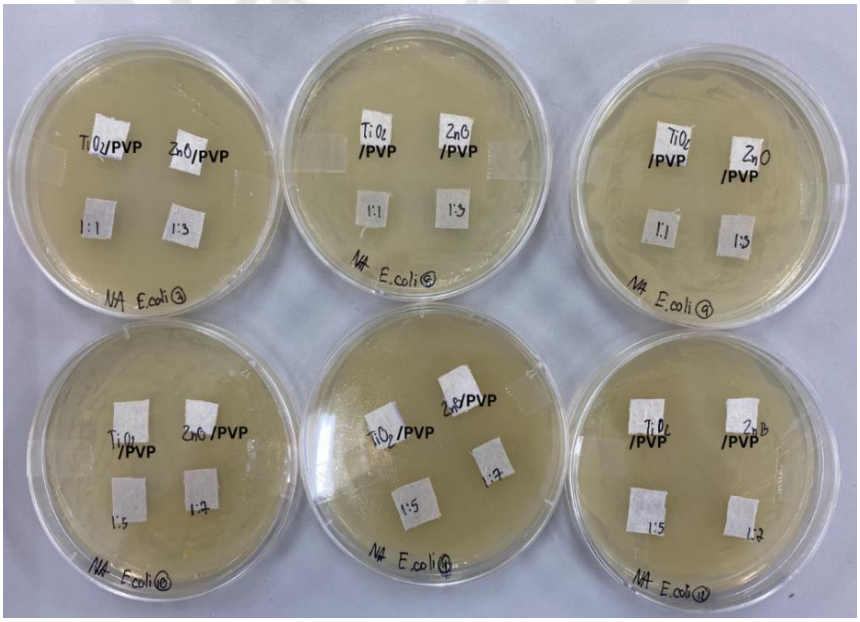

Figure 80 Antibacterial testing of the TNPsGZ-coated cotton fabric against *E.coli*

CHAPTER 5
CONCLUSIONS

5.1 Main conclusion of this study

Nanocomposite coatings have been successfully applied to a cotton fabric. The effect of the coating on hydrophobicity, UV protection and antibacterial properties has been examined. The following conclusions have been obtained:

1. The TiO_2-GO-ZnO (TNPsGZ) composites were successfully synthesized via ultrasonic-assisted technique. Different characterization techniques, such as FTIR, Raman spectroscopy, XRD and FE-SEM, have been utilized to examine the composite's physical and chemical properties. The results demonstrate the characteristics of TiO_2 nanoparticles, graphene oxide and zinc oxide particles.

2. The cotton fabric was coated using the pad-dry-cure process. The optical micrographs show the fabrics with a smooth, finished cotton fabric. The FE-SEM reveals the uniform TNPsGZ composite coating layer on the cotton fiber. The EDS, Raman and FTIR results confirm that the coating layer comprises TiO2 nanoparticles, graphene oxide and zinc oxide particles.

3. The number of coating layers plays an important role. It was found that the single-coated cotton fabrics exhibited satisfactory properties concerning water-repelling behavior.

4. Overall, the results demonstrate the improvement of cotton fabric's hydrophobicity and UV protection properties. The coated cotton significantly improves hydrophobicity with an advancing water contact angle of 129°. This coating offers a strong water-repelling behavior. In addition, the UV-shielding ability of the coated cotton fabric was confirmed by its strong UPF rating. The UV-protective textile is provided by coating with the TNPsGZ composites, blocking over 96% of UV-A and 97% of UV-B with a UPF rating of 30.

5. The antibacterial tests against Staphylococcus aureus and Escherichia coli revealed limited efficacy, suggesting that the composite's antibacterial properties were not fully optimized under the conditions tested. This limitation may be attributed to the insufficient activation of the photocatalytic effects of TiO_2 and ZnO, which require specific environmental conditions to generate reactive oxygen species (ROS) for bacterial inhibition.

6. These findings can be used to develop outdoor clothing for various applications in the textile industry.

5.2 Suggestion for future work

1. Examination of the optimum ratio of TiO_2 nanoparticles and ZnO particles to enhance the antibacterial functionality, such as increasing the ZnO particle content.

2. We are assessing the durability of washing tests.

REFERENCES

1. Masae M, Pitsuwan P, Sriwang T. HYDROPHOBICITY AND ANTIBACTERIAL ACTIVITY OF COATED COTTON FABRICS WITH CHITOSAN, TiO_2 AND SiO_2. Srinakharinwirot University (Journal of Science and Technology). 2018;11(21):165–78.

2. Kale BM. MULTIFUNCTIONAL COTTON FABRIC WITH NANO TIO_2 LOADED CELLULOSE.

3. Liu Y, Xia L, Zhang Q, Guo H, Wang A, Xu W, et al. Structure and properties of carboxymethyl cotton fabric loaded by reduced graphene oxide. Carbohydrate Polymers. 2019 Jun;214:117–23.

4. Alebeid OK, Zhao T. Review on: developing UV protection for cotton fabric. The Journal of The Textile Institute. 2017 Dec 2;108(12):2027–39.

5. Ray A, Singha K, Pandit P, Maity S. Advanced ultraviolet protective agents for textiles and clothing. In: Advances in Functional and Protective Textiles [Internet]. Elsevier; 2020 [cited 2023 Oct 25]. p. 243–60. Available from: https://linkinghub.elsevier.com/retrieve/pii/B9780128202579000114

6. Wirunchit S, Apivitcholchat C, Chodjarusawad T, Koetniyom W. The study of UV protection materials. In Chonburi, Thailand; 2018 [cited 2023 Oct 25]. p. 020024. Available from: https://pubs.aip.org/aip/acp/article/772422

7. Mallia JC, Anastasi AA, Briffa SM. Developing Self-Cleaning Photocatalytic TiO_2 Nanocomposite Coatings: International Journal of Surface Engineering and Interdisciplinary Materials Science. 2023 Jun 16;11(1):1–20.

8. Abidi N, Hequet E, Tarimala S, Dai LL. Cotton fabric surface modification for improved UV radiation protection using sol–gel process. J of Applied Polymer Sci. 2007 Apr 5;104(1):111–7.

9. Jongprateep O, Mani-lata C, Sakunrak Y, Audcharuk K, Narapong T, Janbooranapinij K, et al. Titanium dioxide and fluoropolymer-based coating for smart fabrics with antimicrobial and water-repellent properties. RSC Adv. 2022;12(1):588–94.

10. VerbiČ A, Gorjanc M, SimonČiČ B. Zinc Oxide for Functional Textile Coatings: Recent Advances. Coatings. 2019 Aug 27;9(9):550.

11. Khan MZ, Baheti V, Ashraf M, Hussain T, Ali A, Javid A, et al. Development of UV Protective, Superhydrophobic and Antibacterial Textiles Using ZnO and TiO_2 Nanoparticles. Fibers Polym. 2018 Aug;19(8):1647–54.

12. Zhao J, Deng B, Lv M, Li J, Zhang Y, Jiang H, et al. Graphene Oxide-Based Antibacterial Cotton Fabrics. Adv Healthcare Materials. 2013 Sep;2(9):1259–66.

13. Krishnamoorthy K, Navaneethaiyer U, Mohan R, Lee J, Kim SJ. Graphene oxide nanostructures modified multifunctional cotton fabrics. Appl Nanosci. 2012 Jun;2(2):119–26.

14. Zhou J, Luo Q, Gao P, Ma H. Assembly of graphene oxide on cotton fiber through dyeing and their properties. RSC Adv. 2020;10(20):11982–9.

15. Chandram MS. Studieson Mechanical Behavior of Jute Cotton Reinforced in Brahma Resin. 2017;10(1).

16. House F. Cotton Fabric [Internet]. Cotton Fabric. Available from: https://www.housefabric.com/Cotton-Fabric-Information.aspx

17. Sewing & Craft Alliance. Cotton ... The Most Popular Fabric in the World [Internet]. SEW-lutions Guidelines. 2023. Available from: https://www.sewing.org/files/guidelines/4_105_cotton.pdf

18. Hsieh YL. Chemical structure and properties of cotton. In: Cotton [Internet]. Elsevier; 2007 [cited 2023 Oct 31]. p. 3–34. Available from:

https://linkinghub.elsevier.com/retrieve/pii/B9781845690267500019

19. Hosseini Ravandi SA, Valizadeh M. Properties of fibers and fabrics that contribute to human comfort. In: Improving Comfort in Clothing [Internet]. Elsevier; 2011 [cited 2023 Nov 8]. p. 61–78. Available from: https://linkinghub.elsevier.com/retrieve/pii/B9781845695392500028

20. Begum HA, Tanni TR, Shahid MA. Analysis of Water Absorption of Different Natural Fibers. JTST. 2021;07(04):152–60.

21. Racovita AD. Titanium Dioxide: Structure, Impact, and Toxicity. IJERPH. 2022 May 6;19(9):5681.

22. Eddy DR, Permana MD, Sakti LK, Sheha GAN, Solihudin, Hidayat S, et al. Heterophase Polymorph of TiO_2 (Anatase, Rutile, Brookite, TiO_2 (B)) for Efficient Photocatalyst: Fabrication and Activity. Nanomaterials. 2023 Feb 12;13(4):704.

23. Hanaor DAH, Sorrell CC. Review of the anatase to rutile phase transformation. J Mater Sci. 2011 Feb;46(4):855–74.

24. Spurr RA, Myers Howard. Quantitative Analysis of Anatase-Rutile Mixtures with an X-Ray Diffractometer. Anal Chem. 1957 May 1;29(5):760–2.

25. Pisitsak P, Samootsoot A, Chokpanich N. Investigation of the Self-cleaning Properties of Cotton Fabrics Finished with Nano-TiO_2 and Nano-TiO_2 Mixed with Fumed Silica.

26. Bokuniaeva AO, Vorokh AS. Estimation of particle size using the Debye equation and the Scherrer formula for polyphasic TiO_2 powder. J Phys: Conf Ser. 2019 Dec 1;1410(1):012057.

27. Özgür Ü, Avrutin V, Morkoç H. Zinc Oxide Materials and Devices Grown by Molecular Beam Epitaxy. In: Molecular Beam Epitaxy [Internet]. Elsevier; 2018 [cited 2023 Nov 2]. p. 343–75. Available from:

https://linkinghub.elsevier.com/retrieve/pii/B9780128121368000165

28. Arputharaj A, Nadanathangam V, Shukla SR. A simple and efficient protocol to develop durable multifunctional property to cellulosic materials using in situ generated nano-ZnO. Cellulose. 2017 Aug;24(8):3399–410.

29. Hellen N. A Study on the Properties of ZnO/TiO_2 Nanocomposite Prepared via the Sol-gel Technique. 2017;

30. Johra FT, Jung WG. RGO–TiO_2–ZnO composites: Synthesis, characterization, and application to photocatalysis. Applied Catalysis A: General. 2015 Feb;491:52–7.

31. Idris NJ, Bakar SA, Mohamed A, Muqoyyanah M, Othman MHD, Mamat MH, et al. Photocatalytic performance improvement by utilizing GO_MWCNTs hybrid solution on sand/ZnO/TiO_2-based photocatalysts to degrade methylene blue dye. Environ Sci Pollut Res. 2021 Feb;28(6):6966–79.

32. Rashid MM, Simon**Č**i**Č** B, Tomši**Č** B. Recent advances in TiO_2-functionalized textile surfaces. Surfaces and Interfaces. 2021 Feb;22:100890.

33. Lin HY, Chou YY, Cheng CL, Chen YF. Giant enhancement of band edge emission based on ZnO/TiO_2 nanocomposites. Opt Express. 2007;15(21):13832.

34. Huang Y, Li R, Chen D, Hu X, Chen P, Chen Z, et al. Synthesis and Characterization of CNT/TiO_2/ZnO Composites with High Photocatalytic Performance. Catalysts. 2018 Apr 9;8(4):151.

35. Sakar M, Mithun Prakash R, Do TO. Insights into the TiO_2-Based Photocatalytic Systems and Their Mechanisms. Catalysts. 2019 Aug 9;9(8):680.

36. Ban FY, Majid SR, Huang NM, Lim HN. Graphene Oxide and Its Electrochemical Performance. International Journal of Electrochemical Science. 2012;7(5):4345–51.

37. Hidayah NMS, Liu WW, Lai CW, Noriman NZ, Khe CS, Hashim U, et al. Comparison on

graphite, graphene oxide and reduced graphene oxide: Synthesis and characterization. In Penang, Malaysia; 2017 [cited 2024 Nov 12]. p. 150002. Available from: https://pubs.aip.org/aip/acp/article/965987

38. Jiřičková A, Jankovský O, Sofer Z, Sedmidubský D. Synthesis and Applications of Graphene Oxide. Materials. 2022 Jan 25;15(3):920.

39. Abdolhosseinzadeh S, Asgharzadeh H, Sadighikia S, Khataee A. UV-assisted synthesis of reduced graphene oxide–ZnO nanorod composites immobilized on Zn foil with enhanced photocatalytic performance. Res Chem Intermed. 2016 May;42(5):4479–96.

40. Zuo D, Li G, Ling Y, Cheng S, Xu J, Zhang H. Durable UV-blocking Property of Cotton Fabrics with Nanocomposite Coating Based on Graphene Oxide/ZnO Quantum Dot via Water-based Self-assembly. Fibers Polym. 2021 Jul;22(7):1837–43.

41. Krishna MBM, Venkatramaiah N, Venkatesan R, Rao DN. Graphene oxide (GO)-Semiconductor (ZnO, TiO_2) nanoparticles for broadband optical limiting. In: International Conference on Fibre Optics and Photonics [Internet]. Chennai: OSA; 2012 [cited 2024 Nov 12]. p. TPo.42. Available from: https://opg.optica.org/abstract.cfm?URI=Photonics-2012-TPo.42

42. El-Shafai N, El-Khouly ME, El-Kemary M, Ramadan M, Eldesoukey I, Masoud M. Graphene oxide decorated with zinc oxide nanoflower, silver and titanium dioxide nanoparticles: fabrication, characterization, DNA interaction, and antibacterial activity. RSC Adv. 2019;9(7):3704–14.

43. Priyanka VS, Murali MK, Rahman MA. Biocidal Properties of Zinc Oxide-Titanium Dioxide-Graphene Oxide Nanocomposites via One-Pot Facile Precipitation Method. BioNanoSci. 2022 Mar;12(1):41–8.

44. Tissera ND, Wijesena RN, Perera JR, De Silva KMN, Amaratunge GAJ. Hydrophobic

cotton textile surfaces using an amphiphilic graphene oxide (GO) coating. Applied Surface Science. 2015 Jan;324:455–63.

45. Ragesh P, Anand Ganesh V, Nair SV, Nair AS. A review on 'self-cleaning and multifunctional materials.' J Mater Chem A. 2014;2(36):14773–97.

46. Ashar A, Bhutta ZA, Shoaib M, Alharbi NK, Fakhar-e-Alam M, Atif M, et al. Cotton fabric loaded with ZnO nanoflowers as a photocatalytic reactor with promising antibacterial activity against pathogenic E. coli. Arabian Journal of Chemistry. 2023 Sep;16(9):105084.

47. Thao NMT. MEASURE THE ULTRAVIOLET PROTECTION FACTOR (UPF) OF FABRICS ON UV-VIS SPECTROPHOTOMETER.

48. Gulati R, Sharma S, Sharma RK. Antimicrobial textile: recent developments and functional perspective. Polym Bull. 2022 Aug;79(8):5747–71.

49. Yang H, Zhu S, Pan N. Studying the mechanisms of titanium dioxide as ultraviolet-blocking additive for films and fabrics by an improved scheme. J of Applied Polymer Sci. 2004 Jun 5;92(5):3201–10.

50. Shateri-Khalilabad M, Yazdanshenas ME. Bifunctionalization of cotton textiles by ZnO nanostructures: antimicrobial activity and ultraviolet protection. Textile Research Journal. 2013 Jun;83(10):993–1004.

51. Nautiyal A, Shukla SR, Prasad V. ZnO-TiO_2 hybrid nanocrystal-loaded, wash durable, multifunction cotton textiles. Cellulose. 2022 Jul;29(10):5923–41.

52. Cuong DLT, Van Cuong L, Nghia LTT, Trinh DN, Linh NTT, Hai ND, et al. Synthesis of titanium dioxide/reduced graphene oxide nanocomposite by ultrasound-assisted mechanical mixing method for fabricating photoanode to upgrade the performance and stability of dye-sensitized solar cell. Materials Research Bulletin. 2022

Dec;156:112000.

53. Al-Taweel SS, Saud HR. New route for synthesis of pure anatase TiO_2 nanoparticles via utrasound- assisted sol-gel method. 2016;

54. Di Paola A, Cufalo G, Addamo M, Bellardita M, Campostrini R, Ischia M, et al. Photocatalytic activity of nanocrystalline TiO_2 (brookite, rutile and brookite-based) powders prepared by thermohydrolysis of TiCl4 in aqueous chloride solutions. Colloids and Surfaces A: Physicochemical and Engineering Aspects. 2008 Mar;317(1–3):366–76.

55. Praveen P, Viruthagiri G, Mugundan S, Shanmugam N. Structural, optical and morphological analyses of pristine titanium di-oxide nanoparticles – Synthesized via sol–gel route. Spectrochimica Acta Part A: Molecular and Biomolecular Spectroscopy. 2014 Jan;117:622–9.

56. Hardcastle FD. Raman Spectroscopy of Titania (TiO_2) Nanotubular Water-Splitting Catalysts. Arkansas Academy of Science [Internet]. 2011 Jan 1 [cited 2024 Nov 12];65. Available from: https://scholarworks.uark.edu/jaas/vol65/iss1/9

57. Wang J, Yu J, Zhu X, Kong XZ. Preparation of hollow TiO_2 nanoparticles through TiO_2 deposition on polystyrene latex particles and characterizations of their structure and photocatalytic activity. Nanoscale Res Lett. 2012 Dec;7(1):646.

58. Gul W, Alrobei H. Effect of Graphene Oxide Nanoparticles on the Physical and Mechanical Properties of Medium Density Fiberboard. Polymers. 2021 May 31;13(11):1818.

59. Yavuz S, Bandaru PR. Ag nanowire coated reduced graphene oxide/n-silicon Schottky junction based solar cell. In: 2016 IEEE Conference on Technologies for Sustainability (SusTech) [Internet]. Phoenix, AZ, USA: IEEE; 2016 [cited 2024 Nov 12]. p. 265–9. Available from: http://ieeexplore.ieee.org/document/7897178/

60. Ruidíaz-Martínez M, Álvarez MA, López-Ramón MV, Cruz-Quesada G, Rivera-Utrilla J, Sánchez-Polo M. Hydrothermal Synthesis of rGO-TiO_2 Composites as High-Performance UV Photocatalysts for Ethylparaben Degradation. Catalysts. 2020 May 8;10(5):520.

61. How GTS, Pandikumar A, Ming HN, Ngee LH. Highly exposed {001} facets of titanium dioxide modified with reduced graphene oxide for dopamine sensing. Sci Rep. 2014 May 23;4(1):5044.

62. Maharana HS, Rai PK, Basu A. Surface-mechanical and electrical properties of pulse electrodeposited Cu–graphene oxide composite coating for electrical contacts. J Mater Sci. 2017 Jan;52(2):1089–105.

63. Bashir S, Awan MS, Farrukh MA, Naidu R, Khan SA, Rafique N, et al. In-vivo (Albino Mice) and in-vitro Assimilation and Toxicity of Zinc Oxide Nanoparticles in Food Materials. IJN. 2022 Sep;Volume 17:4073–85.

64. Silambarasan M, Saravanan S, Soga T. Raman and Photoluminescence Studies of Ag and Fe-doped ZnO Nanoparticles.

65. Kalpana VN, Kataru BAS, Sravani N, Vigneshwari T, Panneerselvam A, Devi Rajeswari V. Biosynthesis of zinc oxide nanoparticles using culture filtrates of Aspergillus niger: Antimicrobial textiles and dye degradation studies. OpenNano. 2018;3:48–55.

66. Mendes CR, Dilarri G, Forsan CF, Sapata VDMR, Lopes PRM, De Moraes PB, et al. Antibacterial action and target mechanisms of zinc oxide nanoparticles against bacterial pathogens. Sci Rep. 2022 Feb 16;12(1):2658.

67. Naqvi SMohdA, Soleimani H, Yahya N, Irshad K. Structural and optical properties of chromium doped zinc oxide nanoparticles synthesized by sol-gel method. In Kuala Lumpur, Malaysia; 2014 [cited 2024 Nov 12]. p. 530–7. Available from: https://pubs.aip.org/aip/acp/article/1621/1/530-537/882448

68. Bai KJ, Chuang KJ, Ma CM, Chang TY, Chuang HC. Human lung adenocarcinoma cells with an EGFR mutation are sensitive to non-autophagic cell death induced by zinc oxide and aluminium-doped zinc oxide nanoparticles. J Toxicol Sci. 2017;42(4):437–44.

69. Sudesh, Kumar N, Das S, Bernhard C, Varma GD. Effect of graphene oxide doping on superconducting properties of bulk MgB_2. Supercond Sci Technol. 2013 Sep 1;26(9):095008.

70. Vaideki K, Jayakumar S, Thilagavathi G, Rajendran R. A study on the antimicrobial efficacy of RF oxygen plasma and neem extract treated cotton fabrics. Applied Surface Science. 2007 Jun;253(17):7323–9.

71. Ahmad I, Kan C wai, Yao Z. Photoactive cotton fabric for UV protection and self-cleaning. RSC Adv. 2019;9(32):18106–14.

72. Vasudevan P, Thomas S, Biju PR, Sudarsanakumar C, Unnikrishnan NV. Synthesis and structural characterization of sol–gel derived titania/poly (vinyl pyrrolidone) nanocomposites. J Sol-Gel Sci Technol. 2012 Apr;62(1):41–6.

73. Singh K, Bhattu M, Singh G, Mubarak NM, Singh J. OPEN Light-absorption-driven. Scientific Reports.

74. Gutul T, Rusu E, Condur N, Ursaki V, Goncearenco E, Vlazan P. Preparation of poly(*N* -vinylpyrrolidone)-stabilized ZnO colloid nanoparticles. Beilstein J Nanotechnol. 2014 Apr 3;5:402–6.

75. Suksri S, Aeimbhu A. Fabrication and Characterization of TiO_2/GO/ZnO Composites Coated Cotton Fabric for Improved Hydrophobic Property. 2024;40(1).

76. Ali MM, Haque MdJ, Kabir MH, Kaiyum MA, Rahman MS. Nano synthesis of ZnO–TiO_2 composites by sol-gel method and evaluation of their antibacterial, optical and

photocatalytic activities. Results in Materials. 2021 Sep;11:100199.

77. Laid N, Bouanimba N, Ben Ahmede A, Toureche A, Sehili T. Characterization of ZnO and TiO_2 Nanopowders and their Application for Photocatalytic Water Treatment. Acta Phys Pol A. 2020 Mar;137(3):305–12.

78. Scarpelli F, Mastropietro TF, Poerio T, Godbert N. Mesoporous TiO_2 Thin Films: State of the Art. In: Yang D, editor. Titanium Dioxide - Material for a Sustainable Environment [Internet]. InTech; 2018 [cited 2024 Apr 19]. Available from: http://www.intechopen.com/books/titanium-dioxide-material-for-a-sustainable-environment/mesoporous-tio2-thin-films-state-of-the-art

79. Irfan M, Hussain H, Saleem B, Saleem M, Shukrullah S, Legutko S, et al. Evaluation of Ultrasonically ZnO Loading Effect on Photocatalytic Self-Cleaning, UV Protection and Antibacterial Activity of Plasma/Citric Acid-Activated Cotton Fabric. Nanomaterials. 2022 Jun 20;12(12):2122.

80. Babayevska N, Przysiecka Ł, Iatsunskyi I, Nowaczyk G, Jarek M, Janiszewska E, et al. ZnO size and shape effect on antibacterial activity and cytotoxicity profile. Sci Rep. 2022 May 17;12(1):8148.

VITA